

UNIVERSIDADE FEDERAL DE CAMPINA GRANDE
DEPARTAMENTO DE ENGENHARIA ELÉTRICA
PROGRAMA DE PÓS-GRADUAÇÃO EM ENGENHARIA ELÉTRICA



Universidade Federal
de Campina Grande

DOCTORAL DISSERTATION

*Analysis and Design of the Flight Control System for Battery
Powered Mini Drones*

Augusto de Holanda Barreto Martins Tavares

Campina Grande - PB

April 2023

Analysis and Design of the Flight Control System for Battery Powered Mini
Drones

Augusto de Holanda Barreto Martins Tavares

Doctoral dissertation submitted to the coordination of
the Post-graduate Program in Electrical Engineering of
the Federal University of Campina Grande as part of the
pre-requisites necessary for attaining the title of D. Sc.
in Electrical Engineering

Concentration area: Information Processing

Antonio Marcus Nogueira Lima, Dr.

Supervisor

Saulo Oliveira Dornellas Lima, D. Sc.

Supervisor

Campina Grande - PB

April 2023

T231a Tavares, Augusto de Holanda Barreto Martins.
Analysis and design of the flight control system for battery powered mini drones / Augusto de Holanda Barreto Martins Tavares. – Campina Grande, 2023.
153 f. : il. color.

Tese (Doutorado em Engenharia Elétrica) – Universidade Federal de Campina Grande, Centro de Engenharia Elétrica e Informática, 2023.
"Orientação: Prof. Dr. Antonio Marcus Nogueira Lima, Prof. Dr. Saulo Oliveira Dornellas Lima".

Referências.

1. Processamento da Informação. 2 Quadrotores. 3. Controle Linear e não Linear. 4. Baterias LiPo. 5. Projeto de Controle. 6. Modelagem. I. Lima, Antonio Marcus Nogueira. II. Lima, Saulo Oliveira Dornella. III. Título.

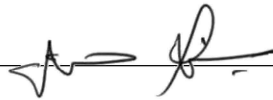
CDU 004.451.7:004.7(043)

Augusto de Holanda Barreto Martins Tavares

Analysis and Design of Battery Powered Quadrotors
Considering the Electrical Subsystem

Doctoral dissertation submitted to the coordination of
the Post-graduate Program in Electrical Engineering of
the Federal University of Campina Grande as part of the
pre-requisites necessary for attaining the title of D. Sc.
in Electrical Engineering

Doctoral Dissertation approved on April 5th 2023



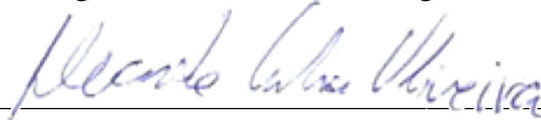
D. Sc. Angelo Perkusich, Evaluating commission member



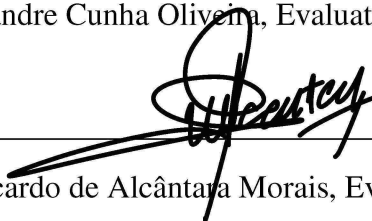
D. Sc. Tiago Pereira do Nascimento, Evaluating commission member



D. Sc. Paulo Lilles Jorge Drews Júnior, Evaluating commission member



D. Sc. Alexandre Cunha Oliveira, Evaluating commission member



D. Sc. Marcos Ricardo de Alcântara Morais, Evaluating commission member

Campina Grande - PB

April 2023



MINISTÉRIO DA EDUCAÇÃO

UNIVERSIDADE FEDERAL DE CAMPINA GRANDE

POS-GRADUACAO EM ENGENHARIA ELETRICA

Rua Aprigio Veloso, 882, - Bairro Universitario, Campina Grande/PB, CEP 58429-900

REGISTRO DE PRESENÇA E ASSINATURAS

ATA DA DEFESA PARA CONCESSÃO DO GRAU DE DOUTOR EM CIÊNCIAS, NO DOMÍNIO DA ENGENHARIA ELÉTRICA, REALIZADA EM 5 DE ABRIL DE 2023 (Nº361)

CANDIDATO: AUGUSTO DE HOLANDA BARRETO MARTINS TAVARES. COMISSÃO EXAMINADORA: ANGELO PERKUSICH, DEE, UFCG, Presidente da Comissão e Examinador interno, ANTONIO MARCUS NOGUEIRA LIMA, Dr., UFCG, SAULO OLIVEIRA DORNELLAS LUIZ, D.Sc., UFPE, Orientadores, ALEXANDRE CUNHA OLIVEIRA, D.Sc., UFCG, MARCOS RICARDO DE ALCÂNTARA MORAIS, Dr, UFCG., Examinadores internos, TIAGO PEREIRA DO NASCIMENTO, Dr., UFPB, PAULO LILLES JORGE DREWS JÚNIOR, Dr., FURG., Examinadores externos. TÍTULO DA TESE: Analysis and Design of Flight Control System for Battery Powered Quadrotors Considering the Electrical Subsystem. ÁREA DE CONCENTRAÇÃO: Processamento da Informação. HORA DE INÍCIO: 14h00 – LOCAL: Sala Virtual, conforme Art. 5º da PORTARIA SEI Nº 01/PRPG/UFCG/GPR, DE 09 DE MAIO DE 2022. Em sessão pública, após exposição de cerca de 45 minutos, o candidato foi arguido oralmente pelos membros da Comissão Examinadora, tendo demonstrado suficiência de conhecimento e capacidade de sistematização, no tema de sua tese, obtendo conceito APROVADO com pequenas modificações no texto, de acordo com as exigências da Comissão Examinadora, que deverão ser cumpridas no prazo de 30 dias. Face à aprovação, declara o presidente da Comissão, achar-se o examinado, após o cumprimento das referidas exigências, legalmente habilitado a receber o Grau de Doutor em Ciências, no domínio da Engenharia Elétrica, cabendo a Universidade Federal de Campina Grande, como de direito, providenciar a expedição do Diploma, a que o mesmo faz jus. Na forma regulamentar, foi lavrada a presente ata, que é assinada por mim, Filipe Emmanuel Porfírio Correia, e os membros da Comissão Examinadora presentes. Campina Grande, 5 de Abril de 2023.

Filipe Emmanuel Porfírio Correia – Secretário

ANGELO PERKUSICH, DEE, UFCG
Presidente da Comissão e Examinador interno

ANTONIO MARCUS NOGUEIRA LIMA, Dr., UFCG
Orientador

SAULO OLIVEIRA DORNELLAS LUIZ, D.Sc., UFPE
Orientador

ALEXANDRE CUNHA OLIVEIRA, D.Sc., UFCG
Examinador interno

MARCOS RICARDO DE ALCÂNTARA MORAIS, Dr, UFCG
Examinador interno

TIAGO PEREIRA DO NASCIMENTO, Dr., UFPB
Examinador externo

PAULO LILLES JORGE DREWS JÚNIOR, Dr., FURG
Examinador externo

AUGUSTO DE HOLANDA BARRETO MARTINS TAVARES
Candidato

2 - APROVAÇÃO

2.1. Segue a presente Ata de Defesa de Tese de Doutorado do candidato AUGUSTO DE HOLANDA BARRETO MARTINS TAVARES, assinada eletronicamente pela Comissão Examinadora acima identificada.

2.2. No caso de examinadores externos que não possuam credenciamento de usuário externo ativo no SEI, para igual assinatura eletrônica, os examinadores internos signatários certificam que os examinadores externos acima identificados participaram da defesa da tese e tomaram conhecimento do teor deste documento.



Documento assinado eletronicamente por **FILIFE EMMANUEL PORFIRIO CORREIA, SECRETÁRIO (A)**, em 10/04/2023, às 10:54, conforme horário oficial de Brasília, com fundamento no art. 8º, caput, da [Portaria SEI nº 002, de 25 de outubro de 2018](#).



Documento assinado eletronicamente por **ANTONIO MARCUS NOGUEIRA LIMA, PROFESSOR(A) DO MAGISTERIO SUPERIOR**, em 10/04/2023, às 12:01, conforme horário oficial de Brasília, com fundamento no art. 8º, caput, da [Portaria SEI nº 002, de 25 de outubro de 2018](#).



Documento assinado eletronicamente por **Tiago Pereira do Nascimento, Usuário Externo**, em 10/04/2023, às 13:12, conforme horário oficial de Brasília, com fundamento no art. 8º, caput, da [Portaria SEI nº 002, de 25 de outubro de 2018](#).



Documento assinado eletronicamente por **ANGELO PERKUSICH, PROFESSOR(A) DO MAGISTERIO SUPERIOR**, em 10/04/2023, às 15:12, conforme horário oficial de Brasília, com fundamento no art. 8º, caput, da [Portaria SEI nº 002, de 25 de outubro de 2018](#).



Documento assinado eletronicamente por **MARCOS RICARDO ALCANTARA MORAIS, PROFESSOR 3 GRAU**, em 10/04/2023, às 16:54, conforme horário oficial de Brasília, com fundamento no art. 8º, caput, da [Portaria SEI nº 002, de 25 de outubro de 2018](#).



Documento assinado eletronicamente por **ALEXANDRE CUNHA OLIVEIRA, PROFESSOR 3 GRAU**, em 14/04/2023, às 16:28, conforme horário oficial de Brasília, com fundamento no art. 8º, caput, da [Portaria SEI nº 002, de 25 de outubro de 2018](#).



Documento assinado eletronicamente por **AUGUSTO DE HOLANDA BARRETO MARTINS TAVARES, Usuário Externo**, em 09/05/2023, às 14:15, conforme horário oficial de Brasília, com fundamento no art. 8º, caput, da [Portaria SEI nº 002, de 25 de outubro de 2018](#).



A autenticidade deste documento pode ser conferida no site <https://sei.ufcg.edu.br/autenticidade>, informando o código verificador **3289416** e o código CRC **1F209DF8**.

Abstract

This doctoral dissertation studies how the electrical subsystem of a battery-powered quadrotor mini drone affects its altitude and attitude dynamics, and how to compensate for the negative effects on the performance caused by the drop in battery voltage during flight. The presented study shows that the closed-loop dynamic behavior degrades as the battery discharges during flight, due to the electrical subsystem being ignored during the flight controller design phase. A study of the relevant bibliography is conducted, showing that this research topic is of interest to the academic community, but has not been explored to the degree presented in this work. A model of a battery-powered quadrotor is constructed, from which a mathematical analysis is conducted showing how the electrical subsystem parameters and the battery discharge affect the closed-loop altitude and attitude dynamics. This system model included the modeling of a LiPo battery, which resulted in the proposal of a lumped parameter model for this type of battery. The mathematical analysis of the quadrotor model showed that the system dynamics get slower as the battery discharges. Compensation for this effect is proposed through two approaches: a battery-aware controller design and by generating the motor commands based on the actual battery voltage instead of the nominal voltage value. A discussion is conducted regarding the impact of the aggressiveness of the attitude controller reference dynamics over the energy consumption, stating that the more aggressive controllers lead to a slower battery discharge. These proposals were tested in simulated and experimental environments using a Parrot Mambo mini drone. The results showed that the proposed compensation techniques positively impacted both the altitude and attitude loops, resulting in a consistent closed-loop behavior for different battery voltage values, along with a smaller steady-state error. The effect of the proposed compensation approaches over the attitude loop was less pronounced than over the altitude loop. These improvements present a trade-off in the form of increased energy consumption. The choice of a more aggressive control strategy when performing a test flight was shown to result in a slower battery discharge when compared to a less aggressive one.

Keywords: Quadrotors, Linear and Nonlinear Control, LiPo batteries, Controller Design, Modelling

Resumo

Esta tese de doutorado estuda como o subsistema elétrico de um mini quadrotor alimentado por bateria afeta as suas dinâmicas de altura e de atitude, e como compensar os efeitos negativos sobre o desempenho decorrentes da queda da tensão da bateria durante o voo. O estudo apresentado mostra que a comportamento dinâmico em malha fechada piora a medida que a bateria descarrega durante o voo, devido ao subsistema elétrico ser desconsiderado durante a etapa de projeto do controlador de voo. Um estudo da bibliografia relevante é realizado, mostrando que este tópico de pesquisa é de interesse da comunidade acadêmico, mas não foi previamente explorado com a profundidade apresentada neste trabalho. O modelo de um quadrotor alimentado por bateria é elaborado, a partir de onde uma análise matemática é realizada demonstrando como os parâmetros do subsistema elétrico e a descarga da bateria afetam as dinâmicas de malha fechada de altura e de atitude. Esse modelo incluiu a modelagem de uma bateria LiPo, que resultou na proposta de um modelo a parâmetros concentrados para este tipo de bateria. A análise matemática do modelo do quadrotor mostrou que as dinâmicas do sistema ficam mais lentas a medida que a bateria descarrega. A compensação deste efeito é proposta por meio de duas abordagens: o projeto de um controlador ciente da bateria e a geração de comandos para os motores a partir da tensão medida da bateria ao invés do valor nominal da tensão. Uma discussão a respeito do impacto da agressividade da dinâmica de referência do controlador de atitude sobre o consumo de energia é realizada, afirmando que dinâmicas de referência mais agressivas levam a uma descarga mais lenta da bateria. Estas propostas foram testadas em ambiente simulado e experimental, utilizando um mini drone Parrot Mambo. Os resultados mostraram que as técnicas de compensação propostas impactaram positivamente tanto as malhas de altura como a de atitude, resultando em um comportamento de malha fechada consistente para diferentes valores de tensão da bateria, além de um erro de regime permanente menor. O efeito das técnicas de compensação sobre a malha de atitude foi menor do que sobre a malha de altura. Foi mostrado que a escolha de uma estratégia de controle mais agressiva ao realizar um voo de teste leva a um menor consumo de energia quando comparada a uma estratégia menos agressiva.

Palavras-chave: Quadrotores, Controle linear e não linear, Baterias LiPo, Projeto de Controle, Modelagem

Acknowledgements

First and foremost I must thank my family. I have been blessed with a caring and loving wife, that shares my profession and has a seemingly endless amount of patience to deal with my quirks and moods. If you are reading this document, it is because she was by my side, unwavering. Thanks must also be extended to my aunts, uncles, cousins, grandparents, and in-laws. I have two younger sisters, who are a source of inspiration for me to try and be better, although I do not always succeed. My father has been a perennial role model when it comes to respecting and pursuing knowledge, and I guess that some of it must have rubbed on me over time. Finally, I must thank my mother, which I, unfortunately, will not be able to do properly here, as it would require me to write a second thesis in which I describe how unbelievably lucky I am to have her supporting me.

I thank my research supervisors Prof. Antonio Marcus and Prof. Saulo Dornellas, and Prof. Tiago Nascimento who also collaborated with this research. I also thank all other colleagues who contributed to this work, including members from three institutions (UFCG, UFPB, and TUM-FSD). Scientific research is a collaborative endeavor by nature, and this document is a direct result of this jolly cooperation.

I thank my friends, and I am fortunate enough to say that if I were to list their names, this page would not be enough, so I will resort to internal jokes and riddles. A certain group of armored armadillos always believed in me, even when I did not. I have more than a few almost beautiful friends, and their camaraderie has been a boon for some 10 years and counting. Salem really *is* the best, and I should really pay for that sushi.

I would be remiss if I did not mention that a significant part of the research presented here was conducted during a real honest-to-god global pandemic. It was only through the support of those close to me that I was able to get by during the toughest of times.

This study was financed in part by the Coordenação de Aperfeiçoamento de Pessoal de Nível Superior - Brasil (CAPES) - Finance Code 001 and the UFCG Post-graduate Program of Electrical Engineering (PPgEE).

“God does not play dice with the universe; He plays an ineffable game of His own devising, which might be compared, from the perspective of any of the other players [i.e. everybody], to being involved in an obscure and complex variant of poker in a pitch-dark room, with blank cards, for infinite stakes, with a Dealer who won’t tell you the rules, and who smiles all the time.”

— Neil Gaiman & Terry Pratchett, *Good Omens: The Nice and Accurate Prophecies of Agnes Nutter, Witch*

“Detective, each of us has our part to play in the world. My part is to solve crimes. I am under no illusion that my role isn’t a minor one, in the scheme of things... but I embrace it because it’s my role, and it’s yours too, detective, whether you accept it or not!”

— Lieutenant Kim Kitsuragi, *Disco Elysium*

Contents

List of abbreviations, acronyms and symbols	viii
List of figures	xiv
List of tables	xix
1 Introduction	1
1.1 Introduction to quadrotors	1
1.2 Motivation	3
1.3 Objectives	5
1.4 Methodology	6
1.5 Contributions	7
1.6 Document structure	8
2 Related works	10
2.1 Lithium-polymer battery models	10
2.2 Electrical subsystem on quadrotors	14
2.3 Energy efficiency on quadrotors	16
3 Model of a quadrotor mini drone	19
3.1 Basic concepts	19
3.2 State variables	22
3.3 Cinematic and dynamic equations	23
3.4 Electrical subsystem	25
3.5 Control allocation and command generation	28
3.6 Nonlinear dynamic inversion and error controller	30
3.6.1 Lie derivative	31

3.6.2	Relative degree	32
3.6.3	Feedback linearization	32
3.6.4	Applying NDI to a quadrotor	34
3.7	Integrated model	40
4	Model of a lithium-polymer battery	43
4.1	Workings of lithium-based batteries	43
4.2	Rakhmatov-Vrudhula model	46
4.3	Electrical model	53
4.4	Discrete-time model	54
4.5	Results	57
4.5.1	Methods and materials	57
4.5.2	Analysis of the modeling process	62
4.5.3	Analysis of the RC parallel circuits	76
4.5.4	GiFi Power 600 <i>mAh</i> 3.7 V 15 C results	79
4.6	Partial conclusions	85
5	Analysis of the closed-loop altitude and attitude dynamics	86
5.1	Altitude loop analysis	86
5.2	Attitude loop analysis	92
5.3	Compensation of the electrical subsystem effects	95
5.3.1	Battery-aware controller design	95
5.3.2	Compensation of the effect of the battery discharge by adjusting the PWM commands	97
5.4	Impact of the controller choice over the battery discharge	99
6	Compensation of the effects of the electrical subsystem	102
6.1	Methods and materials	102
6.1.1	Parrot Mambo	103
6.1.2	Numerical linearization of the attitude control loop	106
6.1.3	Controller design for the altitude control loop	107
6.1.4	Controller design for the attitude control loop	109

6.1.5	Description of the altitude control loop simulation and experiments	110
6.1.6	Description of the attitude control loop simulation and experiments	112
6.1.7	Description of the trajectory simulation and experiments	114
6.2	Simulated location of the closed-loop poles and system response as the battery voltage drops	115
6.2.1	Altitude control loop	115
6.2.2	Attitude control loop	116
6.3	Battery-aware controller design simulated results	118
6.3.1	Altitude control loop	118
6.3.2	Attitude control loop	120
6.4	Adjusted command compensation simulated results	121
6.5	Experimental results for the battery-unaware and battery-aware controllers .	124
6.5.1	Altitude control loop	124
6.5.2	Attitude control loop	127
6.6	Experimental results for the adjusted command compensation	131
6.7	Experimental results for the impact of the controller choice over the energy consumption	133
7	Conclusion	138
7.1	Research results	138
7.2	Future works	140
	Bibliography	153

List of abbreviations, acronyms and symbols

α	Maximum charge of a battery
β	Diffusion parameter of the electroactive species in the electrolyte
ν_ρ	Vector of the attitude pseudo-control signals
Ω	Rotational speed state variables vector
ρ	Rotational position state variables vector
ρ_R	Vector of the attitude reference signals
τ	Torque vector
τ_C	Commanded torques vector
d	Translational position state variables vector
e_ρ	Vector of the attitude errors
$e_{I\rho}$	Vector of the integrals of the attitude errors
$K_{\dot{e}_\rho}$	Vector of the derivative gains of the attitude error controller
K_{e_ρ}	Vector of the proportional gains of the attitude error controller
$K_{e_{I\rho}}$	Vector of the integral gains of the attitude error controller
v	Translational speed state variables vector

\mathbf{B}	Control allocation matrix
\mathbf{J}	Moments of inertia matrix
$\mathbf{R}_{I_o L_o}$	Rotation matrix, from inertial to local frame
$\mathbf{R}_{L_o I_o}$	Rotation matrix, from local to inertial frame
$\mathbf{S}(\boldsymbol{\rho})$	Coupling matrix
μ	Dimension of the electrolyte
ν_Z	Altitude pseudo-control signal
ω_0	Natural frequency of the reference model
ω_i	Angular velocity of motor i
$\omega_{i,C}$	Commanded angular velocity for motor i
$\omega_{i,PWM}$	PWM signals corresponding to the commanded angular velocity of the motor i
Φ	Rotation angle around the x axis, roll
Ψ	Rotation angle around the z axis, yaw
ρ	Depth of discharge
σ_d	Charge lost
σ_u	Unavailable charge
Θ	Rotation angle around the y axis, pitch
ξ	Ratio between the actual battery voltage and the nominal battery voltage
ζ_0	Damping coefficient of the reference model
$A(t)$	State of charge
b	Viscous friction coefficient
C	Concentration of the electroactive species in the electrode

C^*	Concentration of the electroactive species in the electrode for a fully charged battery
c_j	Capacitance of a capacitor belonging to an RC parallel circuit j
D_i	Duty cycle of motor i
D_i^*	Duty-cycle obtained as a function of the battery voltage v_b
e^-	Electron
e^-	Electrons
e_Z	Altitude error
e_{IZ}	Integral of the altitude error
F	Faraday's constant
$f(\cdot)$	Function which assigns to a state of charge value $A(t)$ an open circuit voltage value $v_{oc}(t)$
g	Gravity acceleration on planet Earth
i_b	Battery current
i_i	Current of motor i
J^P	Combined inertia of the rotor and the propeller
J_x	Vehicle moment of inertia along the x axis
J_y	Vehicle moment of inertia along the y axis
J_z	Vehicle moment of inertia along the z axis
K_e	Proportional gain
k_e	Motor torque constant
k_N	Propeller torque or drag coefficient
k_t	Thrust coefficient

$K_{\dot{e}}$	Derivative gain
K_{e_I}	Integral gain
L	Moment around the roll axis
l	Geometric distance between the propellers and the vehicle center of gravity
l_a	Motor armature inductance
L_b	Battery discharge time
L_C	Commanded moment around the roll axis
M	Moment around the pitch axis
m	Vehicle mass
M_C	Commanded moment around the pitch axis
N	Moment around the yaw axis
N_C	Commanded moment around the yaw axis
O	Oxidized species
p	Rotation speed around the x axis
q	Rotation speed around the y axis
R	Reduced species
r	Rotation speed around the z axis
r_a	Motor armature resistance
r_s	Series resistance of the ECM battery model
r_j	Resistance of the resistor belonging to an RC parallel circuit j
S	Surface area of the electrode
T	Total thrust along the z axis

T_C	Commanded thrust
t_s	Sampling time
U	Translational speed along the x axis
V	Translational speed along the y axis
v_b	Battery voltage
v_{cut}	Cut-off voltage
$v_{b,0}$	Nominal battery voltage
v_{cj}	Voltage drop for RC parallel circuit j
v_{oc}	Open-circuit voltage
W	Translational speed along the z axis
X	Position in the X axis
Y	Position in the Y axis
Z	Position in the Z axis
Z_R	Altitude reference signal
6-DOF	Six degrees of freedom model
BLE	Bluetooth Low Energy
D	Constant associated with the diffusion coefficient of the electroactive species
ECM	Equivalent Circuit Model
EIS	Electrochemical Impedance Spectroscopy
ESC	Electronic Speed Controller
FCS	Flight Control System
IMU	Inertial Measurement Unit

J Flux of the electroactive species

LiPo Lithium-Polymer

MSE Mean Square Error

NDI Nonlinear Dynamic Inversion

PSO Particle Swarm Optimization

PWM Pulse Width Modulation

SISO Single Input Single Output

SOC State of charge

SQP Sequential Quadratic Programming

UAV Unmanned Aerial Vehicle

List of Figures

1.1	Comparison of volume and mass relative to energy for different types of batteries.	2
1.2	Quadrotor examples, with applications in agriculture (a), racing (b), filming (c), and firefighting (d). Sources: Wikipedia, DJI, and Nevonprojects. . . .	3
1.3	Example of the battery voltage of a quadrotor mini drone during flight. . . .	4
2.1	Visual representation of the literature review for LiPo battery models. . . .	13
2.2	Visual representation of the literature review for Electrical subsystem on quadrotors.	16
2.3	Visual representation of the literature review for Energy efficiency on quadrotors.	18
3.1	Comparison between the "+" and "x" quadrotor configurations.	20
3.2	Positive roll, pitch, and yaw for an "x" configuration.	21
3.3	Sketch of a quadrotor in "x" configuration with a local and an inertial reference frame.	22
3.4	Integrated conversion for the commanded motor speeds.	25
3.5	Sensorless ESC setup.	26
3.6	Closed-loop ESC setup.	26
3.7	A quadrotor mini drone electrical diagram.	27
3.8	Nonlinear dynamic inversion control block diagram.	34
3.9	Block diagram of a second order reference model.	38
3.10	Block diagram of the altitude control system.	40
3.11	Block diagram of the attitude control system.	40
3.12	Integrated system of a quadrotor mini drone.	41

4.1	Representation of the lithium ions diffusion during the battery discharge.	44
4.2	Representation of the different states of the battery regeneration process.	45
4.3	Electrical model for a LiPo battery.	54
4.4	Block diagram of the battery model implementation.	57
4.5	Experimental setup used to collect battery discharge data.	58
4.6	Example of the constant current discharge test currents.	59
4.7	Example of the low current discharge test currents.	60
4.8	Example of the pulsed current discharge test currents.	61
4.9	Comparison between experimental data and model prediction for constant current discharge times (GREPOW).	62
4.10	Estimation error for constant current discharge times (GREPOW).	63
4.11	Open circuit voltage estimation results for cell 1 (GREPOW).	64
4.12	Open circuit voltage estimation results for cell 2 (GREPOW).	65
4.13	Open circuit voltage estimation results for cell 3 (GREPOW).	65
4.14	Model response for the constant current estimated β	68
4.15	Model responses for battery 1 (GREPOW).	71
4.16	Model responses for battery 2 (GREPOW).	71
4.17	Model responses for battery 3 (GREPOW).	72
4.18	Steps for obtaining the LiPo battery model.	75
4.19	Comparison between optimization time and mean estimation error for battery 1 (GREPOW).	77
4.20	Comparison between optimization time and mean estimation error for battery 2 (GREPOW).	78
4.21	Comparison between optimization time and mean estimation error for battery 3 (GREPOW).	78
4.22	Estimation error for constant current discharges for battery 1 (GiFi Power).	79
4.23	Estimation error for constant current discharges for battery 2 (GiFi Power).	80
4.24	Estimation error for constant current discharges for battery 3 (GiFi Power).	80
4.25	Open circuit voltage estimation results for battery 1 (GiFi Power).	81
4.26	Open circuit voltage estimation results for battery 2 (GiFi Power).	82
4.27	Open circuit voltage estimation results for battery 3 (GiFi Power).	82

4.28	Model responses for battery 1 (GiFi Power).	83
4.29	Model responses for battery 2 (GiFi Power).	83
4.30	Model responses for battery 3 (GiFi Power).	84
5.1	Illustration of a quadrotor during hover (a) and while tilting around the Y axis (b).	100
6.1	Photos of the Parrot Mambo without (a) and with (b) a flexible protection cage.	103
6.2	Simulink block diagram model of the Parrot Mambo.	104
6.3	Simulink model of the Flight Control System of the Parrot Mambo.	104
6.4	Simulink model of the electrical subsystem of the Parrot Mambo.	105
6.5	3D visualization of the Parrot Mambo during flight in the simulated environment.	105
6.6	Model employed for the numerical linearization. The input is (a) and the output is (b).	107
6.7	Reference altitude maneuver.	111
6.8	Photos of the Parrot Mambo performing the maneuver shown in Fig. 6.7, at 1.1 m (a) and 1.5 m (b).	111
6.9	Reference attitude maneuver.	113
6.10	Photos of the Parrot Mambo performing the maneuver shown in Fig. 6.9, at the initial position (a) and 1.5 m forward (b).	113
6.11	Reference trajectory used in the experiments.	114
6.12	Altitude system poles for the linear approximation of the altitude control loop, designed with a battery-unaware controller.	115
6.13	Simulated altitude error transient response using battery-unaware controller design.	116
6.14	Attitude system poles for the linear approximation of the attitude control loop, designed with a battery-unaware controller.	117
6.15	Simulated attitude error transient response using battery-unaware controller design.	118
6.16	Altitude system poles for the linear approximation of the altitude control loop, designed with a battery-aware controller.	119

6.17	Simulated altitude error transient response using battery-aware controller design.	119
6.18	Simulated attitude error transient response using battery-aware controller design.	120
6.19	Attitude system poles for the linear approximation of the altitude control loop, designed with a battery-aware controller.	121
6.20	Simulated altitude error transient response for the non-compensated and compensated command generation.	122
6.21	Simulated altitude error transient response for the non-compensated and compensated command generation, from 27.5 until 32.5 s.	122
6.22	Simulation result for the battery voltage for the non-compensated and compensated command generation.	123
6.23	Altitude response of the battery-unaware controller.	124
6.24	Altitude response of the battery-aware controller.	125
6.25	Experimental altitude error transient responses for different intervals of ξ using the battery-unaware controller design.	126
6.26	Experimental altitude error dynamics for different bands of ξ using the battery-aware controller design.	127
6.27	Comparison of the battery voltage v_b observed in both the battery-unaware and battery-aware cases for the altitude.	128
6.28	Attitude response of the battery-unaware and battery-aware controllers.	128
6.29	Experimental attitude error transient responses for different intervals of ξ using the battery-unaware controller design.	129
6.30	Experimental altitude error transient responses for different intervals of ξ using the battery-aware controller design.	130
6.31	Comparison of the battery voltage v_b observed in both the battery-unaware and battery-aware cases for the attitude.	130
6.32	Experimental altitude error transient response for the normal and compensated command generation.	131
6.33	Experimental altitude error transient response for the normal and compensated command generation, 27.5 to 32.5 s.	132

6.34	Battery voltage during flight for the non-compensated and compensated command generation.	132
6.35	Square trajectory performed by the quadrotor mini drone with different reference models.	133
6.36	Altitude and attitude responses for the square trajectory, $\omega_p = 100$	134
6.37	Altitude and attitude responses for the square trajectory, $\omega_p = 200$	135
6.38	Comparison of the altitude and attitude absolute errors for the square trajectory.	136
6.39	Comparison of the battery voltages for the square trajectory.	137

List of Tables

4.1	Open circuit voltage estimation error metrics for battery 1.	66
4.2	Open circuit voltage estimation error metrics for battery 2.	66
4.3	Open circuit voltage estimation error metrics for battery 3.	66
4.4	Battery voltage estimation error metrics for battery 1.	72
4.5	Battery voltage estimation error metrics for battery 2.	73
4.6	Battery voltage estimation error metrics for battery 3.	73
4.7	Execution time for the optimization algorithms.	75
4.8	Model parameters for battery 1, interior point (GREPOW).	76
4.9	Model parameters for battery 2, interior point (GREPOW).	76
4.10	Model parameters for battery 3, interior point (GREPOW).	76
4.11	Model parameters for battery 1, interior point (GiFi Power).	84
4.12	Model parameters for battery 2, interior point (GiFi Power).	84
4.13	Model parameters for battery 3, interior point (GiFi Power).	85
6.1	Parrot Mambo parameters.	106

Chapter 1

Introduction

This thesis is a study on quadrotor mini drones powered by lithium-polymer batteries, specifically on how the components of the electrical subsystem in these vehicles affect their behavior during flight and how to devise strategies for their control that take these effects into account. It is shown that the system behavior degrades due to the battery discharge during flight and that if components such as the motor are not considered in the modeling phase, the resulting altitude and attitude error controllers will not achieve the desired performance. Changes to the controller design and the command generation are proposed to mitigate these factors. In this chapter, the thesis motivation, objectives, and methodology are described, as is the document structure. To better situate them in the context of this research, an introduction to what quadrotors are is given.

1.1 Introduction to quadrotors

Quadrotors are a subset of a wider category of flying robots, called UAVs (Unmanned Aerial Vehicles). These vehicles can either operate autonomously or be remotely controlled to perform several tasks [Boukoberine, Zhou & Benbouzid 2019]. While the initial application for this type of vehicle was for military reconnaissance, intelligence, and surveillance [Kim, Gadsden & Wilkerson 2020], as microprocessor technology advanced and production costs became cheaper, they became popular for civilian applications such as delivery, aerial filming and smart farming [Maddikunta et al. 2021].

While UAVs can be classified into many categories, including different types of wings,

sizes, and power sources, in this work the focus is battery-powered quadrotors. They are classified as a type of rotary wing drone [Hassanalian & Abdelkefi 2017], as they rely on propeller-based systems to generate lift. These vehicles are capable of flying in all directions, either horizontal or vertical, and, critically, hover in a fixed position. This capability, in addition to their comparatively small size, when compared to fixed-wing UAVs makes them particularly desirable for applications in confined and hard-to-reach locations [Shraim, Awada & Youness 2018]. While rotary wing vehicles can range in the number of motors, the most common configurations are those with four and six motors, respectively named quadrotors and hexacopters.

Quadrotors are more energetically efficient than their six-motor counterparts due to their reduced mass and also tend to be cheaper. They are typically powered by Lithium-Polymer (LiPo) batteries [Hassanalian & Abdelkefi 2017], which provide a high energy-to-mass ratio at a relatively low cost. This is shown in Fig. 1.1, where a comparison of how the volume and weight relate to energy for Lead-Acid, Nickel-Cadimium, Nickel-metal hydride, Lithium-ion, and Lithium-Polymer batteries. Even then, flight endurance remains an important limitation for this type of vehicle. Other alternatives, such as hydrogen-based fuel cells, have been proposed, but their widespread adoption is still dependent upon an improvement of accessibility and price [Belmonte et al. 2018]. Examples of different quadrotors can be seen in Fig. 1.2.

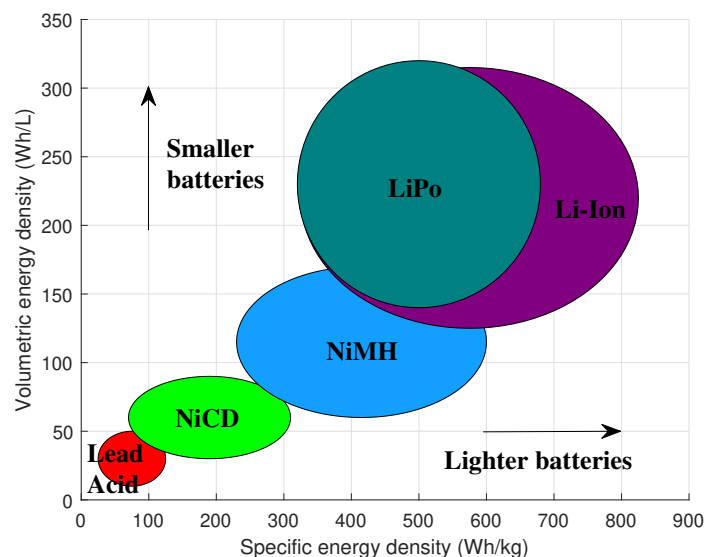


Figure 1.1: Comparison of volume and mass relative to energy for different types of batteries.

The references [Boukoberine, Zhou & Benbouzid 2019] and [Kim, Gadsden & Wilkerson 2020] place quadrotors powered by LiPo batteries as an interesting research topic, due to their wide range of possible applications, and several research challenges available, such as choice of flight control strategy, model-based design approaches, path planning, and estimation of flight autonomy.



(a)



(b)



(c)



(d)

Figure 1.2: Quadrotor examples, with applications in agriculture (a), racing (b), filming (c), and firefighting (d). Sources: Wikipedia, DJI, and Nevonprojects.

Although many of the principles which will be used in this work when developing the quadrotor motor are general in nature, the proposed contributions will be tested and explored for a quadrotor mini drone, which is a subset of quadrotors composed of small and light aircraft.

1.2 Motivation

The fundamental motivation of this research is to determine whether the current system design process for quadrotor mini drones can be improved by considering the behavior of the electrical subsystem. This question can be expanded upon by exploring the description given

in section 1.1. It was mentioned that these vehicles are battery-powered, which implies a varying power source, since as the vehicle performs the desired movements, the voltage at the battery terminals drops and the available energy diminishes. An example can be seen in Fig. 1.3, where the measured voltage at the battery terminals is shown for a quadrotor mini drone performing a square trajectory flight. After an initial drop due to the high current demand for the take-off, the voltage drops during the whole flight. If this is ignored, it will generate a negative effect on the system's performance, as the available voltage at the actuators will be different from a presumed nominal value. The investigation of the related works in Chapter 2 will show that few works take this factor into account during system design, most of which employ simple linear models for the battery, which is a nonlinear system. This investigation can be extended to the other components of the electrical subsystem, such as the propulsors, which are electrical motors.

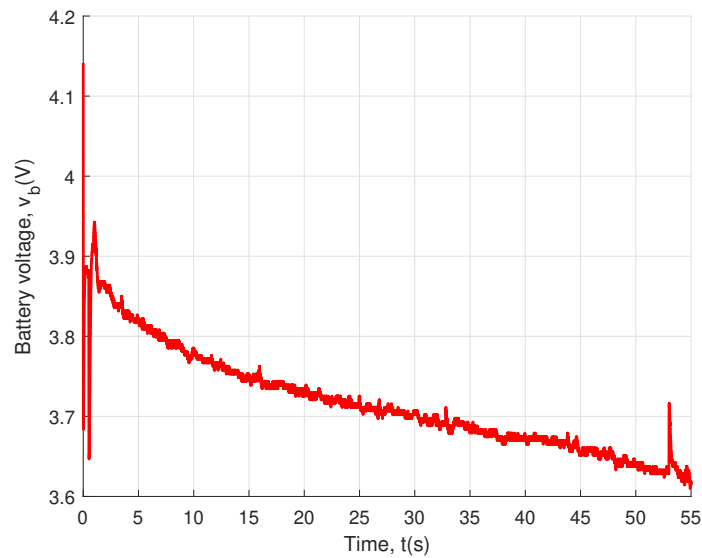


Figure 1.3: Example of the battery voltage of a quadrotor mini drone during flight.

Since the effect of the electrical subsystem over the closed-loop dynamics is being studied, flight autonomy and energy efficiency also become relevant, as possible changes in the system design will affect them. There are plenty of works that treat the problem of energy-efficient path planning, but very few analyze the impact of factors such as the controller design or how the commands for the motors responsible for moving the vehicle are generated.

These facts show that there is space for advances by including the electrical subsystem in the design flow of control systems for quadrotor mini drones. This requires more realistic mathematical models, by means of the inclusion of a nonlinear battery model and other components of the electrical subsystem. This more complex model enables changes in the design process for quadrotor mini drone vehicles, such as controllers that compensate for the effect of the battery voltage over the closed-loop dynamics and different strategies for generating the motor commands. The effectiveness of these must be evaluated, examining if there are any performance gains and the presence of possible trade-offs.

1.3 Objectives

From the motivation, the following research objectives can be established:

- Develop a model for a battery-powered quadrotor mini drone, including the relevant cinematic and dynamic equations, the model of the motors, and how the commands are sent to them. This includes how the altitude and attitude of a quadcopter are controlled, how it tracks position and attitude, and what sensors are used for this purpose. A model of the electrical subsystem must also be derived, including the LiPo battery responsible for powering all of the system components during flight and the motors of the propulsion system. All of these should be integrated into a single model which describes how the quadrotor mini drone behaves.
- Having established a system model, demonstrate the effect of the variation in the battery voltage over the altitude and attitude closed-loop dynamics. This leads to an analysis of whether the intended system behavior considered during the controller design will be attained.
- Provided that the effect of the electrical subsystem over the system dynamics is shown to be detrimental, propose strategies, through changes in the system design, which aim to mitigate losses in performance.
- Analyze how the choice of different closed-loop attitude specifications might impact the battery discharge rate.

1.4 Methodology

Having established the research objectives, the associated methodology can be explained. The first step was to review the relevant literature, through searches in research databases, so that the available spaces for contributions might be delineated. This was a continuous process during the elaboration of the work presented here, as new works are constantly being published.

In parallel with the investigation of the relevant research literature, a study was conducted regarding the definition of a platform in which the desired research objectives could be pursued. This goes through how quadrotor mini drones work at a physical level, by understanding the models of the relevant system components. Another aspect is the practical considerations pertaining to the research. Since quadrotor mini drones are flying vehicles, system failures might lead to damage, making it important to have an available simulator where the feasibility of proposed solutions might be tested beforehand. As for the experiments, it was determined what sensors were available for measuring the relevant variables, the given platform restrictions, and if the tests necessary for exploring the proposed objectives for this work were possible. Furthermore, as the interest of this research is not only to study the behavior of quadrotor mini drones but to propose modifications to it, it should be possible to modify its inner workings, through the deployment of custom controller code and different flight paths. This led to the choice of the Parrot Mambo platform, which presented a solution to these problems and allowed tests to be performed in both simulated and experimental environments.

Having established the state of the art and a platform in which to perform tests, the next step in the methodology was to explore the system model and to derive the relevant mathematical expressions for the altitude and attitude dynamics. During this study, it was verified that the battery behavior is extremely relevant to how the system performs, and also that it has a nonlinear characteristic. This led to an investigation on how to model the available LiPo batteries, including both a literature review on modeling techniques and the design of experiments to collect data so that a model might be identified, along with the investigation of all of the associated practical problems.

After the mathematical analysis of the attitude and altitude control loops was performed,

simulated tests were conducted to verify the validity of their findings. The conclusions were drawn from the mathematical analysis held in the simulation environment and a set of experiments was designed to verify them in a real-flight scenario. As the mathematical analysis indicated the negative effects of the battery discharge over the system dynamics, two solutions were proposed to deal with this problem, one through a change in the controller design process, and another through a change in how the motor commands are obtained. As with the results of the analysis, both of them were implemented in simulation and subsequently tested in an experimental environment. In parallel, an investigation on which factors contribute the most to energy consumption during flight was conducted. A hypothesis that more aggressive attitude control strategies would lead to a slower battery discharge rate was then proposed by analyzing the physical model of the quadrotor mini drone. This hypothesis was also verified in an experimental environment.

1.5 Contributions

The contributions of this research are the following:

- An analysis of the altitude dynamics of a battery-powered quadrotor mini drone is performed. This results in a nonlinear expression for the closed-loop altitude error dynamics in which the motor and the battery voltage are taken into account, in contrast with traditional models where only the cinematic and dynamic equations of the quadrotor mini drone are considered. Furthermore, a linear approximation of the resulting nonlinear expression is also defined, allowing the analysis of the effect of the drop in battery voltage over the closed-loop poles loci. The conclusion is that the altitude dynamics get slower as the battery discharges. Simulated and experimental results which corroborate the findings of the analytical demonstration are presented.
- The same analysis as above was also performed for the attitude dynamics of a quadrotor mini drone, showing the influence of the motor parameters over the closed-loop dynamics and how they are impacted by changes in the battery voltage. The pole placement as the battery discharges was also obtained, although for this case a numerical approach was adopted to linearize the system, due to several couplings between the

relevant state variables, which makes obtaining an analytical approximation nontrivial. As with the altitude dynamics, the attitude dynamics are shown to be slower for lower values of the battery voltage, although to a lesser degree than the altitude. This effect was verified on simulated and experimental results.

- Having analyzed how the system performance worsens as the battery discharges, solutions are proposed to reduce this effect. The first is a battery-aware controller design, that formulates the controller design as an optimization problem, using the nonlinear system model considering the motor and the battery obtained during the analytical demonstration. This leads to a controller which outperforms its battery-unaware counterpart when operating at lower voltage values, at the cost of a faster discharge rate. Simulated and experimental results showing the effectiveness of the proposed approach are provided.
- The second solution pertains to the generation of the commands for the motors which generate the lift that the quadrotor mini drone uses to move. It is shown that if the actual battery voltage is employed when generating these commands the actual motor angular velocity will be close to the commanded velocities, in contrast to the standard case where the nominal battery voltage is considered. This solution was implemented in simulated and experimental environments and the corresponding results are presented.
- A demonstration of how the aggressiveness of the attitude control strategy impacts the energy consumption of the vehicle is presented. This leads to the hypothesis that more aggressive control strategies lead to a slower battery discharge during the flight when compared to less aggressive strategies, due to the reduced transient regime. This hypothesis is tested in an experimental setting.

1.6 Document structure

This document is structured as follows: in Chapter 2 a literature review is conducted in the relevant research areas, showing where this research is located in the state of the art. Chapter 3 describes the model of a quadcopter within the context of this thesis, including the

cinematic and dynamic equations, components of the electrical subsystem, and the employed control laws. The battery model is described in Chapter 4. Chapter 5 presents a mathematical analysis of how the inclusion of the electrical subsystem in the quadrotor mini drone model can give new insights into its behavior, showing that the system performance deteriorates as the battery discharges. Approaches to mitigate this effect are also proposed in this chapter. In Chapter 6 the methods and materials of the simulations and experiments conducted to verify the findings of Chapter 5 are described, and the associated results are presented. Finally, Chapter 7 presents a review of the conclusions drawn from the results and points to future lines of work.

Chapter 2

Related works

In this chapter, the works related to the object of research in this document are presented. There are three main areas of research that are relevant to the results presented further in this text: the modeling of LiPo batteries, studies regarding the electrical subsystem of quadrotors, and studies regarding energy efficiency on quadrotors.

2.1 Lithium-polymer battery models

In electrically powered quadrotors, the battery is a critical component, as it is not only responsible for powering all other system components but also represents a large part of the mass. The methodology of this research includes the use of a system model. Since different quadrotors will be powered by different batteries, a study on the state-of-the-art of modeling techniques for these components is necessary so that a suitable battery model might be obtained. The focus is on LiPo batteries, as they are the most popular choice for electrically powered quadrotors due to their high energy-to-mass ratio and relatively low cost.

The model for this type of battery was formulated in [Doyle, Fuller & Newman 1993], by employing the relevant electrochemical differential equations to describe the conservation of energy and the behavior of the relevant physical variables, such as charge concentration on the electrodes and the resulting voltage at the battery terminals.

From this initial work, other authors have developed improved models, either focusing on specific phenomena or incorporating new battery technology into them. Additionally,

since the original model relies on solving a system of coupled partial differential equations, a computationally intensive problem, work was done to develop models capable of being employed in real-time applications in embedded systems. These models can be divided into three main categories: electrochemical models, Equivalent Circuit Models (ECM), and hybrid models.

The electrochemical models have the advantage of accurately representing the electrochemical phenomena that happen in the batteries. However, they are problematic for use in real-time applications due to their simulation complexity, which is why the authors propose reduced-order alternatives or more efficient methods to solve the associated differential equation system. In [Schmidt et al. 2010] a lumped parameter approach is proposed, while still modeling factors such as ion concentration on the liquid phase of the battery and the relevance of temperature in the kinetic processes. The model proposed in [Mazumder & Zhang 2013] adopts a one-dimensional approximation of the full model, while in [Daigle & Kulkarni 2013] the charge gradient dynamics in the electrode are simplified. A reduced-order electrochemical model is used in conjunction with a Kalman filter to estimate the State of Charge (SOC) of LiPo batteries in [Li & Choe 2013]. The critical problem related to the use of these models is the need to have knowledge of constructive battery parameters, such as the electrode dimension for the cells and the physical properties of the materials employed. Such specific parameters are not typically available in the datasheets for most off-the-shelf LiPo batteries and are difficult to measure or estimate.

By contrast, ECM models forgo the complex relations that model the physical effects of the battery in favor of representing it as an electrical circuit which, through the proper estimation of its parameters, is able to predict the battery voltage at the terminals for a given current. This approach is exemplified in papers such as [Sarikurt, Ceylan & Balikci 2014], [Miniguano et al. 2020], [Tran et al. 2021] and [Sarsembayev et al. 2022]. All ECM-based models need to address the problem of how to calculate the open-circuit voltage of the battery, which is a function of the SOC. The simpler way to obtain an estimate of the SOC is by integrating the current signal, but in this case, the relevant nonlinear effects due to the diffusion of the Lithium ions along the electrolyte are not considered. To compensate for this, many of these works will employ complementary strategies to estimate the SOC. For example, in [Mao, Zhao & Lin 2014] a sliding mode observer is employed to compensate for

the error in the SOC estimation, a problem also studied in [Chen et al. 2016]. Approaches based on Kalman filters can be seen on [Topan et al. 2017], [Wu, Li & Du 2018], [Gjengedal, Vie & Molinas 2017] and [Anggraeni et al. 2022]. Other works use other methods such as particle swarm optimization [Kim, Qiao & Qu 2013], genetic algorithm [Paschero et al. 2010], artificial neural networks [Kuchly et al. 2021] and bayesian filtering [Zhao, Wenzl & Bohn 2012] to solve this problem. In [Tran et al. 2020] a hysteresis effect is added to an ECM model to improve its accuracy. Another solution is to map the SOC to the open circuit voltage by employing a mathematical expression in conjunction with the experimental data of a low current discharge test, as shown in [Rahimi-Eichi, Baronti & Chow 2014]. The use of Electrochemical Impedance Spectroscopy (EIS) can be seen in [Stanciu et al. 2015] and [Mc Carthy et al. 2022]. This technique estimates the parameters of the ECM by exciting the battery over a wide range of frequencies and analyzing the harmonics of the resulting spectra.

Hybrid models combine the ECM and electrochemical approaches. The aim is to obtain a model that still has a physical representation of the relevant phenomena, being able to provide an estimation of the SOC without the need for corrections, while also employing the simple and efficient implementation of the electrical circuit-based models. Examples of this type of model can be seen in [Li, Xiao & Choe 2011] and [Li et al. 2011], where the SOC is obtained by means of a model based on porous electrode theory. However, these models still rely on the knowledge of the battery's constructive parameters.

The model proposed in this work is of the hybrid category, employing an ECM in conjunction with the estimate of the SOC provided by the Rakhmatov-Vrudhula diffusion model [Rakhmatov & Vrudhula 2001], which was employed in studies for Lithium-ion batteries in works such as [Spohn et al. 2008] and [Neves et al. 2016]. It adopts a one-dimensional approximation to solve the system of differential equations of the battery model, resulting in a lumped parameter model which can provide both the available and unavailable charge for a given current, thus forgoing the need for complementary techniques to correct the estimation of the SOC. This work hypothesizes that the Rakhmatov-Vrudhula model can be applied to LiPo batteries due to employing the same mathematical modeling for the diffusion process as the original model proposed in [Doyle, Fuller & Newman 1993], which is based on Fick's law, as seen in [Bard & Faulkner 1980].

The findings of this literature review are summarised through a visual representation in Fig. 2.1. The cited papers are divided by type and small notes mention their specific approaches and differences. The figure shows that the proposed battery model comes from hybrid models, which are themselves derived from the ECM and electrochemical models, but it employs the Rakhmatov-Vrudhula diffusion model, instead of being derived from other LiPo battery models.

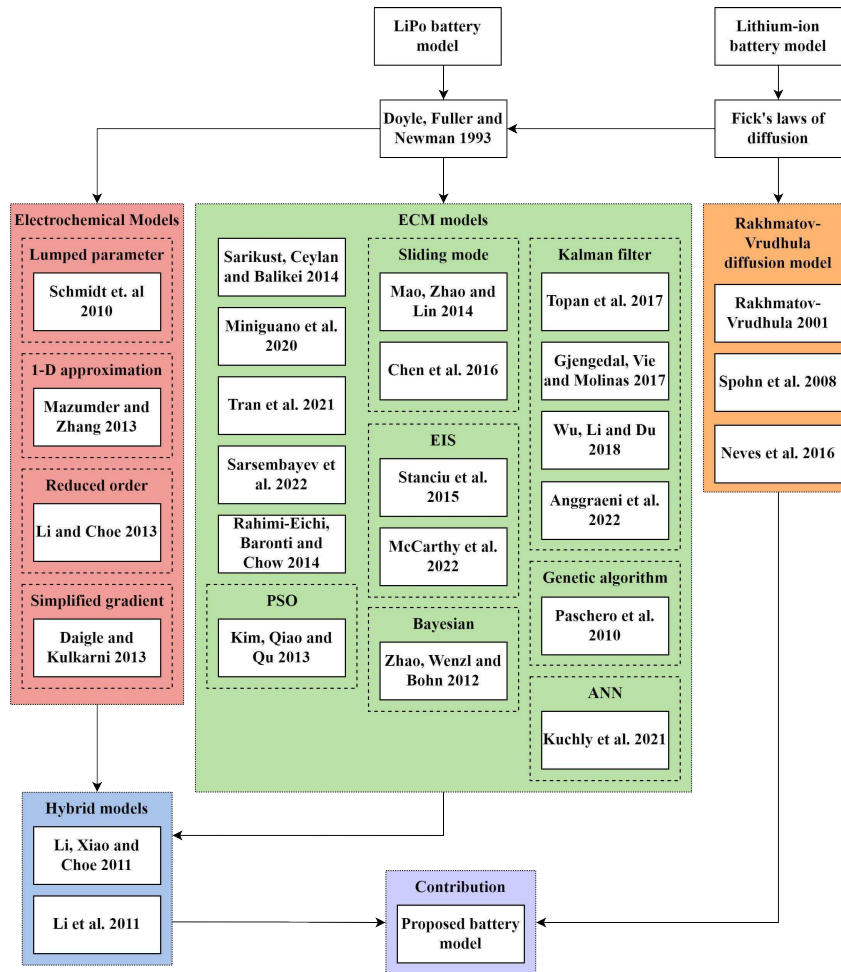


Figure 2.1: Visual representation of the literature review for LiPo battery models.

2.2 Electrical subsystem on quadrotors

The electrical subsystem in a quadrotor is formed by the battery and the propulsors. As such, it contains both the power source and the system actuators and should be taken into account during the design process. In this work, the impact of this subsystem over the closed-loop dynamics is analyzed through its models, and as such, other works which have explored this field must be studied.

Two categories of works appear in this field: those which investigate the impact of the behavior of specific components of the electrical subsystem over the quadrotor dynamics and those that aim to provide design guidelines such that a vehicle can be built taking into consideration a given restriction or a desired purpose. In the latter category, one can refer to a work such as [Lim, Kim & Yee 2021], where a systematic method for the design of quadrotors is proposed, and an algorithm for the analysis of the electric propulsion system is presented. In [Zhang et al. 2021] and [Li et al. 2021] the problem of how to optimize the choice and design of the system components such that environmental wind disturbances might be rejected is studied. A method for optimizing the component selection for the propulsion system according to the system requirements is explored in [Shi et al. 2017], but only the steady-state behavior is considered. Such a method is also the research subject of [Dai et al. 2019], but only a linear battery model was considered as the power source. The restriction imposed upon the vehicle design in [Benito et al. 2014] is a heavy payload requirement for small-sized aircraft, while in [Vu, Dang & Dinh 2019] the goal is to design the electrical subsystem for a quadrotor for use in agriculture. While these works present important guidelines for designers, due to their wide scope several of the system components are assumed in their simplified forms, and the system dynamics are not fully explored.

When it comes to the focus on specific components, studies such as [Falconí et al. 2013] show that the system performance is heavily dependent on the generated thrust from the motors, and then explore different thrust control laws. A study of how the internal battery dynamics affect the flight and control performance is conducted in [Podhradský et al. 2013]: those authors have concluded that when the battery is partly discharged, it provides less output power than when it is fully charged. Experimental test results where this effect appears are presented. As a consequence, the actuators and the UAV dynamics become slower. An

augmented thrust controller with a battery compensation block was proposed, but no design guideline for determining the controller gains was provided. Furthermore, their results were limited to an experimental platform that dealt with thrust for a single motor, instead of a vehicle in-flight. This work was expanded with in-flight tests in [Podhradský, Coopmans & Jensen 2014], but the implemented altitude controller had an error within 1 *m* of the intended setpoint. This same effect was studied in [Yahui, Shaolei & Cong 2014] and in [Szafranski, Czyba & BŁachuta 2014], where the nonlinear model for the propulsion system of a UAV is proposed, verifying the effect of different energy levels in the thrust obtained on an experimental setup. This setup did not involve an in-flight vehicle and the main interest was restricted to the modeling problem. The same effect was studied in [Jee, Cho & Kim 2020], focused on modeling the quadrotor actuators while taking undefined hardware errors into account.

The work presented in this thesis shows an analysis of the closed-loop altitude and attitude dynamics of a quadrotor, showing how the electrical subsystem affects them, especially because of the varying battery voltage. Moreover, as these effects are deemed detrimental to the system, compensation techniques through changes in the controller design and motor command generation are proposed and implemented for an in-flight vehicle.

The findings of this literature review are summarised through a visual representation in Fig. 2.2, where the proposed contributions are shown as being an extension of both the works that have previously explored the effects of the electrical subsystem and those which aim to improve the design process. It should be noted that when it comes to the design, the focus of this work is on the flight controller and the command generation, which are more specific in scope than most works in this area but are nevertheless critical components of a quadrotor.

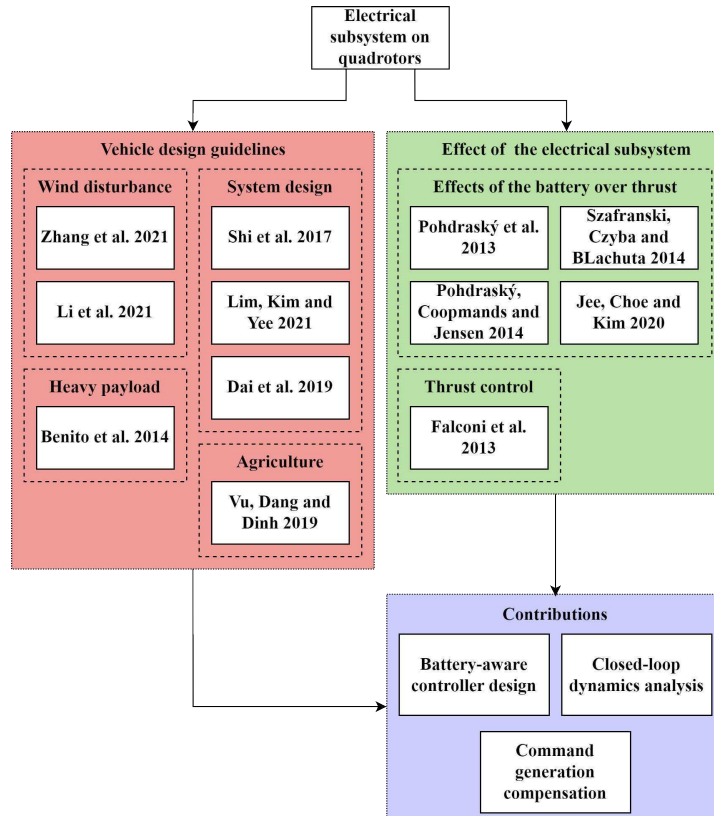


Figure 2.2: Visual representation of the literature review for Electrical subsystem on quadrotors.

2.3 Energy efficiency on quadrotors

The last stage of this literature review is to explore the works which deal with energy efficiency for quadrotors. More specifically, having determined the nature of the relationship between the desired vehicle dynamics and the electrical subsystem, the next step is to consider solutions that optimize the system behavior with regard to its energy consumption. This research topic is relevant since even though LiPo batteries have a high energy-to-mass ratio, rotary-wing vehicles tend to have a high energy consumption rate, leading to low flight autonomy. Therefore gains in energy efficiency are very desirable.

The first category of papers in this field is those concerned with minimizing energy spent when the quadrotor is commanded to perform a mission. One of the most common ways to deal with this problem is to define path planning as an optimization problem in which the energy spent must be minimized, typically employing a battery model, as can be seen in

[Schacht-Rodríguez et al. 2018], [Morbidi, Cano & Lara 2016] and [Yacef et al. 2017]. The conditions for optimizing the path planning may change according to the desired application, such as considering the effect of the wind [Azevedo et al. 2018], application in photogrammetry [Franco & Butazzo 2016][Cabreira et al. 2018] or meeting the requirements for distributed cellular networks [Chou, Pang & Yu 2020][Galán-Jiménez et al. 2021]. While all of these approaches are valid, they deal with the outermost control loop of quadrotors, which is the control of lateral position, ignoring effects that might increase the energy consumption in the inner control loops for altitude and attitude.

Another approach is to consider energy efficiency in the design of the controller itself. In [Wang, Wang & Ren 2022] an attitude controller where the energy consumption is considered is proposed, by establishing a bound within which the system must operate, restricted to cases where no aggressive maneuvers are performed during flight. A controller for path-following is proposed in [Gandolfo et al. 2017] based on the relationship between vehicle speed and consumed energy, showing that energy gains can be achieved when the trajectory requirement is made of fixed points that must be reached by the vehicle, regardless of time restrictions. A comparison between different control strategies is performed in [Gandolfo et al. 2017], with the results indicating that one must be careful when drawing conclusions about the advantages of one control strategy over another.

In all of these cases, the prediction of the flight time is important, so that missions might be designed such that a given quadrotor has enough flight autonomy to perform them. Different approaches to solve this problem are studied in [Sierra et al. 2019], [Abdilla, Richards & Burrow 2015] and [Schacht-Rodríguez et al. 2018], although all of them have in common the use of a battery model with a linear SOC to generate the flight time predictions.

Other works try different approaches. The work presented in [Horn et al. 2019], considers the impact of component choice over energy consumption, looking at the effects of different propellers in a hybrid quadrotor. Works such as [Voznesenskii 2021] and [Zhao et al. 2018] deal with strategies for automated battery replacement or recharging. In these works, energy efficiency is considered for a system where one or more vehicles are performing given tasks, and the goal is to reduce the downtime due to discharged batteries.

Considering the works presented above, the discussion regarding energy efficiency in this thesis is performed at a lower level, concerning the impact of the aggressiveness of the

attitude control strategy over the energy consumption, which is not performed in [Wang, Wang & Ren 2022] and [Gandolfo et al. 2017]. In addition, a nonlinear battery model was used to evaluate the discharge, in place of simplified models that presume a linear behavior from the battery.

This literature review is summarised through a visual representation in Fig. 2.3. This is a wide field of research, with multiple proposals for solving different facets of the energy efficiency problem. This is reflected by the relation between the proposed contribution and the previous works shown in Fig. 2.3, which aims to look at energy efficiency within the context of how the choice of aggressive closed-loop dynamics might affect energy consumption.

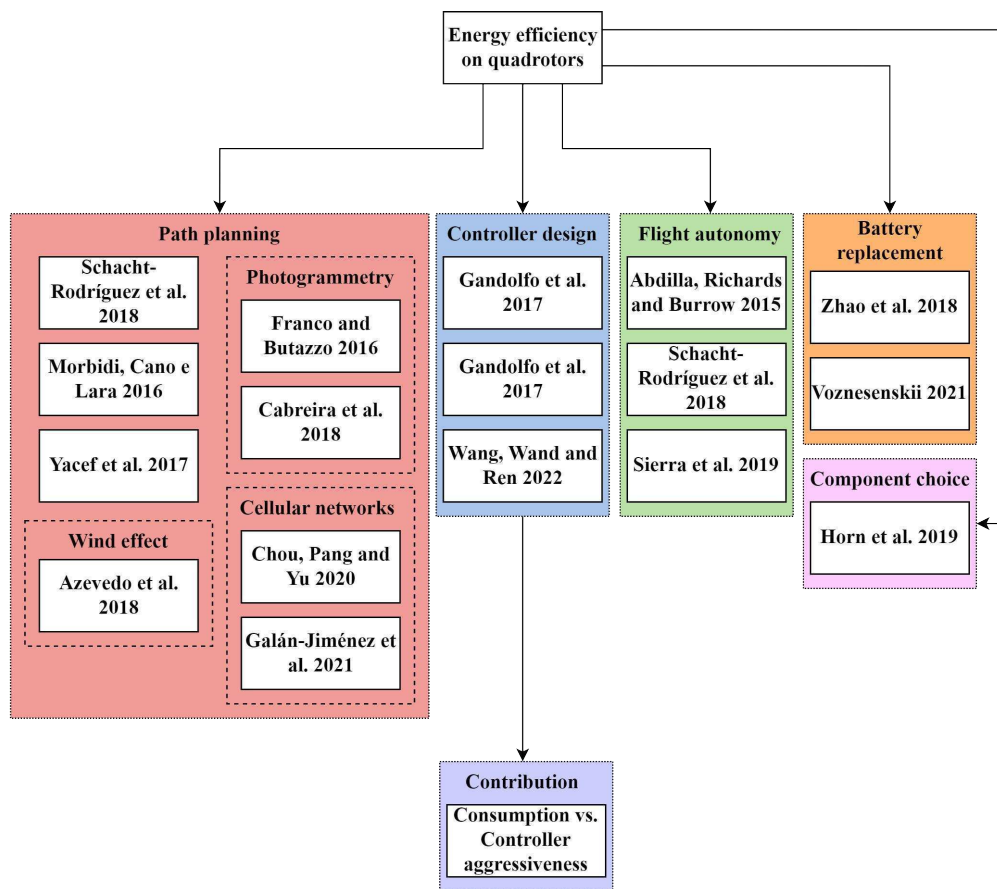


Figure 2.3: Visual representation of the literature review for Energy efficiency on quadrotors.

Chapter 3

Model of a quadrotor mini drone

In this chapter, the model of a quadrotor is presented, encompassing the basic concepts for this type of vehicle, the six degrees of freedom model (6-DOF) equations for an object moving through space, and the associated state variables and the components of the electrical subsystem. This chapter also contemplates the command generation strategy and the control law employed in this study, along with how all of the system components relate to one another. Of note, the model of the battery, which is a component of the electrical subsystem, will be presented in detail in the subsequent chapter.

3.1 Basic concepts

The quadrotor is considered to be a rigid structure with four arms of the same dimensions fixed to a central body. A propulsor, made of a propeller rigidly coupled to a motor, is placed at the end of each of the arms. Two of these motors spin clockwise, while the other two spin counter-clockwise. The placement of the components is such that the center of mass can be considered sufficiently close to the geometric center of the vehicle. This configuration can be achieved in two different forms: with the vehicle arms being aligned with the horizontal axes of the inertial reference plane, called a cross configuration "+", or with the arms forming a 45° angle in relation to this same axes, called an x configuration "x". These configurations are both shown in Fig. 3.1. A quadrotor is a sub-actuated system, as it possesses only four actuators to which commands can be sent, in the form of the motors, but has six degrees of freedom.

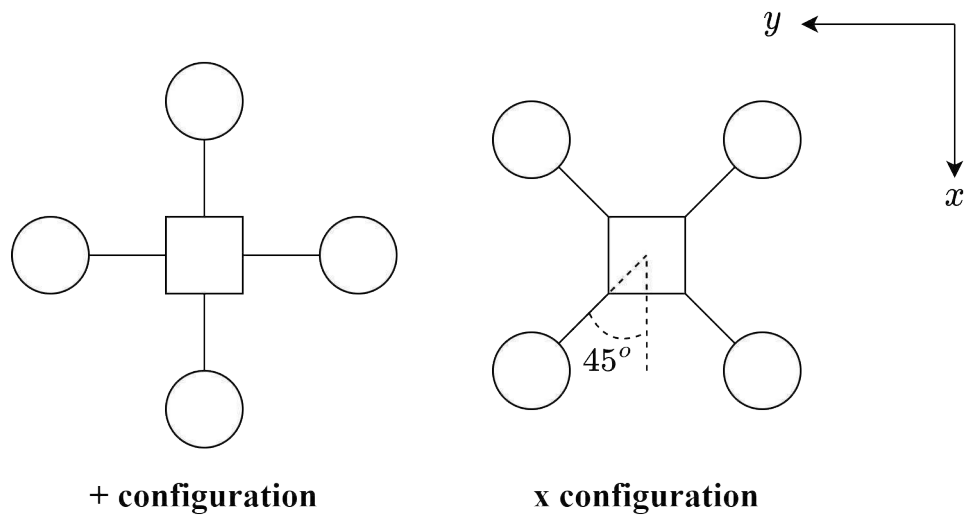


Figure 3.1: Comparison between the "+" and "x" quadrotor configurations.

The variables used to control the system are the thrust, roll angle, pitch angle, and yaw angle. The thrust is defined as the resulting force along the vertical axis of the inertial reference frame and is the variable most closely associated with changes in vehicle altitude. Therefore, the thrust command is achieved by changing all four motor speeds at the same intensity. The roll angle, or simply roll, is the angle formed by performing a rotation around the x axis of the inertial reference frame. In an "x" configuration, a positive roll command is achieved by increasing the speed of the motors to the left of the x axis and decreasing the speed of the motors to the right. The pitch angle is analogous to the roll, but for the y axis instead. A positive pitch is achieved by increasing the speed of the motors to the right of the y axis and decreasing the speed of those to the left. The yaw angle is the rotation around the z axis, and a positive yaw command is achieved by increasing the speed of the motors spinning clockwise and decreasing the speed of the motors spinning counter-clockwise. These movements are demonstrated in Fig. 3.2.

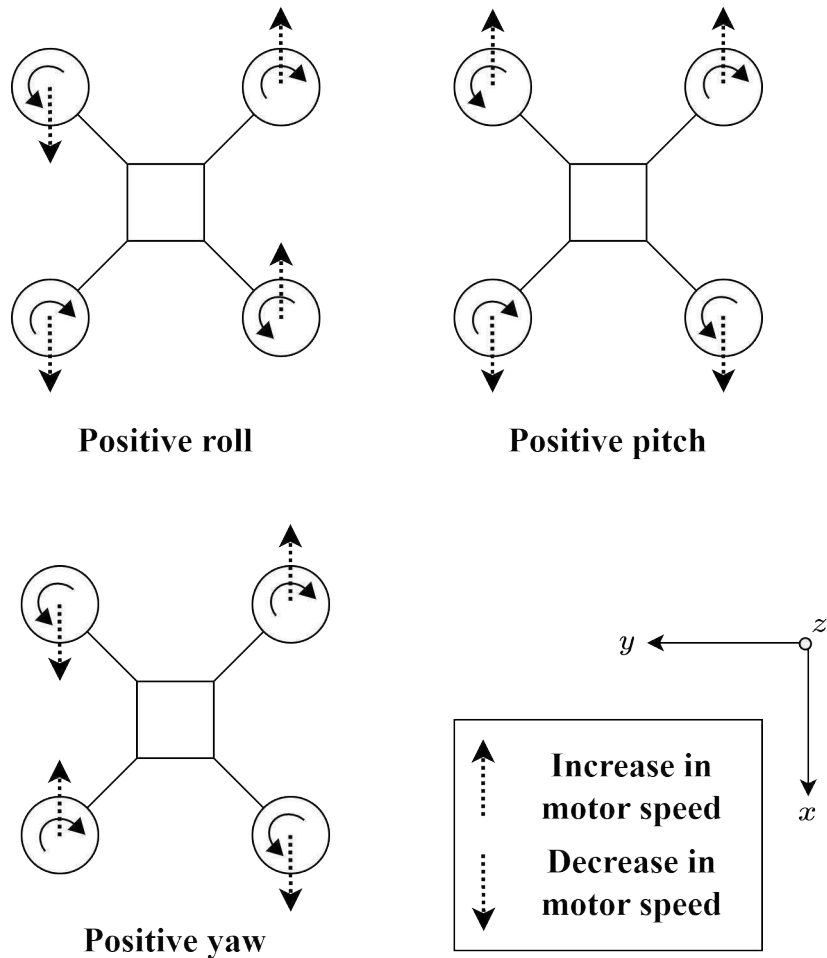


Figure 3.2: Positive roll, pitch, and yaw for an "x" configuration.

Due to these four variables being defined as the control outputs, a cascading control structure is typically adopted for this type of vehicle, where attitude, which is considered to be the set of the roll, pitch, and yaw angles, and the altitude are part of an inner control loop, while the movement along the horizontal plane is controlled in an outer control loop. The logic is that any commands that instruct the vehicle to move a given distance along the horizontal axes are translated into variations in the attitude, while the altitude, which is a direct function of the vertical thrust, is dealt with separately. Therefore, to attain precise control of the quadrotor position, the most important factors are to implement reliable altitude and attitude controllers.

3.2 State variables

The state variables of the system are given by the following vectors:

- The translational position state variables vector in the inertial reference frame $\mathbf{d}(t) = [X(t) \ Y(t) \ Z(t)]^T \in \mathbb{R}^3$, in meters [m];
- the rotational position state variables vector in the inertial reference frame $\boldsymbol{\rho}(t) = [\Phi(t) \ \Theta(t) \ \Psi(t)]^T \in \mathbb{R}^3$, in radians [rad];
- the translational speed state variables vector in the inertial reference frame $\mathbf{c}(t) = [U(t) \ V(t) \ W(t)]^T \in \mathbb{R}^3$, in meters per second [m/s];
- the rotational speed state variables vector in the local reference frame $\boldsymbol{\Omega}(t) = [p(t) \ q(t) \ r(t)]^T \in \mathbb{R}^3$, in radians per second [rad/s].

A sketch of a quadrotor showing these variables for a local reference frame L_o can be seen in Fig. 3.3. The inertial reference frame I is also shown. The index I_o in this case denotes the inertial reference frame, while the index L_o denotes the local reference frame.

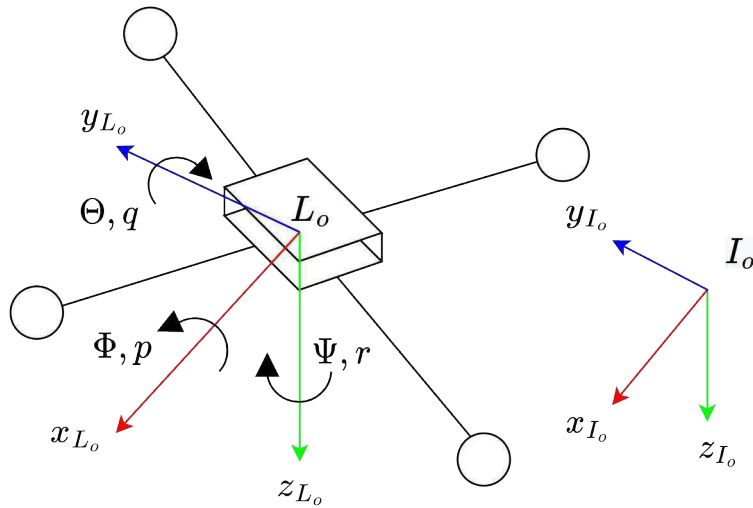


Figure 3.3: Sketch of a quadrotor in "x" configuration with a local and an inertial reference frame.

The difference between the translational position state variables when the local and inertial reference frames are considered must be addressed. This is done through a rotation matrix, from which the inertial position can be obtained from the local variables. The inverse of this same rotation matrix can perform the inverse process, going from the inertial to the local variables.

The rotation matrix $\mathbf{R}_{\mathbf{I}\mathbf{L}} \in \mathbb{R}^{3 \times 3}$ is obtained through rotations around the z , y and x axis, respectively, as shown in (3.1). The expanded expression, with each rotation, can be seen in (3.2), which leads to the final expression in (3.3). The inverse of a rotation matrix is given by its transpose, such that $\mathbf{R}_{\mathbf{I}_o\mathbf{L}_o}^{-1} = \mathbf{R}_{\mathbf{I}_o\mathbf{L}_o}^T = \mathbf{R}_{\mathbf{L}_o\mathbf{I}_o}$.

$$\mathbf{R}_{\mathbf{I}_o\mathbf{L}_o} = \mathbf{R}_z \cdot \mathbf{R}_y \cdot \mathbf{R}_x \quad (3.1)$$

$$\mathbf{R}_{\mathbf{I}_o\mathbf{L}_o} = \begin{bmatrix} \cos \Psi & -\sin \Psi & 0 \\ \sin \Psi & \cos \Psi & 0 \\ 0 & 0 & 1 \end{bmatrix} \cdot \begin{bmatrix} \cos \Theta & 0 & \sin \Theta \\ 0 & 1 & 0 \\ -\sin \Theta & 0 & \cos \Theta \end{bmatrix} \cdot \begin{bmatrix} 1 & 0 & 0 \\ 0 & \cos \Phi & -\sin \Phi \\ 0 & \sin \Phi & \cos \Phi \end{bmatrix} \quad (3.2)$$

$$\mathbf{R}_{\mathbf{I}_o\mathbf{L}_o} = \begin{bmatrix} \cos \Psi \cos \Theta & \cos \Psi \sin \Theta \sin \Phi - \sin \Psi \cos \Phi & \cos \Psi \sin \Theta \cos \Phi + \sin \Psi \sin \Phi \\ \sin \Psi \cos \Theta & \sin \Psi \sin \Theta \sin \Phi + \cos \Psi \cos \Phi & \sin \Psi \sin \Theta \cos \Phi - \cos \Psi \sin \Phi \\ -\sin \Theta & \cos \Theta \sin \Phi & \cos \Theta \cos \Phi \end{bmatrix} \quad (3.3)$$

3.3 Cinematic and dynamic equations

Equations (3.4) through (3.7) describe the movement of a 6-DOF quadrotor. It is considered that the position \mathbf{d} and velocities \mathbf{c} are in the inertial reference frame.

$$\dot{\mathbf{d}} = \mathbf{c} \quad (3.4)$$

$$\dot{\mathbf{c}} = \frac{1}{m} \mathbf{R}_{\mathbf{I}_o\mathbf{L}_o} \begin{bmatrix} 0 \\ 0 \\ -T \end{bmatrix} + \begin{bmatrix} 0 \\ 0 \\ g \end{bmatrix} \quad (3.5)$$

$$\dot{\boldsymbol{\rho}} = \mathbf{S}(\boldsymbol{\rho})\boldsymbol{\Omega} \quad (3.6)$$

$$\dot{\boldsymbol{\Omega}} = \mathbf{J}^{-1}(-\boldsymbol{\Omega} \times \mathbf{J}\boldsymbol{\Omega} + \boldsymbol{\tau}) \quad (3.7)$$

Where, beyond the state variables previously described, the following can be seen:

- The gravity acceleration on earth $g = 9.81 \text{ m/s}$.
- The vehicle mass $m \in \mathbb{R}_{>0}$.
- The total thrust $T \in \mathbb{R}$ along the z_L axis.

- The moments of inertia matrix $\mathbf{J} = \begin{bmatrix} J_x & 0 & 0 \\ 0 & J_y & 0 \\ 0 & 0 & J_z \end{bmatrix} \in \mathbb{R}^{3 \times 3}$.

- The torque vector $\boldsymbol{\tau} = [L \ M \ N]^T \in \mathbb{R}^{3 \times 1}$, where $L \in \mathbb{R}$ is the torque around the x_L axis, $M \in \mathbb{R}$ is the torque around the y_L axis, and $N \in \mathbb{R}$ is the torque around the z_L axis.
- The coupling matrix $\mathbf{S}(\boldsymbol{\rho})$, shown in (3.8), which describes how the movement in one angle affects the others. By analyzing the lines of $\mathbf{S}(\boldsymbol{\rho})$ it can be seen that each term of $\dot{\boldsymbol{\rho}}$ will be a function of the others, which reflects the coupling of the angles in quadrotors. This can be explained by returning to Fig. 3.2, where it is visible that the different movements have conflicting interests in regard to the increase or decrease of the motor speeds.

$$\mathbf{S}(\boldsymbol{\rho}) = \begin{bmatrix} 1 & \sin \Phi \tan \Theta & \cos \Phi \tan \Theta \\ 0 & \cos \Phi & -\sin \Phi \\ 0 & \sin \Phi \sec \Theta & \cos \Phi \sec \Theta \end{bmatrix} \quad (3.8)$$

This model places the torque vector $\boldsymbol{\tau}$ and the total thrust T as the system inputs, from which the translational and angular accelerations can be modified, which allows the control of the translational position \mathbf{d} and rotational position $\boldsymbol{\rho}$. However, in most quadrotor architectures, the control signals are the speed commands for each of the four motors, implying

that a relation must be defined between these two sets of variables. This relation will be shown in Section 3.5.

3.4 Electrical subsystem

The electrical subsystem of a quadrotor mini drone is responsible for vehicle propulsion, flight control, and providing power to all vehicle components. Its components are the motors, the battery, the flight controller, the input/output devices and a device responsible for translating the lower power commands sent from the flight controller into the higher power voltages needed to feed the motors.

This last component merits a more in-depth discussion. In its simplest form, it is comprised of a DC-DC converter. This DC-DC converter receives the duty cycle necessary to provide the appropriate voltage to the motors. In this case, it is assumed that the setup has been properly calibrated, as there is no controller to guarantee that the desired motor speed has been achieved. This setup is typically employed by smaller quadrotors, which have a single integrated board containing all components of the electrical subsystem apart from the motor and the battery. This configuration is the one present in the Parrot Mambo, and is shown in Fig. 3.4. The commanded motor speed $\omega_{i,C}$ is converted to a PWM duty-cycle $\omega_{i,PWM}$, that is sent to a DC-DC converter. This duty-cycle is then employed to modulate the battery voltage v_b so that the appropriate motor voltage v_i is generated.

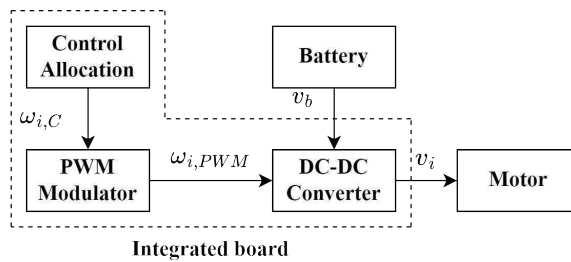


Figure 3.4: Integrated conversion for the commanded motor speeds.

In larger aircraft, a separate component is employed to perform this link between the low and high-power parts of the system. This component is called an Electronic Speed Controller (ESC). This component might be included either if an integrated board is not able to meet the power requirements or if the motor speeds must be directly controlled. The most

common ESC configuration is shown in Fig. 3.5. In this case, a sensorless control solution is employed to generate the PWM duty-cycle $\omega_{i,PWM}$. This approach is adopted to control the motor speed while maintaining a low cost by forgoing the need for a sensor.

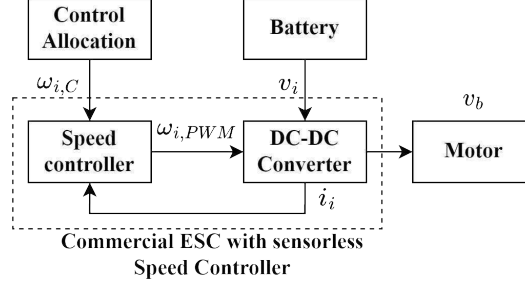


Figure 3.5: Sensorless ESC setup.

A more sophisticated solution will include a closed-loop for the motor speed, as it is shown in Fig. 3.6. While this setup provides the best degree of control over the motor speed, the need for a reliable sensor increases the hardware cost. This is a problem since one of the strong points of quadrotors is their low cost.

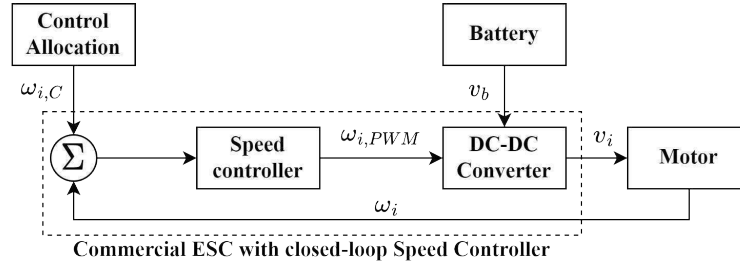


Figure 3.6: Closed-loop ESC setup.

Since the platform employed in this work is the Parrot Mambo, our scenario is the one in Fig. 3.4. A more detailed diagram showing how the electrical subsystem components are connected to one another can be seen in Fig. 3.7.

The propulsion system comprises four coreless DC motors, which achieve a higher rate between motor mass and generated thrust. The coreless motors are modeled considering the energy dissipated in the resistive windings and the energy required to overcome the internal and load friction [Bolton & Pearson 2018]. The armature current is shown in (3.9), where $i_i \in \mathbb{R}$ is the current of motor $i \in \{1, 2, 3, 4\}$, $\omega_i \in \mathbb{R}$ is the propeller rotational rate of motor $i \in \{1, 2, 3, 4\}$, $D_i \in [0, 1]$ is the duty cycle of motor $i \in \{1, 2, 3, 4\}$, $r_a \in \mathbb{R}_{\geq 0}$ is the

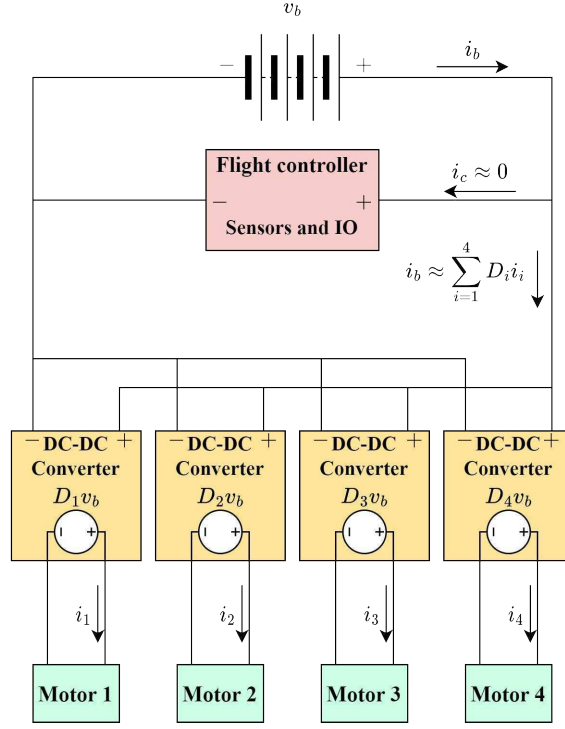


Figure 3.7: A quadrotor mini drone electrical diagram.

armature resistance, $l_a \in \mathbb{R}_{\geq 0}$ is the armature inductance, $v_b \in \mathbb{R}$ is the battery voltage and $k_e \in \mathbb{R}_{\geq 0}$ is the motor torque constant. Due to the small dimensions of the motors employed in this research, it will be considered that the armature inductance is negligible, that is $l_a \approx 0$.

$$i_i = \frac{1}{r_a} \left[D_i v_b - k_e \omega_i - l_a \frac{di_i}{dt} \right] \quad (3.9)$$

The expression of the motor angular velocity dynamics can be seen in (3.10), where $J^P \in \mathbb{R}_{\geq 0}$ is the combined inertia of the rotor and the propeller, $b \in \mathbb{R}_{\geq 0}$ is the viscous friction coefficient, and $k_N \in \mathbb{R}_{\geq 0}$ is the torque or drag coefficient, related to the propeller.

$$J^P \dot{\omega}_i = k_e i_i - b \omega_i - k_N \omega_i^2 \quad (3.10)$$

The battery is responsible for providing power to the flight controller, the actuators, the sensors, and the input/output systems, as can be seen in Fig. 3.7, where the battery current $i_b \in \mathbb{R}$ is shown. The following assumptions were considered in this work: (i) the currents provided to the flight controller, sensors, and input/output systems are negligible when compared to the current provided to the actuators ($i_c \approx 0$) and (ii) the DC-DC converters

are power conserving, such that the power provided by the battery is equal to the electric power consumed by the actuators, as described in (3.11). This assumption was adopted as the details regarding the actual nature of the DC-DC converters used to generate the motor commands for the Parrot Mambo were not available.

$$v_b i_b \approx \sum_{i=1}^4 D_i v_b i_i \Rightarrow i_b \approx \sum_{i=1}^4 D_i i_i \quad (3.11)$$

The sensors are responsible for measuring the system states and providing the feedback signals for the flight controller, along with other relevant data such as the battery voltage. A typical set of quadrotor sensors will normally include an Inertial Measurement Unit (IMU), composed of an accelerometer and a gyroscope, a barometer, and an ultrasound distance sensor aligned with the positive direction of the z axis. In many cases, cameras are also employed to enable position tracking through image-based algorithms, such as Optical Flow. The measurements provided by these sensors are then fused through a state estimator, which provides estimates of the state variables of the 6-DOF model. The input/output interface is used to enable communication with and send commands to the vehicle. It typically employs wireless technologies such as radio, Wi-Fi, or Bluetooth Low Energy (BLE) connection, due to the restrictions imposed by wired alternatives for use during flight. Through the input/output interface flight data logs are collected, and flight trajectories and flight controller algorithms are sent to the vehicle.

3.5 Control allocation and command generation

With the motor equations described in the previous section it is now possible to define the relations that lead from the torque vector $\boldsymbol{\tau}$ and thrust T to, ultimately, the Pulse Width Modulation (PWM) signals corresponding to the commanded angular rates for the motors $\omega_{i,PWM}$. Considering that $\boldsymbol{\omega} = [\omega_1 \ \omega_2 \ \omega_3 \ \omega_4]^T$, the expression for the linear dependency for a quadrotor in "x" configuration is presented in (3.12), where $k_T \in \mathbb{R}$ is the thrust coefficient and k_N is the drag coefficient. The control allocation matrix \mathbf{B} defines a constant configuration, where $l_x = l \sin 45^\circ$, with $l \in \mathbb{R}$ being the geometric distance between the

propellers and the vehicle center of gravity [Falconí & Holzapfel 2014].

$$\begin{bmatrix} L \\ M \\ N \\ T \end{bmatrix} = \underbrace{\begin{bmatrix} -l_x k_T & -l_x k_T & l_x k_T & l_x k_T \\ l_x k_T & -l_x k_T & -l_x k_T & l_x k_T \\ -k_N & k_N & -k_N & k_N \\ k_T & k_T & k_T & k_T \end{bmatrix}}_{\mathbf{B}} \begin{bmatrix} \omega_1^2 \\ \omega_2^2 \\ \omega_3^2 \\ \omega_4^2 \end{bmatrix} \quad (3.12)$$

Therefore, a set of commanded angular rates $[\omega_{1,C} \ \omega_{2,C} \ \omega_{3,C} \ \omega_{4,C}]^T$ can be obtained from the moment and thrust commands $[L_C \ M_C \ N_C \ T_C]^T$ using (3.13).

$$\begin{bmatrix} \omega_{1,C}^2 \\ \omega_{2,C}^2 \\ \omega_{3,C}^2 \\ \omega_{4,C}^2 \end{bmatrix} = \mathbf{B}^{-1} \begin{bmatrix} L_C \\ M_C \\ N_C \\ T_C \end{bmatrix} \quad (3.13)$$

The PWM commands sent to the DC-DC converters $\omega_{i,PWM}$ are then calculated by inverting and solving (3.9) and (3.10). The steady state condition $\dot{\omega}_i = 0$ is considered, which leads to (3.14).

$$0 = k_e i_i - b \omega_i - k_N \omega_i^2 \quad (3.14)$$

Considering the expression for the current i_i shown in (3.9) and replacing ω_i by $\omega_{i,C}$, the expression for D_i as a function of $\omega_{i,C}$ can be obtained as shown in (3.15), resulting in (3.16).

$$0 = \frac{k_e}{r_a} (D_i v_b - k_e \omega_{i,C}) - b \omega_{i,C} - k_N \omega_{i,C}^2$$

$$\frac{k_e}{r_a} (D_i v_b - k_e \omega_{i,C}) = b \omega_{i,C} + k_N \omega_{i,C}^2 \quad (3.15)$$

$$D_i v_b - k_e \omega_{i,C} = \frac{r_a b}{k_e} \omega_{i,C} + \frac{r_a k_N}{k_e} \omega_{i,C}^2$$

$$D_i v_b = k_e \omega_{i,C} + \frac{r_a b}{k_e} \omega_{i,C} + \frac{r_a k_N}{k_e} \omega_{i,C}^2$$

$$D_i = \frac{1}{k_e v_b} [(k_e^2 + r_a b) \omega_{i,C} + r_a k_N \omega_{i,C}^2] \quad (3.16)$$

Notice that the value of the battery voltage v_b must be known in (3.16). If this value is neither measured nor estimated, the assumed nominal battery voltage $v_{b,0}$ is used, as shown in (3.17).

$$D_i = \frac{1}{k_e v_{b,0}} [(k_e^2 + r_a b) \omega_{i,C} + r_a k_N \omega_{i,C}^2] \quad (3.17)$$

The expressions defined in Sections 3.3, 3.4, and 3.5 detail how the components of a quadrotor work, except for the battery which is the subject of the subsequent chapter. However, to analyze the closed-loop dynamics of a quadrotor, it is necessary to define the control strategies implemented in the flight controller shown in Fig. 3.7. This will be explored in the following sections, which show how the Nonlinear Dynamic Inversion approach was applied to solve the altitude and attitude control problems.

3.6 Nonlinear dynamic inversion and error controller

The Nonlinear Dynamic Inversion (NDI) technique became popular for flight controllers around 1990, due to its ability to decouple the controller design from the variations in the vehicle dynamics during a large flight envelope (the limits within the gravity center of a flying vehicle that can be safe for operation). The basis of this method is feedback linearization [Horn et al. 2019]. The concept is that by canceling the nonlinear system dynamics, a linear controller can be employed. However, the relevant system parameters and states must be known, otherwise, the resulting output will not be satisfactory [Karlsson 2002]. This strategy had its stability and robustness previously studied in [Yuan et al. 2013] and [Ducard & Geering 2008], and was applied to UAVs in [Tal & Karaman 2021] and [Zhanqi & Xi'an 2012]

The feedback linearization process transforms a nonlinear system into a linear equivalent through a change of variables and the use of proper control input. It can be applied to nonlinear systems of the form shown in (3.18) and (3.19), where $x \in \mathbb{R}^n$ is the state vector, $u \in \mathbb{R}^v$ is the input signals vector and $y \in \mathbb{R}^m$ is the output signals vector.

$$\dot{x} = f(x) + g(x)u \quad (3.18)$$

$$y = h(x) \quad (3.19)$$

The goal is to achieve a control input of the form (3.20) such that the mapping between u and the new input ν is linear. Then, a control strategy can be employed in an outer loop in the resulting linear system.

$$u = a(x) + b(x)\nu \quad (3.20)$$

For simplicity, it is assumed that the system shown in (3.18) and (3.19) is Single Input Single Output (SISO). The following analysis will show how to achieve the nonlinear dynamic inversion and can be easily extended for a system with multiple inputs and outputs. It is divided into four parts: a brief explanation of the Lie derivative, the formalization of the relative degree, the feedback linearization process itself, and its application to the case of quadrotor altitude and attitude control loops.

3.6.1 Lie derivative

Consider the temporal derivative of (3.19), which can be obtained through the chain rule, resulting in (3.22).

$$\dot{y} = \frac{dh(x)}{dt} = \frac{dh(x)}{dx} \dot{x} \quad (3.21)$$

$$\dot{y} = \frac{dh(x)}{dx} f(x) + \frac{dh(x)}{dx} g(x)u \quad (3.22)$$

Then, the Lie derivative of $h(x)$ with respect to $f(x)$ can be defined as in (3.23).

$$L_f h(x) = \frac{dh(x)}{dx} f(x) \quad (3.23)$$

Similarly, the Lie derivative of $h(x)$ with respect to $g(x)$ is shown in (3.24).

$$L_g h(x) = \frac{dh(x)}{dx} g(x) \quad (3.24)$$

This notation allows expressing \dot{y} as shown in (3.25):

$$\dot{y} = L_f h(x) + L_g h(x)u \quad (3.25)$$

The Lie derivative notation is also convenient when taking several derivatives with respect to the same vectorial field or with respect to a different one. Consider, for example, (3.26) and (3.27).

$$L_f^2 h(x) = L_f L_f h(x) = \frac{d(L_f h(x))}{dx} f(x) \quad (3.26)$$

$$L_g L_f h(x) = \frac{d(L_f h(x))}{dx} g(x) \quad (3.27)$$

3.6.2 Relative degree

The system defined by (3.18) and (3.19) has a relative degree $r \in \mathbb{N}$ in a region $x_0 \subset X_0$ if the conditions defined in (3.28) and (3.29) are met for $x \in x_0$ with $0 \leq k \leq r - 2, k \in \mathbb{N}$.

$$L_g L_f^k h(x) = 0 \quad (3.28)$$

$$L_g L_f^{(r-1)} h(x_0) \neq 0 \quad (3.29)$$

Considering this definition in relation to the expression of the temporal derivative y , it can be defined that the relative degree of a system is the number of times the derivative y must be derived until the output u appears explicitly in the derivative expression.

3.6.3 Feedback linearization

Assuming that the relative degree of the system defined by (3.18) and (3.19) is n , after n derivatives of the output signal y the result shown in (3.30) is obtained. The notation $y^{(n)}$ indicates the n th derivative of y .

$$\begin{aligned}
y &= h(x) \\
\dot{y} &= L_f h(x) \\
\ddot{y} &= L_f^2 h(x) \\
&\vdots \\
y^{(n-1)} &= L_f^{(n-1)} h(x) \\
y^{(n)} &= L_f^n h(x) + L_g L_f^{(n-1)} h(x) u
\end{aligned} \tag{3.30}$$

As the relative degree of the system is assumed to be n , the Lie derivatives of the form $L_g L_f^i h(x)$, for $i = 1, \dots, (n-2)$, are equal to zero. That is, the input signal u has no direct contribution for the first $(n-1)$ derivatives. $T_{\text{NDI}}(x)$ gives the normalized form of the system from these first $(n-1)$ derivatives, arriving at (3.31).

$$z = T_{\text{NDI}}(x) = \begin{bmatrix} z_1(x) \\ z_2(x) \\ \vdots \\ z_n(x) \end{bmatrix} = \begin{bmatrix} y \\ \dot{y} \\ \vdots \\ y^{(n-1)} \end{bmatrix} = \begin{bmatrix} h(x) \\ L_f h(x) \\ \vdots \\ L_f^{(n-1)} h(x) \end{bmatrix} \tag{3.31}$$

The transform shown in (3.31) translates trajectories of the original coordinate system x to a new coordinate system z . These new trajectories are described by the new system shown in (3.32).

$$\begin{cases} \dot{z}_1 = L_f h(x) = z_2(x) \\ \dot{z}_2 = L_f^2 h(x) = z_3(x) \\ \vdots \\ \dot{z}_n = L_f^n h(x) + L_g L_f^{(n-1)} h(x) u \end{cases} \tag{3.32}$$

By observing the last equation of the system (3.32), it is possible to see that if the feedback control law is chosen as defined in (3.33), then $\dot{z}_n = \nu$.

$$u = \frac{1}{L_g L_f^{(n-1)} h(x)} (-L_f^n h(x) + \nu) \tag{3.33}$$

The control law presented in (3.33) provides a linear input-output map from ν to $z_1 = y$.

$$\begin{cases} \dot{z}_1 = z_2 \\ \dot{z}_2 = z_3 \\ \vdots \\ \dot{z}_n = \nu \end{cases} \quad (3.34)$$

The resulting system (3.34) is a cascade of n integrators, and an outer control loop ν can be chosen by employing standard control solutions for linear systems. The resulting NDI architecture can be seen in Fig. 3.8.

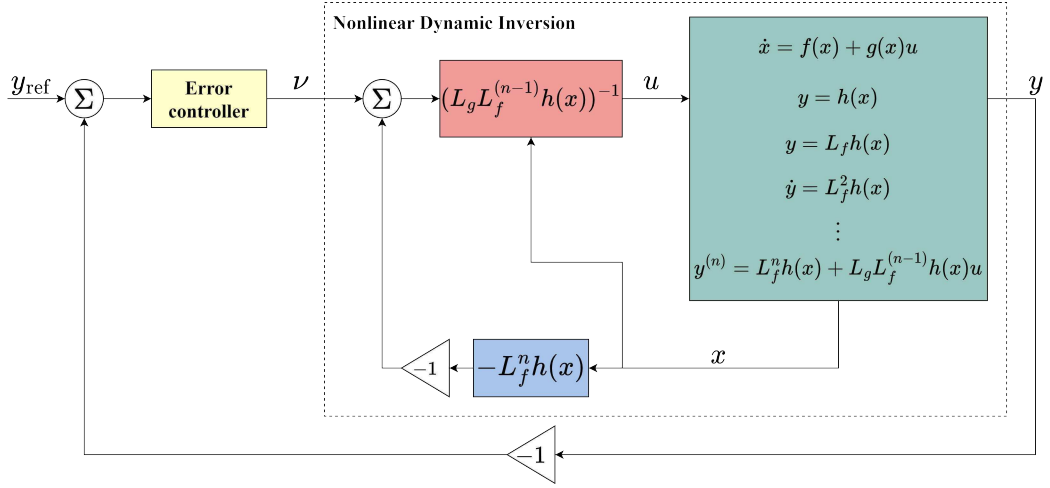


Figure 3.8: Nonlinear dynamic inversion control block diagram.

The algorithm described above shows how to apply the NDI to a generic system of the form defined in (3.18) and (3.19). In the next sections, it will be shown how to apply this strategy to the altitude and attitude control loops.

3.6.4 Applying NDI to a quadrotor

Attitude control loop

The attitude dynamics of a quadrotor were defined in (3.6), where the coupling of the angular speeds is shown. The rotational dynamics are given by the Euler equation, which

was shown in (3.7). These expressions are repeated below in (3.35) and (3.36), for ease of reading.

$$\dot{\rho} = \mathbf{S}(\rho)\Omega \quad (3.35)$$

$$\dot{\Omega} = \mathbf{J}^{-1}(-\Omega \times \mathbf{J}\Omega + \tau) \quad (3.36)$$

The system can be rewritten as presented in (3.37), (3.38) and (3.39).

$$\mathbf{y} = \mathbf{x}_1 \quad (3.37)$$

$$\dot{\mathbf{x}}_1 = \mathbf{G}_1(\mathbf{x}_1) \mathbf{x}_2 \quad (3.38)$$

$$\dot{\mathbf{x}}_2 = \mathbf{f}_2(\mathbf{x}_2) + \mathbf{G}_2\mathbf{u} \quad (3.39)$$

Where

- \mathbf{y} is the system output and $\mathbf{y} = \mathbf{x}_1 = \rho$
- $\mathbf{x}_2 = \Omega$
- $\mathbf{u} = \tau$
- $\mathbf{f}_2 = -\mathbf{J}^{-1}[\mathbf{x}_2 \times (\mathbf{J}\mathbf{x}_2)]$
- $\mathbf{G}_2 = \mathbf{J}^{-1}$
- $\mathbf{G}_1(\mathbf{x}_1) = \mathbf{S}(\rho)$

By taking the derivative of the output \mathbf{y} in (3.37), (3.40) can be written.

$$\dot{\mathbf{y}} = \dot{\mathbf{x}}_1 = \mathbf{G}_1(\mathbf{x}_1) \mathbf{x}_2 = \mathbf{S}(\rho)\Omega \quad (3.40)$$

The goal is to obtain the expression for the attitude dynamics $\ddot{\mathbf{y}}$. This results in (3.41) by taking the derivative of (3.40).

$$\ddot{\mathbf{y}} = (L_{\mathbf{G}_1(\mathbf{x}_1)} \mathbf{G}_1(\mathbf{x}_1) \mathbf{x}_2) \mathbf{G}_1(\mathbf{x}_1) \mathbf{x}_2 + \mathbf{G}_1(\mathbf{x}_1) \dot{\mathbf{x}}_2 \quad (3.41)$$

Equation (3.42) can be written by applying the Lie derivative.

$$(L_{\mathbf{G}_1(x_1)} \mathbf{G}_1(\mathbf{x}_1) \mathbf{x}_2) = \left. \frac{\partial(\mathbf{G}_1(\mathbf{x}_1) \mathbf{x}_2)}{\partial \mathbf{x}_1^T} \mathbf{G}_1(\mathbf{x}_1) \right|_{\mathbf{x}_1} \quad (3.42)$$

Then, (3.44) results from applying (3.42) to (3.41).

$$\ddot{\mathbf{y}} = \frac{\partial(\mathbf{G}_1(\mathbf{x}_1) \mathbf{x}_2)}{\partial \mathbf{x}_1^T} \mathbf{G}_1(\mathbf{x}_1) \mathbf{x}_2 + \mathbf{G}_1(\mathbf{x}_1) \dot{\mathbf{x}}_2 \quad (3.43)$$

$$\ddot{\mathbf{y}} = (L_{\mathbf{G}_1(x_1)} \mathbf{G}_1(\mathbf{x}_1) \mathbf{x}_2) \mathbf{x}_2 + \mathbf{G}_1(\mathbf{x}_1)(\mathbf{f}_2(\mathbf{x}_2) + \mathbf{G}_2 \cdot \mathbf{u}) \quad (3.44)$$

Considering $\nu \in \mathbb{R}^3$ the pseudo-control signal, then, the control goal is to track $\ddot{\mathbf{y}} = \nu$. This leads to (3.45), from which the commanded control input u_c can be written as (3.48) such that the nonlinear dynamics are inverted.

$$(L_{\mathbf{G}_1(x_1)} \mathbf{G}_1(\mathbf{x}_1) \mathbf{x}_2) \mathbf{x}_2 + \mathbf{G}_1(\mathbf{x}_1)(\mathbf{f}_2(\mathbf{x}_2) + \mathbf{G}_2 \mathbf{u}) = \nu \quad (3.45)$$

$$\mathbf{f}_2(\mathbf{x}_2) + \mathbf{G}_2 \mathbf{u} = \mathbf{G}_1^{-1}(\mathbf{x}_1)(\nu - (L_{\mathbf{G}_1(x_1)} \mathbf{G}_1(\mathbf{x}_1) \mathbf{x}_2) \mathbf{x}_2) \quad (3.46)$$

$$\mathbf{G}_2 \mathbf{u} = \mathbf{G}_1^{-1}(\mathbf{x}_1) \nu - \mathbf{G}_1^{-1}(\mathbf{x}_1)(L_{\mathbf{G}_1(x_1)} \mathbf{G}_1(\mathbf{x}_1) \mathbf{x}_2) \mathbf{x}_2 - \mathbf{f}_2(\mathbf{x}_2) \quad (3.47)$$

$$\mathbf{u}_c = \mathbf{G}_2^{-1}[\mathbf{G}_1^{-1}(\mathbf{x}_1) \nu - \mathbf{G}_1^{-1}(\mathbf{x}_1)(L_{\mathbf{G}_1(x_1)} \mathbf{G}_1(\mathbf{x}_1) \mathbf{x}_2) \mathbf{x}_2 - \mathbf{f}_2(\mathbf{x}_2)] \quad (3.48)$$

Returning to the original notation, the expression for the commanded torques τ_C is given by (3.49) where $\nu_\rho \in \mathbb{R}^3$ is the vector of the attitude pseudo-control signals and $\dot{\mathbf{S}}(\boldsymbol{\rho}, \dot{\boldsymbol{\rho}})$ is the derivative of the coupling matrix $\mathbf{S}(\boldsymbol{\rho})$ with respect to $\boldsymbol{\rho}$.

$$\tau_C = \mathbf{J}[\mathbf{S}^{-1}(\boldsymbol{\rho}) \nu_\rho - \mathbf{S}^{-1}(\boldsymbol{\rho}) \dot{\mathbf{S}}(\boldsymbol{\rho}, \dot{\boldsymbol{\rho}}) \boldsymbol{\Omega} + \mathbf{J}^{-1}(-\boldsymbol{\Omega} \times \mathbf{J} \boldsymbol{\Omega})] \quad (3.49)$$

Altitude control loop

The application of the NDI to the altitude control loop is analogous to that seen above for the attitude control loop. The translational position dynamics were defined in (3.4) and

(3.5), from which the altitude dynamics can be extracted, as shown in (3.50) and (3.51).

$$\dot{Z} = W \quad (3.50)$$

$$\dot{W} = g - \frac{T}{m} \cos \Phi \cos \Theta \quad (3.51)$$

The system shown in (3.50) and (3.51) can be rewritten as (3.52) (3.53), and (3.54).

$$y = x_1 \quad (3.52)$$

$$\dot{x}_1 = x_2 \quad (3.53)$$

$$\dot{x}_2 = g - G_2(z_1)u \quad (3.54)$$

Where

- y is the system output and $y = x_1 = Z$
- $x_2 = W$
- $u = T$
- $z_1 = \rho$
- $G_2(z_1) = -\frac{\cos \Phi \cos \Theta}{m}$

Then, the equation for \ddot{y} is shown in (3.55).

$$\ddot{y} = g - G_2(z_1)u \quad (3.55)$$

Once again, $\nu \in \mathbb{R}$ is the pseudo-control signal, and the control goal is to track $\ddot{y} = \nu$. This leads to equation (3.56). From (3.56), the commanded control input u_c is defined as (3.57).

$$\nu = g - G_2(z_1)u \quad (3.56)$$

$$u_c = G_2^{-1}(z_1)(g - \nu) \quad (3.57)$$

Returning to the original notation, the expression for the commanded thrust T_C is given by (3.58), where ν_Z is the altitude pseudo-control signal.

$$T_C = \frac{m}{\cos \Phi \cos \Theta} (g - \nu_Z) \quad (3.58)$$

Reference model and error controller

Let the desired system behavior for the system be given by $y_{\text{ref}} \in \mathbb{R}$. To provide a smoother and easier-to-track reference signal, a reference model of the form (3.59) is employed. The same model is also presented in a block diagram in Fig. 3.9. The constants $\omega_0 \in \mathbb{R}$ and $\zeta_0 \in \mathbb{R}$ are the natural frequency and the damping coefficient, respectively. Their values must be chosen to take into account the physical limitations of the vehicle and the desired dynamic behavior.

$$\ddot{y}_{\text{ref}} + 2\zeta_0\omega_0\dot{y}_{\text{ref}} + \omega_0^2(y_C - y_{\text{ref}}) = 0 \quad (3.59)$$

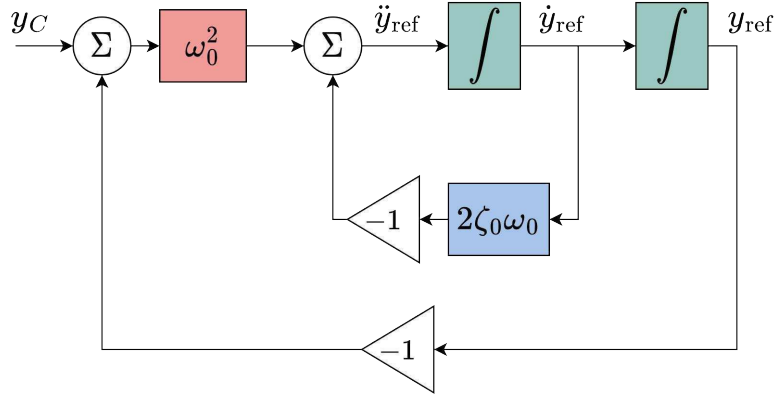


Figure 3.9: Block diagram of a second order reference model.

The pseudo control ν is defined as (3.60), where K_e , K_{e_I} and K_{e_d} are the proportional, integral and derivative gains, respectively.

$$\nu = \ddot{y}_{\text{ref}} + K_{e_I} \int_0^t \mathbf{e} \, d\delta + K_e \mathbf{e} + K_{e_d} \dot{\mathbf{e}} \quad (3.60)$$

$$\therefore \mathbf{e}_I = \int_0^t \mathbf{e} d\delta \quad (3.61)$$

With the error signal defined as in (3.62), the first and second derivatives are given by (3.63) and (3.64).

$$\mathbf{e} = \mathbf{y}_{\text{ref}} - \mathbf{y} \quad (3.62)$$

$$\dot{\mathbf{e}} = \dot{\mathbf{y}}_{\text{ref}} - \dot{\mathbf{y}} \quad (3.63)$$

$$\ddot{\mathbf{e}} = \ddot{\mathbf{y}}_{\text{ref}} - \ddot{\mathbf{y}} \quad (3.64)$$

Considering that after the feedback linearization $\ddot{y} = \nu$, (3.65) can be written. The resulting error dynamics are then given by (3.66), which shows that through the proper choice of the proportional gain \mathbf{K}_e , integral gain \mathbf{K}_{e_I} and derivative gain $\mathbf{K}_{\dot{e}}$ the closed loop poles can be placed in an arbitrary location.

$$\ddot{\mathbf{e}} = \ddot{\mathbf{y}}_{\text{ref}} - \ddot{\mathbf{y}}_{\text{ref}} - \mathbf{K}_{e_I} \int_0^t \mathbf{e} d\delta - \mathbf{K}_e \mathbf{e} - \mathbf{K}_{\dot{e}} \dot{\mathbf{e}} \quad (3.65)$$

$$\begin{bmatrix} \dot{\mathbf{e}}_I \\ \dot{\mathbf{e}} \\ \ddot{\mathbf{e}} \end{bmatrix} = \begin{bmatrix} 0 & 1 & 0 \\ 0 & 0 & 1 \\ -\mathbf{K}_{e_I} & -\mathbf{K}_e & -\mathbf{K}_{\dot{e}} \end{bmatrix} \begin{bmatrix} \mathbf{e}_I \\ \mathbf{e} \\ \dot{\mathbf{e}} \end{bmatrix} \quad (3.66)$$

Block diagrams

When applied to a quadrotor, the control strategy described in this Section results in the block diagrams for the altitude and attitude control loops shown in Figs. 3.10 and 3.11, respectively. It should be noted that a control loop for the X and Y variables are also present, but acting as a way to relate position commands to attitude commands, which is consistent with the dynamic equations for the quadrotor presented in Section 3.3, which show that the variables directly related to the inputs T , L , M and N are the altitude and attitude variables.

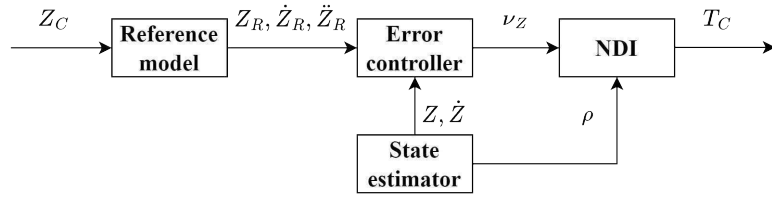


Figure 3.10: Block diagram of the altitude control system.

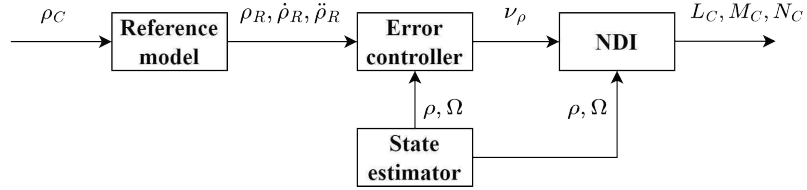


Figure 3.11: Block diagram of the attitude control system.

3.7 Integrated model

The integrated system of a quadrotor mini drone, with all of the components described in the previous sections, is shown in Fig. 3.12. A state estimator receives the data from the embedded sensors and estimates them to the controllers. The commands for the attitude control system are derived from the position controller, which defines the desired position in relation to the inertial reference frame. The altitude is controlled in a separate loop, as one of the desirable characteristics of quadrotors is their ability to keep a constant height while changing their position. The resulting commanded torques T_C , L_C , M_C , and N_C are then used as the input for the control allocation process and the PWM commands for the motors are generated and sent to the ESCs. The ESCs then feed the battery voltage to feed the motors such that they spin at the desired speed, and from there the dynamic equations of the 6-DOF model can describe the resulting flight dynamics.

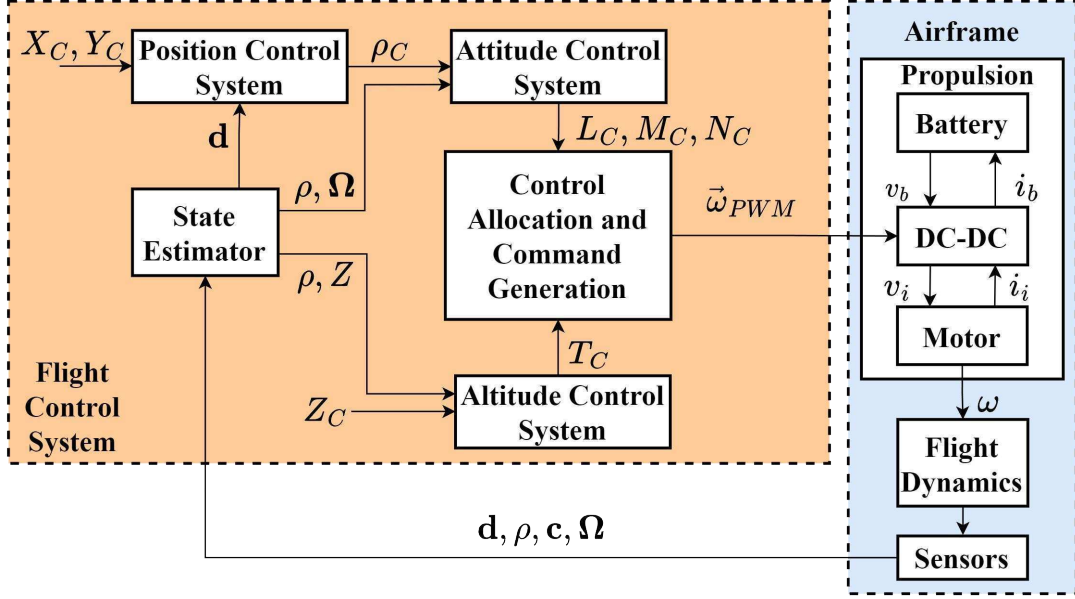


Figure 3.12: Integrated system of a quadrotor mini drone.

In Fig. 3.12 the position controller is shown. As mentioned before, this controller will provide the commands for the attitude controller according to the desired trajectory for the vehicle. The corresponding equations are presented in (3.67) and (3.68), where $e_X = X - X_R$, $e_Y = Y - Y_R$, Φ_C and Θ_C are the commanded pitch and roll angles, respectively, and K_{pY} , K_{dY} , K_{pX} and K_{dX} are the position controller gains. A rotation is performed to calculate the error, as the local and inertial reference frames might not be aligned.

$$\Phi_C = K_{pY} (-\sin(\Psi)e_X + \cos(\Psi)e_Y) + K_{dY}V \quad (3.67)$$

$$\Theta_C = K_{pX} (\cos(\Psi)e_X + \sin(\Psi)e_Y) + K_{dY}U \quad (3.68)$$

Additionally, the control of the yaw angle Ψ also needs to be detailed. When considering a quadrotor flight, controlling the yaw angle corresponds only to defining which direction the vehicle will be facing. This fact, in addition to the fact the yaw angle bears no influence over the movement along the horizontal plane or the vertical axis, makes it so controlling this state is comparatively less critical than controlling the other attitude states and the altitude. A separate PID controller is used in this case, according to the expression shown in (3.69),

where $e_\Psi = \Psi_R - \Psi$, resulting in the commanded moment L_C .

$$L_C = K_{p\Psi}e_\Psi + K_{i\Psi} \int_0^t e_\Psi d\delta + K_{d\Psi}\dot{e}_\Psi \quad (3.69)$$

In this chapter, the quadrotor mini drone model used in this research was detailed. This includes the explanation of the basic concepts which govern the operation of such vehicles, along with the relevant kinematic and dynamic equations. The electrical subsystem was described, with the exception of the battery, along with how the commands for the motors are generated. The application of the NDI control strategy to the quadrotor altitude and attitude control loops was shown. The connections between these different components led to an integrated model. In the next chapter, the battery model will be presented, including its mathematical expressions and experimental results.

Chapter 4

Model of a lithium-polymer battery

In this chapter, the theoretical concepts, modeling strategies, and research results regarding the study of Lithium-Polymer(LiPo) batteries as a component in quadrotor systems are explored. The concepts behind the workings of Lithium based batteries are explained. The proposal is to model LiPo batteries by combining two models: the Rakhmatov-Vrudhula diffusion model and an electrical model, which are described. Subsequently, a discrete version of the composition of these two models is presented. The parameters of this discrete model were estimated from experimental data. A study was conducted on how to best estimate the necessary diffusion and electrical model parameters, leading to a set of tests that allows the values to be estimated jointly. Then, the results of the modeling process of several batteries are shown, along with a description of the experiment design and of the decisions taken during the modeling process. The results demonstrate that the employed modeling approach was able to accurately capture the dynamics of LiPo batteries.

4.1 Workings of lithium-based batteries

A battery, or electrochemical accumulator, is defined as a device capable of converting chemical energy into electrical energy [Silva 2016]. The typical structure of a battery is an association in series or parallel of one or more electrochemical cells, where each of these cells possesses a positive electrode, or cathode, and a negative electrode, or anode, which are separated by an electrolyte. Chemical energy is converted to electrical energy as a result of the chemical reactions between the electrodes and the ions in the electrolyte, also called

electroactive species [Neves et al. 2016].

During the discharge process inside lithium-based battery cells, a process of diffusion of the lithium ions happens from the anode to the cathode, which can be seen in Fig. 4.1. This phenomenon is modeled in the first model proposed for LiPo batteries in [Doyle, Fuller & Newman 1993]. During the recharge, the diffusion happens in the opposite direction, that is, it is bidirectional, changing according to the operating regime.

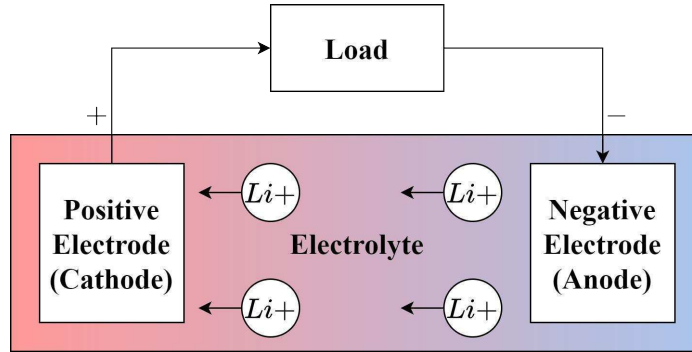


Figure 4.1: Representation of the lithium ions diffusion during the battery discharge.

The loss of electrons is called oxidation, and the gain is called reduction. Thus, the reactions in the discharge process can be described by (4.1) for the reduction and (4.2) for the oxidation, where e^- are the electrons, O are the oxidized species and R the reduced species. In the reduction, the oxidized species receive electrons and become reduced species, while in the oxidation the reduced species free electrons to form oxidized species. If there is no load, and consequently no ion diffusion, the electroactive species remain uniformly distributed along the electrolyte.



The most relevant variables when formulating the specifications for a given battery are its voltage, measured in volts (V), its capacity, typically measured in milliampere-hour (mAh) and its maximum constant discharge rate in amperes (A), measured as a multiple of the current specified in the capacity. In LiPo batteries, the nominal voltage value is around 3.6 to 3.7 V per cell. Such values are smaller than the full charge voltage equal to 4.2 V and

greater than the full discharge voltage equal to 3.0 V . Since batteries are manufactured by associating cells, either in series or parallel, the nominal voltage of a LiPo battery is always an integer multiple of this value.

In a real battery, both the terminal voltage and the capacity diminish as the current demanded by the load increases [Jongerden & Haverkort 2010]. Another phenomenon that happens in real batteries is the formation of a gradient of the concentration of electroactive species in the electrolyte during the discharge. This concentration of active material appears in the junction between the electrode and the electrolyte, getting smaller as the electrochemical reactions happen. When the battery is not being discharged the intensity of the gradient is reduced. The concentration of electroactive species in the electrolyte becomes more uniform, and the battery's apparent charge increases, in a process called the regeneration effect.

This process is shown in Fig. 4.2. At first, the battery is fully charged (a). As the discharge occurs, a gradient of electroactive species appears in the electrolyte (b), and when the discharge ends the remaining electroactive species return to a uniform distribution (c), which is precisely the regeneration effect described previously, which replenishes part of the available charge in the battery. As multiple discharges happen, the concentration of the electroactive species diminishes (d), until it is no longer possible to maintain the necessary chemical reactions for energy generation, and the battery is then considered discharged.

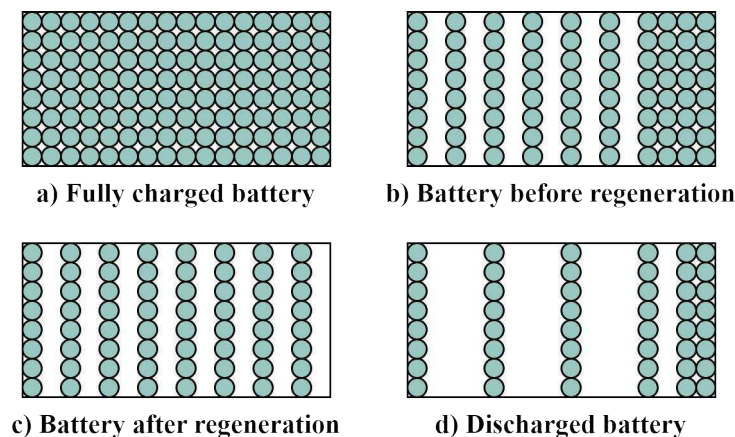


Figure 4.2: Representation of the different states of the battery regeneration process.

Another behavior present in real batteries is the capacity rate effect, which is associated with the regeneration effect. As the discharge current increases, the effective capacity of the battery decreases, since the electroactive species are being consumed by the chemical

reactions at the electrode faster than they can be replenished through the diffusion process. When it comes to small discharge currents, the opposite occurs, where it is possible to use almost the totality of the electroactive species in the battery. In this case, the concentration at the electrode will take more time to reach the critical point at which the battery is discharged since the diffusion will have more time to happen. For intermediate values of discharge currents a mix of both regimes is observed [Fransozi 2015][Schneirderi 2011].

The following voltage values are, generally, important when analyzing batteries:

- Open-circuit voltage v_{oc} : the value of the voltage in the battery terminals in the absence of load.
- Terminal voltage v_b : the value of the voltage between the battery terminals in the presence of load.
- Cut-off voltage v_{cut} : Voltage value between the battery terminals at which the battery is considered discharged. Further discharge below this level might permanently damage the battery.

A model is necessary to describe how the electrochemical diffusion process inside the battery will affect the available terminal voltage and its charge. The Rakhmatov-Vrudhula model achieves this by using Fick's laws of diffusion. This demonstration is shown in the next section, according to what was presented in [Neves et al. 2016].

4.2 Rakhmatov-Vrudhula model

The Rakhmatov-Vrudhula diffusion model has been used to model the diffusion dynamics of Li-ion batteries in works such as [Wang et al. 2022], [Neves et al. 2016] and [Spohn et al. 2008], and provides an accurate solution to the state of charge estimation problem coupled with a very low computational cost. The resulting model is a solution for the set of differential equations that describe the diffusion process inside the battery. The model parameters are dependent solely on the knowledge of the total battery capacity and the diffusion coefficient.

The decision to use the Rakhmatov-Vrudhula model for LiPo batteries was made after comparing it to the LiPo battery model proposed in [Doyle, Fuller & Newman 1993].

Although there are differences in the materials used in constructing Li-ion and LiPo batteries, the diffusion phenomenon is described by Fick's laws in both cases, which suggests that the diffusion operates similarly for both batteries. While this does not prove that the Rakhmatov-Vrudhula model is an exact diffusion model for LiPo batteries, it indicates that it may be possible to use it for this type of battery. The results in Section 4.5 demonstrate that the proposed model was able to accurately model the behavior of several LiPo batteries.

For a given electrochemical cell, consider that there is a uniform distribution of the electroactive species through an electrolyte of finite dimension μ . Consider, then, that $C(x, t)$ gives the concentration of electroactive species in the electrolyte at a distance $x \in [0, \mu]$ from the electrode in a time instant $t \in [0, L_b]$, where L_b is the discharge time of the battery. At $x = 0$ the function $C(0, t)$ gives the concentration of the electroactive species at the electrode. When the battery is fully charged, the initial concentration at the electrolyte is given by a value C^* . By comparing the value of $C(0, t)$ with C^* it is possible to measure how many electroactive species left the electrode since the beginning of a given discharge. This comparison is called depth of charge $\rho(t)$, as can be seen in (4.3).

$$\rho(t) = 1 - \frac{C(0, t)}{C^*} \quad (4.3)$$

Since the total discharge time is given by L_b , $C(0, L_B)$ is the condition of the concentration of charge at the electrode which corresponds to the value of the cut-off voltage v_{cut} . As such, $\rho(L_b)$ is the total depth of discharge.

From Fick's first law [Bard & Faulkner 2001] it can be seen that the flux of electroactive species $J(x, t)$ is proportional to the gradient of the concentration, as can be seen in (4.4), where D is a constant associated to the diffusion coefficient of the electroactive species.

$$-J(x, t) = D \frac{\partial C(x, t)}{\partial x} \quad (4.4)$$

The variation in the concentration of the electroactive species through time is given by Fick's second law (4.5).

$$\frac{\partial C(x, t)}{\partial x} = D \frac{\partial^2 C(x, t)}{\partial x^2} \quad (4.5)$$

From Faraday's law it can be established that for $x = 0$ the flux $J(0, t)$ at the surface of the electrode is proportional to the battery current $i_b(t)$, as can be seen in (4.6), where n is the number of electrons taking part in the electrochemical reaction, F is Faraday's constant and S is the surface area of the electrode.

$$-J(0, t)nSF = i_b(t) \quad (4.6)$$

It is possible to employ the laws above to obtain the relationship (4.7).

$$D \frac{\partial C(x, t)}{\partial x} \Big|_{x=0} = \frac{i_b(t)}{nFS} \quad (4.7)$$

When $x = \mu$, that is, when at the furthest point from the electrode in the diffusion region, the boundary conditions establish that the flux is zero, which gives (4.8).

$$D \frac{\partial C(x, t)}{\partial x} \Big|_{x=\mu} = 0 \quad (4.8)$$

The system of differential equations formed by (4.4) and (4.5), along with the boundary conditions (4.7) and (4.8) was solved by Rakhmatov and Vrudhula [Rakhmatov & Vrudhula 2003]. A solution of the form (4.9) was proposed.

$$\frac{d^2 C(x)}{dx^2} - a^2 C(x) = -b \quad (4.9)$$

Equation (4.10) can be obtained through the Laplace transform $\bar{C}(s)$.

$$\begin{aligned} s^2 \bar{C}(s) - sC(0) - C'(0) - a^2 \bar{C}(s) &= -\frac{b}{s} \\ \bar{C}(s) &= \frac{-b + s^2 C(0) + sC'(0)}{s(s-a)(s+a)} \end{aligned} \quad (4.10)$$

Expression (4.11) is obtained from (4.10) through partial fraction expansion.

$$\bar{C}(s) = \frac{A'}{s+a} + \frac{B'}{s-a} + \frac{b}{a^2 s} \quad (4.11)$$

The result of the inverse Laplace transform of (4.11) is shown in (4.12).

$$C(x) = \frac{b}{a^2} + A'e^{-ax} + B'e^{ax} \quad (4.12)$$

Next, the Laplace transform is applied to Fick's second law (4.5), obtaining (4.13), where $\bar{C}(x, s)$ is a boundary condition and $C^* = C(x, 0)$.

$$s\bar{C}(x, s) - \bar{C}(x, 0) = D \frac{d^2 \bar{C}(x, s)}{dx^2} \quad (4.13)$$

By comparing (4.13) with (4.9) it is possible to determine the values of a^2 e b .

$$a^2 = \frac{s}{D} \quad (4.14)$$

$$b = \frac{C^*}{D} \quad (4.15)$$

Replacing a^2 and b in (4.12), equation (4.16) is obtained.

$$\bar{C}(x, s) = \frac{C^*}{s} + A'(s)e^{-\sqrt{\frac{s}{D}}x} + B'(s)e^{\sqrt{\frac{s}{D}}x} \quad (4.16)$$

The boundary conditions in (4.17) result from the derivative of (4.16).

$$\frac{d\bar{C}(x, s)}{dx} = -\sqrt{\frac{s}{D}} \left(A'(s)e^{-\sqrt{\frac{s}{D}}x} - B'(s)e^{\sqrt{\frac{s}{D}}x} \right) \quad (4.17)$$

The system of equations to find the values of $A'(s)$ and $B'(s)$ is formed from (4.6) and (4.7), arriving at (4.18) and (4.19).

$$-\sqrt{\frac{s}{D}}(A'(s) - B'(s)) = \frac{\bar{i}(s)}{nFSD} \quad (4.18)$$

$$-\sqrt{\frac{s}{D}} \left(A'(s)e^{-\sqrt{\frac{s}{D}}\omega} - B'(s)e^{\sqrt{\frac{s}{D}}\omega} \right) = 0 \quad (4.19)$$

by isolating $B'(s)$ in (4.18), the expression in (4.20) is obtained.

$$B'(s) = A'(s) + \frac{\bar{i}(s)\sqrt{D}}{nFSD\sqrt{s}} \quad (4.20)$$

replacing (4.20) in (4.19), (4.21) can be written.

$$A'(s) = \frac{\frac{-\bar{i}(s)\sqrt{D}}{nFSD\sqrt{s}}e^{\omega\sqrt{\frac{s}{D}}}}{e^{\omega\sqrt{\frac{s}{D}}} - e^{-\omega\sqrt{\frac{s}{D}}}} \quad (4.21)$$

applying (4.21) in (4.20) the expression (4.22) for $B'(s)$ is obtained.

$$B'(s) = \frac{\bar{i}(s)\sqrt{D}}{nFSD\sqrt{s}} \left(1 - \frac{e^{\omega\sqrt{\frac{s}{D}}}}{e^{\omega\sqrt{\frac{s}{D}}} - e^{-\omega\sqrt{\frac{s}{D}}}} \right) \quad (4.22)$$

With the values of $A'(s)$ and $B'(s)$ being known, the concentration of the electroactive species along the dimension μ of the electrolyte can be obtained from (4.16). To measure the depth of discharge $\rho(t)$ the concentration at the electrode is needed, that is, the value of $\bar{C}(x, s)$ for $x = 0$, presented in (4.23).

$$\bar{C}(0, s) = \frac{C^*}{s} - \frac{\bar{i}(s)\sqrt{D}}{nFSD\sqrt{s}} \left(\frac{e^{\omega\sqrt{\frac{s}{D}}} + e^{-\omega\sqrt{\frac{s}{D}}}}{e^{\omega\sqrt{\frac{s}{D}}} - e^{-\omega\sqrt{\frac{s}{D}}}} \right) \quad (4.23)$$

The hyperbolic cotangent of a given variable λ is given by (4.24).

$$\coth \lambda = \frac{e^\lambda + e^{-\lambda}}{e^\lambda - e^{-\lambda}} \quad (4.24)$$

applying the formula of the hyperbolic cotangent (4.24) to (4.23) results in (4.26).

$$\bar{C}(0, s) = \frac{C^*}{s} - \frac{\bar{i}(s)\sqrt{D}}{nFSD\sqrt{s}} \coth \left(\omega\sqrt{\frac{s}{D}} \right) \quad (4.25)$$

$$\bar{C}(0, s) = \frac{C^*}{s} - \frac{\bar{i}(s)}{nFSD} \frac{\coth(\omega\sqrt{\frac{s}{D}})}{\sqrt{\frac{s}{D}}} \quad (4.26)$$

let the inverse Laplace transform of $\frac{\coth(\omega\sqrt{\frac{s}{D}})}{\sqrt{\frac{s}{D}}}$ be given by (4.27).

$$\mathcal{L}^{-1} \left\{ \frac{\coth(\omega\sqrt{\frac{s}{D}})}{\sqrt{\frac{s}{D}}} \right\} = \sqrt{\frac{D}{\pi t}} \sum_{k=-\infty}^{\infty} e^{-\frac{\omega^2 k^2}{Dt}} \quad (4.27)$$

Considering (4.27) and that a multiplication in frequency is equivalent to a convolution in time, the inverse Laplace transform of (4.26) can be obtained, resulting in (4.29), which is the expression for the concentration of the electroactive species in the electrode through time.

$$C(0, t) = C^* - \frac{i_b(t)}{nFSD} * \sqrt{\frac{D}{\pi t}} \sum_{k=-\infty}^{\infty} e^{-\frac{\omega^2 k^2}{Dt}} \quad (4.28)$$

$$C(0, t) = C^* - \frac{1}{nFS\sqrt{\pi D}} \int_0^t \frac{i_b(\tau_0)}{\sqrt{t - \tau_0}} \sum_{k=-\infty}^{\infty} e^{-\frac{\omega^2 k^2}{D(t-\tau_0)}} d\tau_0 \quad (4.29)$$

Applying (4.29) to (4.3), results in equation (4.30).

$$\rho(t) = \frac{1}{nFS D \sqrt{\pi D C^*}} \int_0^t \frac{i_b(\tau_0)}{\sqrt{t - \tau_0}} \sum_{k=-\infty}^{\infty} e^{-\frac{\omega^2 k^2}{D(t-\tau_0)}} d\tau_0 \quad (4.30)$$

The relation (4.31) is valid for $Re(y) > 0$.

$$\sum_{k=-\infty}^{\infty} e^{-yk^2} = \sqrt{\frac{\pi}{y}} \sum_{k=-\infty}^{\infty} e^{-\frac{\pi^2 k^2}{y}} \quad (4.31)$$

Considering $y = \frac{\omega^2}{D(t-\tau_0)} > 0$, (4.32) can be written.

$$\sum_{k=-\infty}^{\infty} e^{-\frac{\omega^2 k^2}{D(t-\tau_0)}} = \sqrt{\frac{\pi D(t-\tau_0)}{\omega^2}} \sum_{k=-\infty}^{\infty} e^{-\frac{\pi D(t-\tau_0)k^2}{\omega^2}} \quad (4.32)$$

applying (4.32) to (4.30) leads to (4.33), which gives the depth of discharge through time.

$$\rho(t) = \frac{1}{nFS \omega C^*} \int_0^t i_b(\tau_0) \sum_{k=-\infty}^{\infty} e^{-\frac{\pi^2 D(t-\tau_0)k^2}{\omega^2}} d\tau_0 \quad (4.33)$$

since $k^2 = (-k)^2$ in the sum that can be seen in (4.33), arriving at (4.35).

$$\sum_{k=-\infty}^{\infty} e^{-\frac{\pi^2 D(t-\tau_0)k^2}{\omega^2}} = \sum_{k=-\infty}^{-1} e^{-\frac{\pi^2 D(t-\tau_0)k^2}{\omega^2}} + e^0 + \sum_{k=1}^{\infty} e^{-\frac{\pi^2 D(t-\tau_0)k^2}{\omega^2}} \quad (4.34)$$

$$\sum_{k=-\infty}^{\infty} e^{-\frac{\pi^2 D(t-\tau_0)k^2}{\omega^2}} = 1 + 2 \sum_{k=1}^{\infty} e^{-\frac{\pi^2 D(t-\tau_0)k^2}{\omega^2}} \quad (4.35)$$

the result of applying (4.35) to (4.33) is (4.36).

$$\rho(t) = \frac{1}{nFS \omega C^*} \left[\int_0^t i_b(\tau_0) d\tau_0 + 2 \sum_{k=1}^{\infty} \int_0^t i_b(\tau_0) e^{-\frac{\pi^2 D(t-\tau_0)k^2}{\omega^2}} d\tau_0 \right] \quad (4.36)$$

By specifying two parameters, $\beta = \frac{\pi \sqrt{D}}{\omega}$ and $\alpha = nFS \omega C^* \rho(L_b)$, it is possible to write the relationship between α , β , the total discharge time L_b and the current i_b as (4.37).

$$\alpha = \int_0^{L_b} i_b(\tau_0) d\tau_0 + 2 \sum_{k=1}^{\infty} \int_0^{L_b} i_b(\tau_0) e^{-\beta^2 k^2 (L-\tau_0)} d\tau_0 \quad (4.37)$$

(4.37) is the relationship between the time L_b needed for the battery to reach the cut-off voltage v_b , the discharge current $i_b(t)$, where the parameters α and β can be estimated from experimental data. These two parameters are a representation of the physical characteristics

of the battery, with α being the maximum charge of the battery, measured in coulombs, and β is the diffusion parameter of the diffusion of the electroactive species through the electrolyte, measured in $s^{-1/2}$. The total charge delivered by the battery to the external load is given by the first term of the right side of (4.37), while the second term represents the charge that cannot be delivered to the electroactive species in the surface of the electrode at the time instant $t = L_b$. The total charge consumed corresponding to discharge times smaller than L_b is given by (4.38), where the charge lost term is σ_d and the unavailable charge σ_u .

$$\sigma(t) = \sigma_d(t) + \sigma_u(t) = \int_0^t i_b(\tau_0) d\tau_0 + 2 \sum_{k=1}^{\infty} \int_0^t i_b(\tau_0) e^{-\beta^2 m^2 (L-\tau_0)} d\tau_0 \quad (4.38)$$

An ideal battery would be able to deliver all of its capacity to an external load. This means that for an ideal battery $\beta \rightarrow \infty$, which results in $\sigma_u \approx 0$. As β increases, the speed of the diffusion of the electroactive species increases, reaching the electrode faster. On the other hand, as β decreases, fewer ions are available at the electrode, since the diffusion speed decreases.

By applying the Laplace transform to (4.38) [Neves et al. 2016] the transfer function $H(s)$ between the input $\bar{I}_b(s) = \mathcal{L}[I_b(t)]$ and the output $\bar{\sigma}_b(s) = \mathcal{L}[\sigma(t)]$ is obtained, as can be seen in (4.39).

$$H(s) = \frac{\bar{\sigma}(s)}{\bar{I}_b(s)} = \frac{1}{s} + 2 \sum_{k=0}^{\infty} \frac{1}{s + \beta^2 k^2} \quad (4.39)$$

A steady-state solution can be obtained for the second term of (4.39) [Luiz, Lima & Lima 2022], considering a constant current I , which results in (4.40). Thus, the parameters of the diffusion model α and β can be estimated using (4.40) and performing multiple constant current discharge experiments. This procedure will be detailed further in this chapter.

$$\alpha = IL_b + \frac{\pi^2}{3\beta^2} I \quad (4.40)$$

The percentile error $\Delta_{\%}$ of the sum in (4.39) was calculated for the case in which the first k_0 terms are employed, resulting in (4.41). For example, in the case where the first 10 terms

of the sum are considered, $\Delta_{\%} = 5,78\%$.

$$\Delta_{\%} = \frac{\frac{\pi^2}{6\beta^2} - \frac{1}{\beta^2} \sum_{k=1}^{k_0} \frac{1}{k^2}}{\frac{\pi^2}{6\beta^2}} 100\% \quad (4.41)$$

Finally, the state of charge of the battery can be defined as shown in (4.42). The SOC is a percentile value that is obtained by calculating the normalized difference between the maximum charge α and the depth of discharge σ .

$$A(t) = 100 \left(\frac{\alpha - \sigma(t)}{\alpha} \right) \% \quad (4.42)$$

A limitation of the Rakhmatov-Vrudhula model is that it only provides the SOC of the battery, giving no information regarding the terminal voltage. The value of the SOC given by (4.42) needs to be related to the terminal voltage v_b , so that the model can not only predict how long the battery will take to discharge, but also can estimate the voltage during this process. In this work, an equivalent circuit model is employed for this purpose, being described in the following section.

4.3 Electrical model

The diffusion model presented in the previous section is able to represent part of the internal dynamics of the battery, but some relevant phenomena are not included in it. Additionally, if the aim is to obtain a model which can provide the battery voltage v_b in addition to its state of charge $A(t)$, a relation between these two variables must be established. For this purpose, an electrical model is employed. The coupling of an electrical model to a model that gives an estimation of the state of charge is a widely used strategy in battery modeling, as can be seen in [Lee, Dai & Chuang 2018], [Valladolid et al. 2019] and [Wang et al. 2022].

The electrical model used is shown in Fig. 4.3. The battery voltage v_b is given by (4.43), where $v_{oc}(t)$ is the open-circuit voltage of the battery as a function of the state of charge $f(A(t))$, and r_s is the series resistance. The dynamics of the voltage drop $v_{c_j}(t)$ for a given RC parallel circuit j is given by (4.44), where r_j and c_j are the resistance and capacitance, respectively. These parallel circuits model the fast dynamics at the battery electrode, which is not covered by the typically slower response of the diffusion model. This leads to the

inclusion of these additional parameters in the model, as otherwise there would be non-modeled dynamics when comparing the experimental data with the model response for the battery voltage. The relationship between the open-circuit voltage v_{oc} and the state of charge $A(t)$ can be obtained through a low discharge rate experiment, for which (4.45) is true.

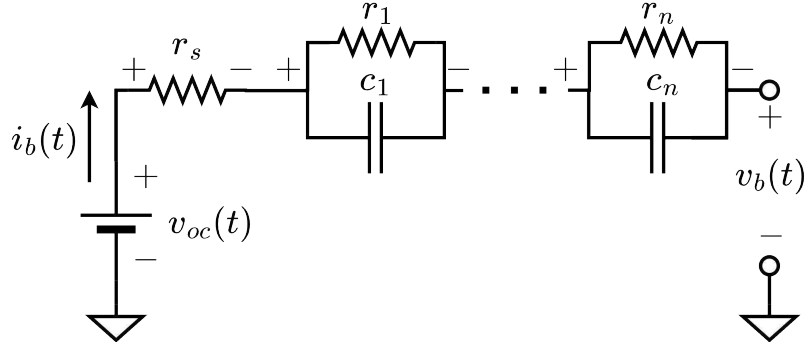


Figure 4.3: Electrical model for a LiPo battery.

$$v_b(t) = v_{oc}(t) - r_s i_b(t) - \sum_{j=1}^n v_{c_j}(t) \quad (4.43)$$

$$i_b(t) = \frac{v_{c_j}(t)}{r_j} + c_j \dot{v}_{c_j}(t) \quad (4.44)$$

$$v_b(t) \approx v_{oc}(t), \text{ for } i_b(t) \approx 0 \quad (4.45)$$

4.4 Discrete-time model

From this point forward, the models previously presented, which were already employed in the literature, will be combined into the proposed lumped parameter model for a LiPo battery. This combination is performed through the relationship between the open-circuit voltage v_{oc} and the state of charge $A(t)$, mentioned in the previous Section. The result is a model which can represent the state of charge by modeling the diffusion and provide an estimate of the battery voltage v_b through the ECM.

In order to apply an optimization algorithm to estimate the model parameters, a discrete-time version of the complete battery model had to be determined. The state-space for the

diffusion model for a given sampling time t_s can be seen in (4.46) and (4.47), where σ_d is the delivered charge state, σ_{um} are the unavailable charge states, $m \in [1, 2, \dots, M]$ and $k \in \mathbb{N}$ is the discrete time, where $t = kt_s$. The state of charge $A(k)$ is obtained from (4.48) and the open-circuit voltage is given by (4.49). Then, the state-space model of the ECM is given by (4.50) and (4.51).

$$\begin{bmatrix} \sigma_{u1}(k+1) \\ \sigma_{u2}(k+1) \\ \vdots \\ \sigma_{uM}(k+1) \\ \sigma_d(k+1) \end{bmatrix} = \begin{bmatrix} e^{-\beta^2 t_s} & 0 & \cdots & 0 & 0 \\ 0 & e^{-\beta^2 4t_s} & \cdots & 0 & 0 \\ \vdots & \vdots & \ddots & \vdots & \vdots \\ 0 & 0 & \cdots & e^{-\beta^2 M^2 t_s} & 0 \\ 0 & 0 & \cdots & 0 & 1 \end{bmatrix} \begin{bmatrix} \sigma_{u1}(k) \\ \sigma_{u2}(k) \\ \vdots \\ \sigma_{uM}(k) \\ \sigma_d(k) \end{bmatrix} + \begin{bmatrix} -\frac{e^{-\beta^2 t_s} - 1}{\beta^2} \\ -\frac{e^{-\beta^2 4t_s} - 1}{\beta^2 4} \\ \vdots \\ -\frac{e^{-\beta^2 M^2 t_s} - 1}{\beta^2 M^2} \\ t_s \end{bmatrix} i_b(k) \quad (4.46)$$

$$\sigma(k) = \begin{bmatrix} 2 & 2 & \cdots & 2 & 1 \end{bmatrix} \begin{bmatrix} \sigma_{u1}(k) \\ \sigma_{u2}(k) \\ \vdots \\ \sigma_{uM}(k) \\ \sigma_d(k) \end{bmatrix} \quad (4.47)$$

$$A(k) = 100 \frac{\alpha - \sigma(k)}{\alpha} \% \quad (4.48)$$

$$v_{oc}(k) = f(A(k)) \quad (4.49)$$

$$\begin{bmatrix} v_{c1}(k+1) \\ v_{c2}(k+1) \\ \vdots \\ v_{cn}(k+1) \end{bmatrix} = \begin{bmatrix} e^{-\frac{t_s}{r_1 c_1}} & 0 & \cdots & 0 \\ 0 & e^{-\frac{t_s}{r_2 c_2}} & \cdots & 0 \\ \vdots & \vdots & \ddots & \vdots \\ 0 & 0 & \cdots & e^{-\frac{t_s}{r_n c_n}} \end{bmatrix} \begin{bmatrix} v_{c1}(k) \\ v_{c2}(k) \\ \vdots \\ v_{cn}(k) \end{bmatrix} + \begin{bmatrix} -r_1 \left(e^{-\frac{t_s}{r_1 c_1}} - 1 \right) \\ -r_2 \left(e^{-\frac{t_s}{r_2 c_2}} - 1 \right) \\ \vdots \\ -r_n \left(e^{-\frac{t_s}{r_n c_n}} - 1 \right) \end{bmatrix} i_b(k) \quad (4.50)$$

$$v_b(k) = \begin{bmatrix} -1 & -1 & \cdots & -1 \end{bmatrix} \begin{bmatrix} v_{c1}(k) \\ v_{c2}(k) \\ \vdots \\ v_{cn}(k) \end{bmatrix} - r_s i_b(k) + f(A(k)) \quad (4.51)$$

This model is derived from the equations for the diffusion and electrical models shown in Sections 4.2 and 4.3, respectively. A block diagram showing how the equations relate to one another is presented in Fig. 4.4 for added clarity. The block diagram employs the Z transform to obtain the discrete-time transfer functions from (4.46) to (4.51), and the corresponding expressions are shown in (4.52)

$$\begin{aligned} \bar{\sigma}_d(z) &= \frac{z}{z-1} \bar{i}_b(z) \\ \bar{\sigma}_{um}(z) &= \left(2 \sum_{m=1}^M \left(\frac{z}{z - e^{-\beta^2 m^2}} \right) \right) \bar{i}_b(z) \\ \bar{\sigma}(z) &= \bar{\sigma}_d(z) + \bar{\sigma}_u(z) \\ A(k) &= 100 \frac{\alpha - \mathcal{Z}^{-1}[\bar{\sigma}(z)]}{\alpha} \% \\ v_{oc}(k) &= f(A(k)) \\ \bar{v}_{cj}(z) &= \frac{c_j^{-1} z}{z - e^{-\frac{1}{r_j c_j}}} \bar{i}_b(z) \\ v_b(k) &= v_{oc}(k) - r_s i_b(k) - \mathcal{Z}^{-1} \left[\sum_{j=1}^n \bar{v}_{cj}(z) \right] \end{aligned} \quad (4.52)$$

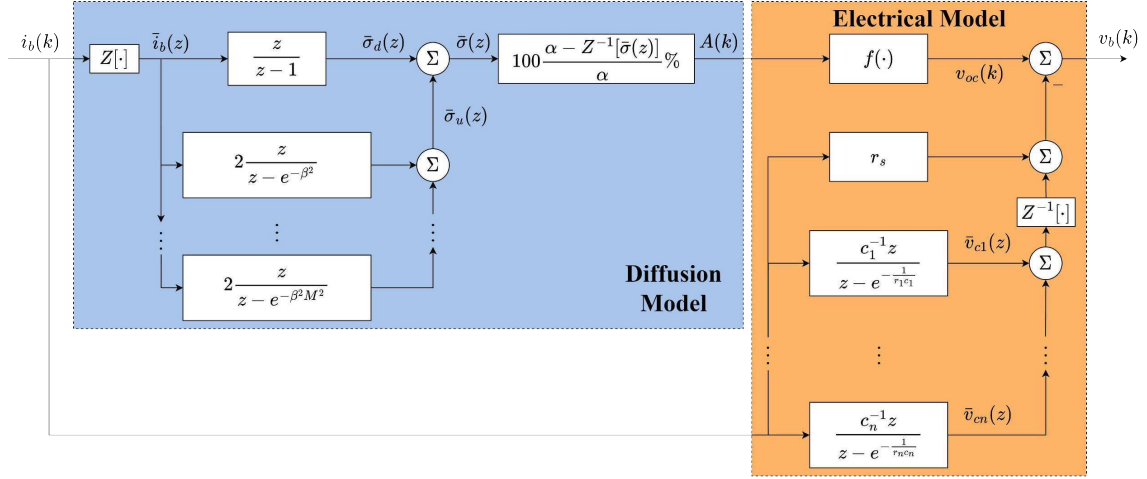


Figure 4.4: Block diagram of the battery model implementation.

4.5 Results

This section presents a set of results showing the proposed model's performance. The employed methods and materials are described, the steps and decisions taken during the modeling process are explained, an analysis of the choice of the number of RC branches is provided and the modeling results for several batteries are provided.

4.5.1 Methods and materials

The setup shown in Fig. 4.5 was employed to collect experimental discharge data from LiPo batteries. An EA-EL 9080 programmable DC load was used to set the discharge rate for each experiment, and an OWON XDM2041 digital multimeter was employed to measure the voltage between the battery terminals during the discharges. Although the DC load is capable of providing voltage data, its precision is limited to only the first decimal digit, thus demanding the inclusion of the multimeter for better precision.

As shown in the diagram, both devices were connected to a computer by serial connections, through which the measured data was transmitted and stored in log files.

The sampling time used is $t_s = 0.01 \text{ s}$, matching the sampling rate of the measuring hardware. The experimental data used in the parameter estimation was collected from three batteries in each of the cases shown next, in order to account for possible variations in the

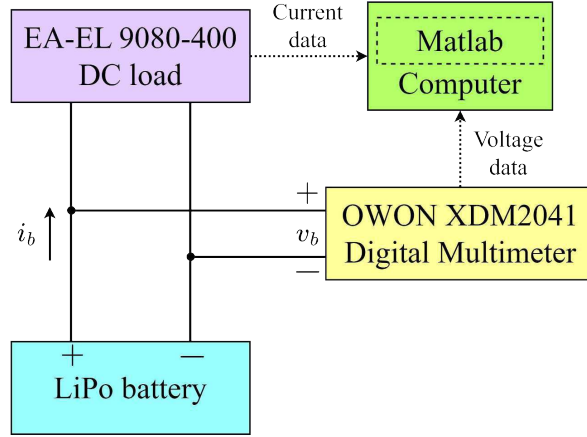


Figure 4.5: Experimental setup used to collect battery discharge data.

manufacturing process.

The model parameters are shown in the model equations in Section 4.4, which also describe the behavior of the battery dynamics. By analyzing these expressions, a set of experiments can be designed such that these parameters can be extracted from experimental data. These experiments are described below. From this point forward the notation $\hat{\epsilon}$ will be employed to refer to the estimate of a given variable or parameter ϵ .

1. The first experiments are constant current discharges to obtain the diffusion model parameters α and β , starting at the nominal discharge current value of each cell $1C$, and increasing by its multiples $2C$, $3C$, \dots and so on, until the battery discharges. An example of these currents with fictional times can be seen in Fig. 4.6. The resulting pairs of current and discharge times from these experiments can be employed to obtain the estimated $\hat{\alpha}$ and $\hat{\beta}$ by solving the optimization problem stated in (4.53).

$$\begin{aligned}
 [\hat{\alpha}, \hat{\beta}] &= \arg \min_{[\alpha, \beta]} \left(\frac{1}{N} \sum_{k=1}^N (L_b(k) - \hat{L}_b(k|[\alpha, \beta]))^2 \right) \\
 \text{s.t. } \hat{L}_b(k|[\alpha, \beta]) &= \frac{\alpha}{I(k)} - \frac{\pi^3}{3\beta^2} \\
 \alpha &\in \mathbb{R}_{\geq 0} \\
 \beta &\in [0, 1]
 \end{aligned} \tag{4.53}$$

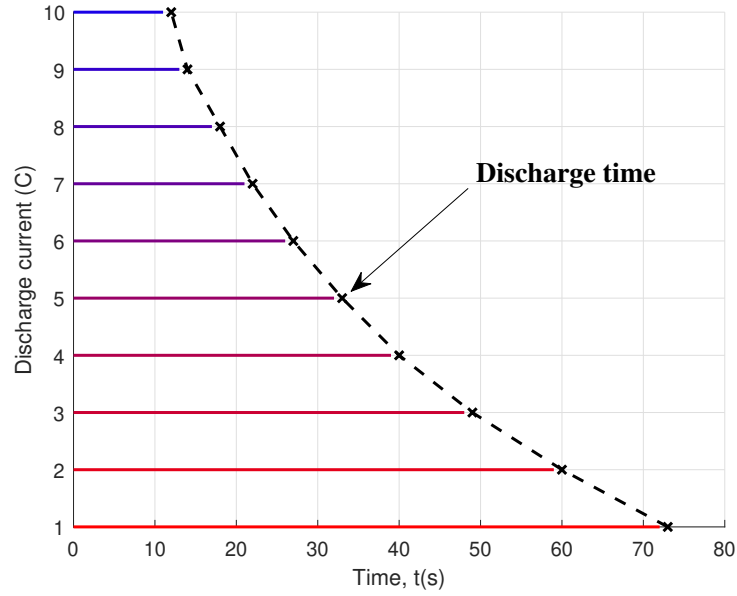


Figure 4.6: Example of the constant current discharge test currents.

- The next step in the modeling process is representing the open-circuit voltage v_{oc} as a function f of the state of charge $A(t)$. For this purpose, a constant current discharge at a current low enough such that $v_b \approx v_{oc}$ is performed until the battery is fully discharged. An example of the test current can be seen in Fig. 4.7. Then, \hat{f} can be obtained by solving the optimization problem stated in (4.54), where v_{oc}^{data} and v_{oc}^{estim} are the experimental and estimated open-circuit voltages, respectively. Notice that a choice regarding the mathematical expression of the function f must be made, such as a polynomial expression or Fourier expansion. This choice will be analyzed in a subsequent section.

$$\hat{f} = \arg \min_f \left(\frac{1}{N} \sum_{k=1}^N (v_{oc}(k) - f(A(k)))^2 \right) \quad (4.54)$$

s.t. Eqs. (4.46) to (4.49)

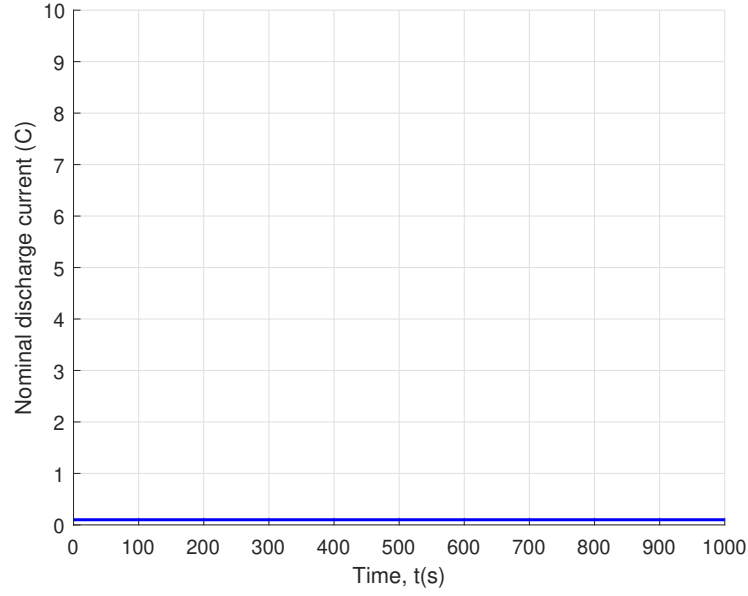


Figure 4.7: Example of the low current discharge test currents.

3. Finally, a pulsed current discharge at $10 C$ is conducted. The current pulses in this case are short in duration, followed by a long time where no current is drained, capturing the regeneration regime in the resulting experimental data. An example of the pulsed current signal can be seen in Fig. 4.8. This experiment allows the estimation of the electrical model parameters by solving the optimization problem stated in (4.55). Let $\mathbf{v} = [r_s \ r_1 \ \dots \ r_n \ c_1 \ \dots \ c_n] \in \mathbb{R}_{\geq 0}^{2n+1}$ be the ECM parameters vector and $\hat{\mathbf{v}}$ its estimate.

$$\begin{aligned} \hat{\mathbf{v}} &= \arg \min_{\mathbf{v}} \left(\frac{1}{N} \sum_{k=1}^N (v_b(k) - \hat{v}_b(k|\mathbf{v}))^2 \right) \\ \text{s.t. Eqs. (4.46) to (4.51)} \\ \mathbf{v} &\in \mathbb{R}_{\geq 0}^{2n+1} \end{aligned} \tag{4.55}$$

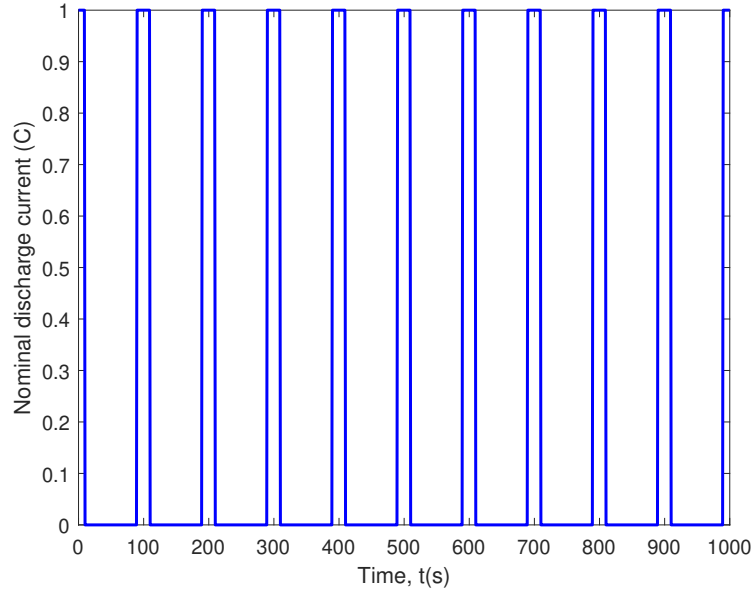


Figure 4.8: Example of the pulsed current discharge test currents.

Several error graphs will be shown to provide a quantitative measure of the modeling results. The estimation error e in these graphs is calculated as shown in (4.56), where x_{data} and x_{estim} are the experimental and the estimated values of a variable x , respectively. Its mean and maximum values will also be employed. The mean and maximum values of the estimation error shown in (4.56) will also be used, defined in (4.57) and (4.58) for N samples, respectively.

$$e(k) = 100 \left| \frac{x(k) - \hat{x}(k)}{x(k)} \right| \% \quad (4.56)$$

$$e_{\text{avg}} = \frac{1}{N} \sum_{k=1}^N e(k) \quad (4.57)$$

$$e_{\text{max}} = \max_{1 \leq k \leq N} |e(k)| \quad (4.58)$$

4.5.2 Analysis of the modeling process

The results from this section were obtained from a set of three GREPOW 32000 mAh, 3.8 V, 8 C batteries. The goal is to describe the decisions and conclusions gathered at each step of the modeling process.

Constant discharge experiments

The experimental data gathered from the constant current discharge experiments can be seen in Fig. 4.9, along with the estimated discharge times obtained from the diffusion model employing the parameters resulting from the solution of (4.53). The corresponding errors are shown in Fig. 4.10. The optimization problem in this case was solved by employing an interior point algorithm with an error tolerance of 10^{-6} . By observing the graphs, it is evident that the model is precise when it comes to predicting the discharge time for a given constant current, with the highest error among all cells being slightly greater than 2%.

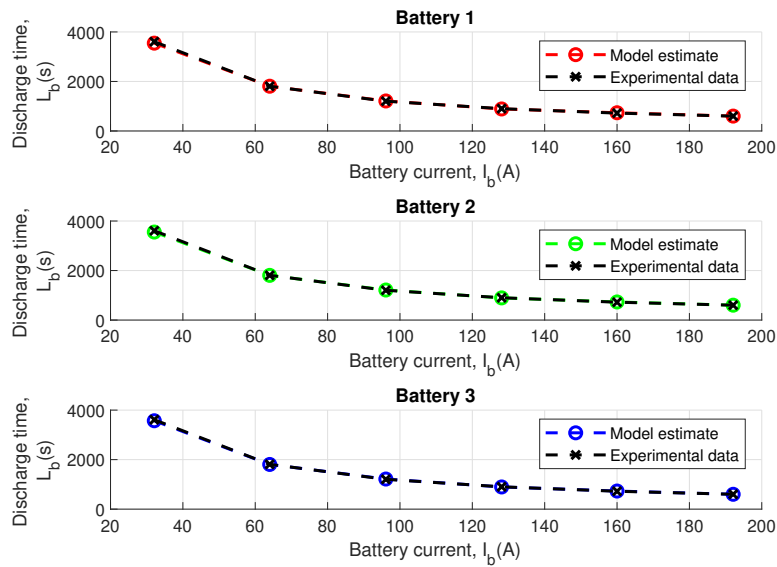


Figure 4.9: Comparison between experimental data and model prediction for constant current discharge times (GREPOW).

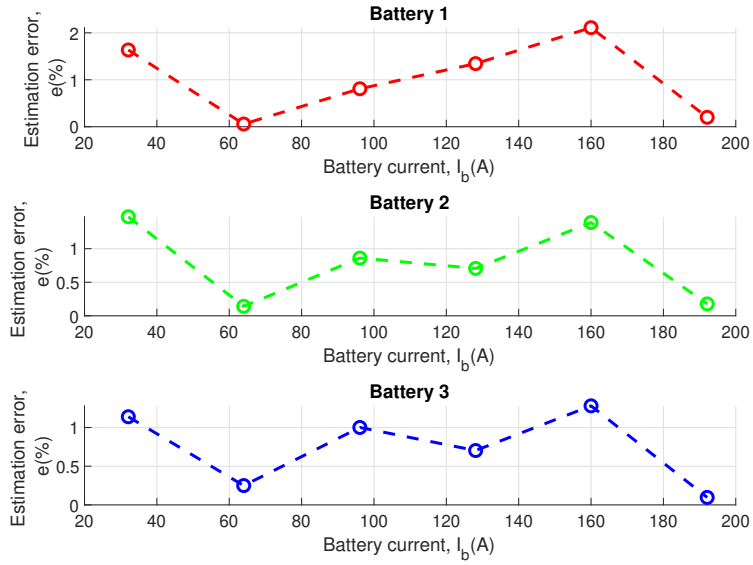


Figure 4.10: Estimation error for constant current discharge times (GREPOW).

Low discharge rate experiment

It was stated that in order to find $v_{oc}(k) = f(A(k))$ the optimization problem (4.54) must be solved. This formulation of the optimization problem assumes that the SOC $A(k)$ is known, which implies that α and β have been correctly estimated. While the results shown in Figs. 4.9 and 4.10 indicate that this might be the case, it will be shown in the next section that the diffusion parameter β must be re-estimated. Therefore, the optimization problem (4.54) must be reformulated to be independent of this parameter.

Considering that in this case the steady-state solution presented in (4.40) is valid, for a small value of I the unavailable charge term of the diffusion model can be considered negligible, as the discharge time L_b will be large. This means that, in this case, the state of charge is approximately linear, and can be obtained from the integral of the current. Then, the optimization problem for obtaining the expression for v_{oc} presented in (4.54) must be rewritten for this case, which is shown in (4.59).

$$\begin{aligned}
\hat{f} &= \arg \min_f \left(\frac{1}{N} \sum_{k=1}^N (v_{oc}(k) - \hat{v}_{oc}(k))^2 \right) \\
\text{s.t. } \hat{v}_{oc}(k) &= f(A(k)) \\
A(k) &= \frac{\alpha - \sigma(k)}{\alpha} \% \\
\sigma(k) &= i_b(k)t_s + \sigma(k-1)
\end{aligned} \tag{4.59}$$

A choice must be made regarding the expression of the open-circuit voltage as a function f of the state of charge $A(k)$. Three approaches were tested: a 9th degree polynomial expression, a 7th order Fourier series approximation, and linear curve interpolation. The order of the mathematical expressions was chosen as the lowest order that gave a mean error under 1 %, to avoid using high-order expressions unnecessarily. Due to the discharge times of twelve to fourteen hours for a low current, there are plenty of data points for the interpolation, meaning that linear interpolation can be chosen at no cost in modeling error instead of more complex interpolation algorithms. The experimental data and the corresponding v_{oc} model curves for each cell can be seen in Figs. 4.11 to 4.13, along with their estimation error.

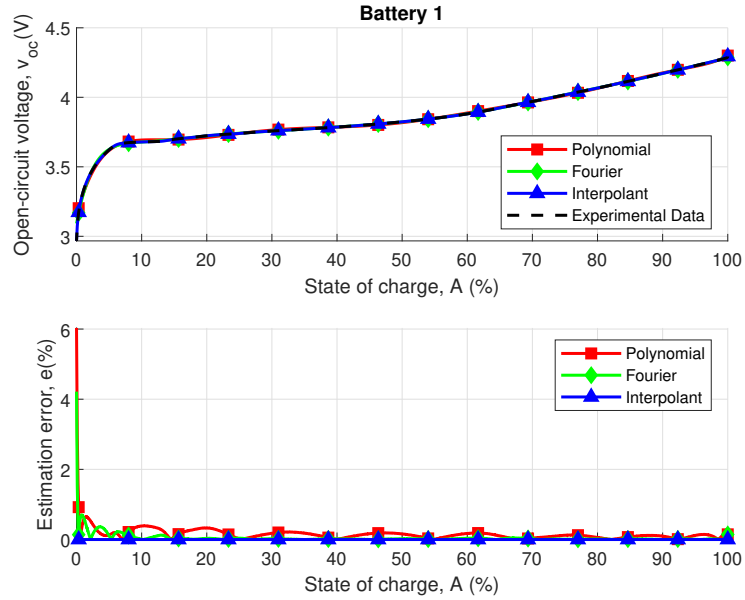


Figure 4.11: Open circuit voltage estimation results for cell 1 (GREPOW).

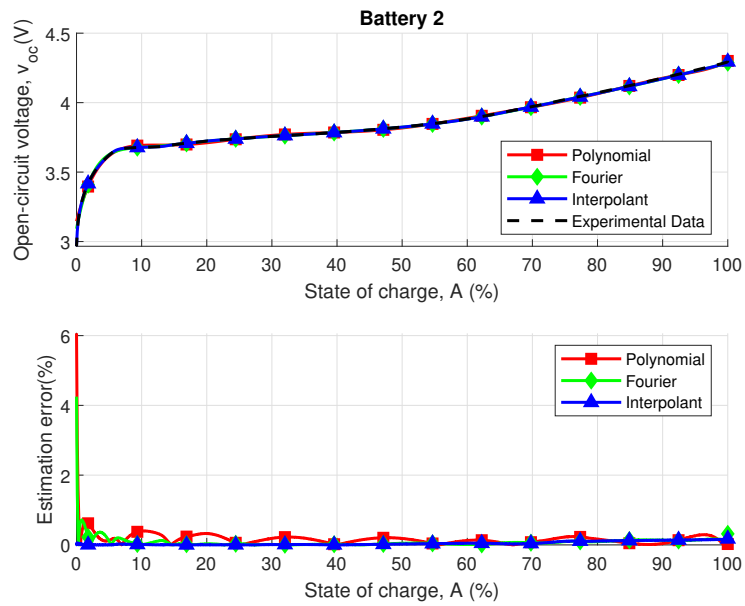


Figure 4.12: Open circuit voltage estimation results for cell 2 (GREPOW).

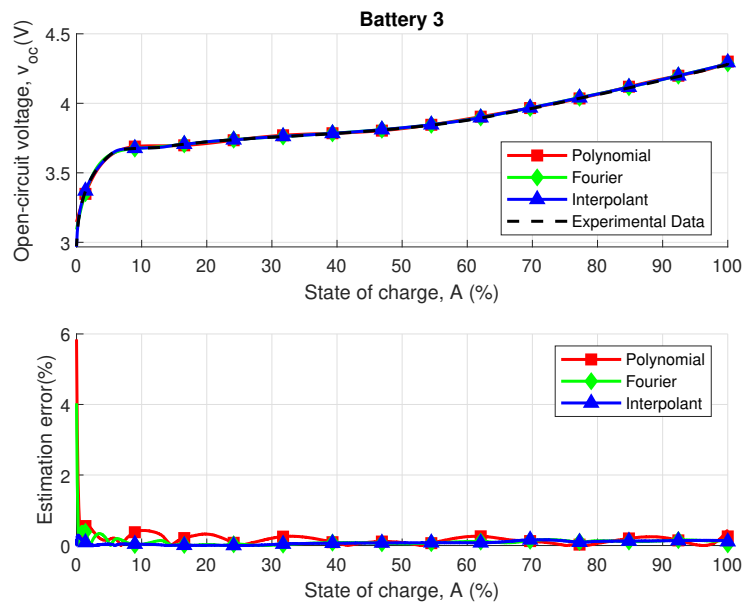


Figure 4.13: Open circuit voltage estimation results for cell 3 (GREPOW).

The interpolated alternative outperforms the polynomial and Fourier expressions. It should be noted that this conclusion is a consequence of the long duration of this experiment, which generates a rich data set from which the interpolation can be calculated. However, if an explicit mathematical expression is desired for the open circuit voltage, the other

alternatives present a good performance except for the very low state of charge values. The corresponding estimation error metrics for each battery are shown in Tables 4.1 to 4.3.

Table 4.1: Open circuit voltage estimation error metrics for battery 1.

	Mean error (%)	Maximum error (%)
Polynomial	0.149	6.031
Fourier	0.041	4.216
Interpolation	0.032	0.098

Table 4.2: Open circuit voltage estimation error metrics for battery 2.

	Mean error (%)	Maximum error (%)
Polynomial	0.165	6.066
Fourier	0.076	4.250
Interpolation	0.046	0.172

Table 4.3: Open circuit voltage estimation error metrics for battery 3.

	Mean error (%)	Maximum error (%)
Polynomial	0.173	5.845
Fourier	0.099	4.033
Interpolation	0.078	0.296

Pulsed current experiment

As described before, the pulsed current experiments are used to estimate the parameters of the ECM. By analyzing the optimization problem for this step as it is stated in (4.55), the number of RC parallel circuits employed must also be determined. For the purposes of this study, a single parallel circuit was deemed enough to model the corresponding dynamics, as the addition of extra parallel circuits resulted in the increase of the parameter estimation time at no significant increase in model precision. The inclusion of extra branches is particularly costly, as the related parameters do not have evident estimation bounds, and providing

initial values for the optimization algorithm demands previous system knowledge. The optimization problem can then be re-stated as in (4.60). Let $\boldsymbol{\chi} = \begin{bmatrix} r_s & r_1 & c_1 \end{bmatrix} \in \mathbb{R}_{\geq 0}^3$ be the parameter vector for the ECM model with one RC parallel circuit, and $\hat{\boldsymbol{\chi}}$ its estimate.

$$\hat{\boldsymbol{\chi}} = \arg \min_{\boldsymbol{\chi}} \left(\frac{1}{N} \sum_{k=1}^N (v_b(k) - \hat{v}_b(k|\boldsymbol{\chi}))^2 \right)$$

$$\text{s.t. } \hat{v}_b(k|\boldsymbol{\chi}) = v_{oc}(k) - r_s i_b(k) - v_{c1}(k)$$

$$v_{c1}(k) = e^{-\frac{t_s}{r_1 c_1}} v_{c1}(k-1) - r_1 \left(e^{-\frac{t_s}{r_1 c_1}} - 1 \right) i_b(k-1)$$

$$v_{oc}(k) = f(A(k))$$

$$A(k) = \frac{\alpha - \sigma(k)}{\alpha} \%$$

$$\sigma(k) = \begin{bmatrix} 2 & \dots & 2 & 1 \end{bmatrix} \begin{bmatrix} \sigma_{u1}(k) \\ \vdots \\ \sigma_{u10}(k) \\ \sigma_d(k) \end{bmatrix}$$

$$\begin{bmatrix} \sigma_{u1}(k+1) \\ \vdots \\ \sigma_{u10}(k+1) \\ \sigma_d(k+1) \end{bmatrix} = \begin{bmatrix} e^{-\beta^2 t_s} & \dots & 0 & 0 \\ \vdots & \ddots & \vdots & \vdots \\ 0 & \dots & e^{-\beta^2 100 t_s} & 0 \\ 0 & \dots & 0 & 1 \end{bmatrix} \begin{bmatrix} \sigma_{u1}(k) \\ \vdots \\ \sigma_{u10}(k) \\ \sigma_d(k) \end{bmatrix} + \begin{bmatrix} -\frac{e^{-\beta^2 t_s} - 1}{\beta^2} \\ \vdots \\ -\frac{e^{-\beta^2 100 t_s} - 1}{\beta^2 100} \\ t_s \end{bmatrix} i_b(k)$$

$$\boldsymbol{\chi} \in \mathbb{R}^3$$

(4.60)

Before a more complete analysis of the solution for this optimization problem was performed, preliminary results were obtained to validate this approach. These preliminary results for the three batteries can be seen in Fig. 4.14, where the model estimate of the battery voltage is compared against the experimental data. It is visible in the graphs that the model is not able to properly model the battery dynamics. Since the diffusion parameter obtained by solving (4.53) had been estimated from a constant current discharge it did not reflect the dynamics of the regeneration regime, which leads to the poor behavior observed in Fig. 4.14. This showed the need to estimate a new value for β .

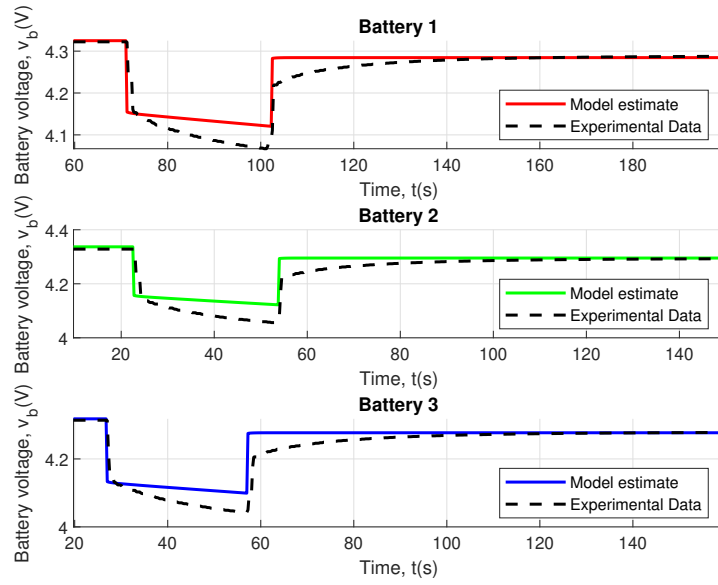


Figure 4.14: Model response for the constant current estimated β .

Since the regeneration regime is well represented in the pulsed current experiment data set, it is proposed that the optimization problem stated in (4.60) can be reformulated to also include the estimation of the diffusion parameter β , which would lead to a better performing model. This results in the optimization problem stated in (4.61), where both the ECM model parameters and the diffusion parameter are estimated. Let $\vartheta = \begin{bmatrix} \beta & r_s & r_1 & c_1 \end{bmatrix} \in [0, 1] \times \mathbb{R}_{\geq 0}^3$ be the model parameters vector, and $\hat{\vartheta}$ its estimate. The results presented later will show that this approach resulted in a better-performing model.

$$\begin{aligned}
\hat{\boldsymbol{\vartheta}} &= \arg \min_{\boldsymbol{\vartheta}} \left(\frac{1}{N} \sum_{k=1}^N (v_b(k) - \hat{v}_b(k|\boldsymbol{\vartheta}))^2 \right) \\
\text{s.t. } \hat{v}_b(k|\boldsymbol{\vartheta}) &= v_{oc}(k) - r_s i_b(k) - v_{c1}(k) \\
v_{c1}(k) &= e^{-\frac{t_s}{r_1 c_1}} v_{c1}(k-1) - r_1 \left(e^{-\frac{t_s}{r_1 c_1}} - 1 \right) i_b(k-1) \\
v_{oc}(k) &= f(A(k)) \\
A(k) &= \frac{\alpha - \sigma(k)}{\alpha} \% \\
\sigma(k) &= \begin{bmatrix} 2 & \dots & 2 & 1 \end{bmatrix} \begin{bmatrix} \sigma_{u1}(k) \\ \vdots \\ \sigma_{u10}(k) \\ \sigma_d(k) \end{bmatrix} \\
\begin{bmatrix} \sigma_{u1}(k+1) \\ \vdots \\ \sigma_{u10}(k+1) \\ \sigma_d(k+1) \end{bmatrix} &= \begin{bmatrix} e^{-\beta^2 t_s} & \dots & 0 & 0 \\ \vdots & \ddots & \vdots & \vdots \\ 0 & \dots & e^{-\beta^2 100 t_s} & 0 \\ 0 & \dots & 0 & 1 \end{bmatrix} \begin{bmatrix} \sigma_{u1}(k) \\ \vdots \\ \sigma_{u10}(k) \\ \sigma_d(k) \end{bmatrix} + \begin{bmatrix} -\frac{e^{-\beta^2 t_s} - 1}{\beta^2} \\ \vdots \\ -\frac{e^{-\beta^2 100 t_s} - 1}{\beta^2 100} \\ t_s \end{bmatrix} i_b(k) \\
\hat{\boldsymbol{\vartheta}} &\in [0, 1] \times \mathbb{R}_{\geq 0}^3
\end{aligned} \tag{4.61}$$

As this step is the most computationally intensive, it is of interest to study the performance of different optimization algorithms when solving it. The following numerical approaches have been evaluated in this step, all of them widely employed in the scientific literature and capable of dealing with constrained nonlinear optimization:

- Interior point: Interior point algorithms work by moving the solution point in the objective function within a feasible area. Details can be found in [Nocedal, Öztoprak & Waltz 2014].
- Sequential Quadratic Programming (SQP): SQP methods represent a state-of-the-art approach to solving constrained nonlinear optimization problems. It approximates Newton's method for constrained problems. An overview can be found in [Fletcher 2000].
- Levenberg-Marquadt: This algorithm is employed to solve nonlinear least-squares

curve fitting problems. An in-depth analysis can be found in [Kelley 1999].

- Genetic Algorithm: This method solves constrained nonlinear problems by mimicking a biological evolution model, successively modifying a population made of possible solutions for the problem. A control engineering-focused discussion is conducted in [Chipperfield & Fleming 1996].
- Particle Swarm Optimization (PSO): This algorithm simulates a swam of particles distributed over the solution space, selecting those that converge to the minima or maxima. Details are available in [Kennedy & Eberhart 1995].
- Simulated Annealing: This method simulates the cooling of a hot metal plate according to the optimality of a given solution within the solution space to solve constrained nonlinear problems. A discussion regarding this method is had in [Ingber 1995].

All of those algorithms had a step tolerance of 10^{-6} , with the same initial values being used for the interior point, SQP, active set, and Levenberg-Marquadt. The genetic algorithm had a population of 100 and a maximum number of generations of 1000. The PSO had a swarm of 100 particles, uniformly distributed, with an inertia range of $[0.1, 1]$. The genetic algorithm had a population of 100. In all cases the maximum number of iterations is set to $200 n_{\text{vars}}$, with n_{vars} being the number of constants to be estimated, and the maximum number of stall iterations is 20.

The results for each of the three batteries are presented in Figs. 4.15 to 4.17, with the estimation error, mean and maximum values for each case shown in Tables 4.4 to 4.6. For better readability of the results, only one of the multiple pulses is shown in the graphs. Each pulse had a duration of 30 s, with a subsequent rest time of 29 min30 s. They were applied until the terminal voltage reached the cut-off voltage. An observation must be made here, as the Levenberg-Marquadt results are not shown in the graphs. This happened because this algorithm had very poor performance when compared to the other alternatives. Due to the potential for visual obfuscation, it was determined to exclude these data points from the graphical representation and instead present only the associated error metrics in tabular form.

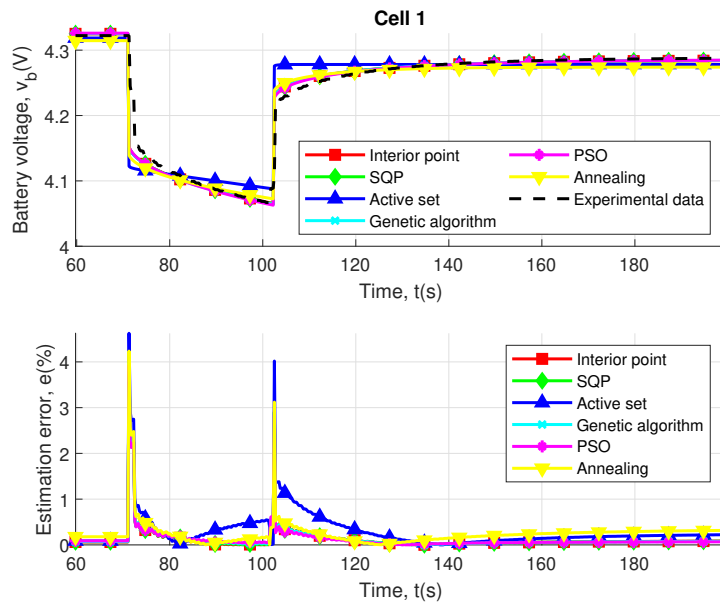


Figure 4.15: Model responses for battery 1 (GREPOW).

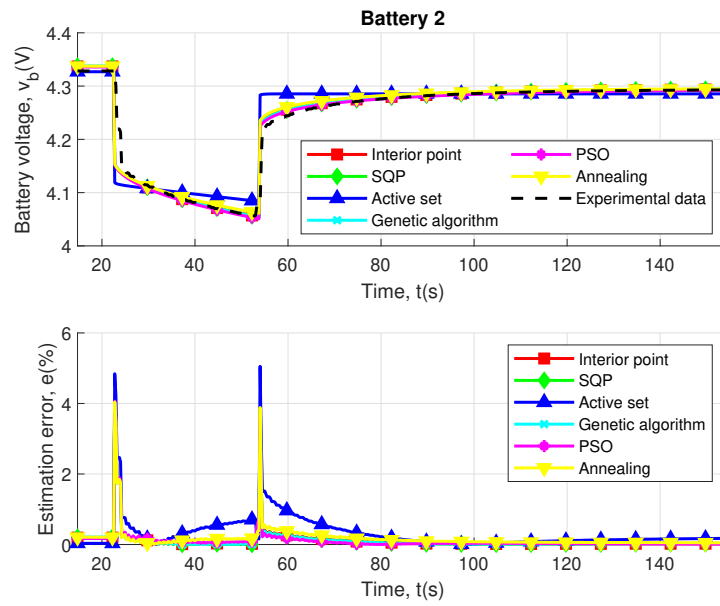


Figure 4.16: Model responses for battery 2 (GREPOW).

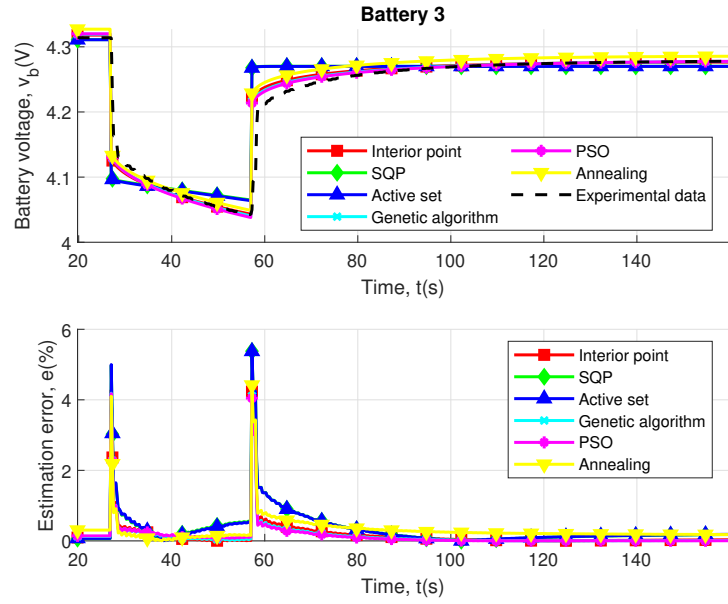


Figure 4.17: Model responses for battery 3 (GREPOW).

Table 4.4: Battery voltage estimation error metrics for battery 1.

	Mean error (%)	Maximum error (%)
Interior point	0.120	3.962
SQP	0.119	3.954
Active set	0.290	4.624
Genetic algorithm	0.122	3.968
Levenberg-Marquadt	14.918	19.710
PSO	0.126	3.938
Simulated Annealing	0.211	4.236

Table 4.5: Battery voltage estimation error metrics for battery 2.

	Mean error (%)	Maximum error (%)
Interior point	0.111	4.050
SQP	0.108	4.033
Active set	0.310	5.051
Genetic algorithm	0.107	4.027
Levenberg-Marquadt	16.257	21.967
PSO	0.095	4.064
Simulated Annealing	0.158	4.041

Table 4.6: Battery voltage estimation error metrics for battery 3.

	Mean error (%)	Maximum error (%)
Interior point	0.150	4.277
SQP	0.325	5.380
Active set	0.324	5.375
Genetic algorithm	0.130	4.188
Levenberg-Marquadt	17.149	24.082
PSO	0.128	4.175
Simulated Annealing	0.295	4.417

When evaluating the performance of the obtained models and the corresponding optimization algorithms, the most important factor is how well the physical dynamics of the battery were represented. Additionally, it is desirable for the modeling approach to be applicable to any LiPo battery, provided that the necessary experimental data is available. Keeping these factors in mind, it is visible that the active set approach was fair, but had the worst performance among the other approaches, with the mean and maximum errors higher than the alternatives by around 0.2 % and 1 %, respectively. The Levenberg-Marquadt algorithm was not able to find an adequate solution to the optimization problem, which is reflected in the error metrics.

The interior point, SQP, genetic algorithm, PSO and simulated annealing identified models had a mostly similar behavior across all three cells, presenting a mean estimation error under 1 % and a maximum estimation error of around 4 % in the transient response. This shows that the combination of the Rakhmatov-Vrudhula diffusion model and the electrical model can accurately represent the behavior of these batteries.

At a closer inspection, it can be seen that the SQP model for Battery 3 had metrics similar to that of the active set alternative. This can be either due to a specific characteristic of this battery manufacturing or to a particularity of the data set which made the algorithm settle for a local minimum, but since the other algorithms did not suffer the same problem, they should be considered over the SQP approach, so that the resulting model is less prone to error due to such factors.

The choice between the interior point, genetic algorithm, PSO, and simulated annealing can be guided by their metrics during the optimization process, which can be seen in Table 4.7, which shows the time it took each algorithm to estimate the model parameters, on Matlab R2021a running on Windows 10 in a computer with an Intel(R) Core(TM) i5-10300H 2.50 GHz CPU and 16 GB of RAM memory. The interior point algorithm was by far the fastest, not considering the active set approach, which had precision problems. The interior point algorithm ran in under a minute with no significant loss in model accuracy. However, the performance of this algorithm is reliant upon an initial guess for the variables, which demands previous system knowledge regarding values likely to be in the vicinity of the correct ones. The genetic algorithm, PSO, and simulated annealing have strategies that allow them to search over a wider range of possibilities, at the cost of a much higher execution time

for this specific case, as becomes evident from examining the execution times in the table. Therefore, if a reasonable guess can be obtained for the initial values and the application demands a fast execution time of the algorithm, the interior point is the better choice. In those cases where the execution time is not a restriction and no reasonable guess for a starting point can be made, the other alternatives might be preferable.

Table 4.7: Execution time for the optimization algorithms.

	Battery 1 (s)	Battery 2 (s)	Battery 3 (s)
Interior point	36.392	44.559	31.272
SQP	16.486	14.931	6.832
Active set	6.103	6.042	5.916
Genetic algorithm	6882.383	1468.587	2332.450
Levenberg-Marquadt	57.732	59.074	58.795
PSO	12584.441	10547.718	9874.524
Simulated Annealing	13374.558	7058.637	11222.890

Modeling guide

The information regarding the modeling process acquired in the previous section can then lead to a modeling guide to obtaining the proposed model, which is shown in Fig. 4.18. Each experiment is associated with the required estimation steps to obtain one or more of the model components, which can then be combined to obtain the complete battery model.

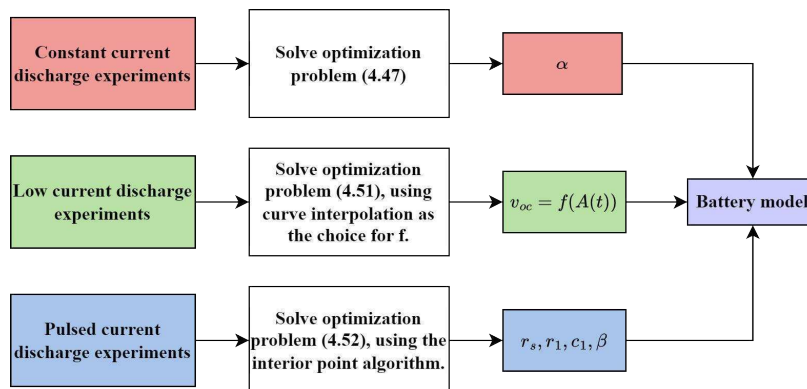


Figure 4.18: Steps for obtaining the LiPo battery model.

Model parameters

The parameter models resulting from the modeling process described above are shown in Tables 4.8 through 4.10 for the active set approach. All values are relatively close to each other, with the differences being between the expected margins due to variations in the manufacturing process and the noise in the measurements obtained from the experiments.

Table 4.8: Model parameters for battery 1, interior point (GREPOW).

$\hat{\alpha}$	$\hat{\beta}$	\hat{r}_s	\hat{r}_1	\hat{c}_1
$1.1586 \times 10^5 C$	$0.2074 s^{-1/2}$	0.0016Ω	$1.0238 \times 10^{-6} \Omega$	$500.0597 F$

Table 4.9: Model parameters for battery 2, interior point (GREPOW).

$\hat{\alpha}$	$\hat{\beta}$	\hat{r}_s	\hat{r}_1	\hat{c}_1
$1.1590 \times 10^5 C$	$0.1810 s^{-1/2}$	0.0017Ω	$4.5346 \times 10^{-6} \Omega$	$500.2820 F$

Table 4.10: Model parameters for battery 3, interior point (GREPOW).

$\hat{\alpha}$	$\hat{\beta}$	\hat{r}_s	\hat{r}_1	\hat{c}_1
$1.1603 \times 10^5 C$	$0.2018 s^{-1/2}$	0.0017Ω	$2.7461 \times 10^{-6} \Omega$	$500.9338 F$

4.5.3 Analysis of the RC parallel circuits

In the previous section, during the parameter estimation step using the pulsed current data, it was stated that a choice must be made regarding the number of RC parallel circuits used in the model. It was then said that, in the case studied here, a single RC parallel circuit was deemed sufficient, as the inclusion of extra circuits brought an increase in the execution time of the optimization algorithm, due to the increased number of variables, with no discernible gain in the error metrics.

A study was conducted to verify this claim, where the number of parallel circuits was increased, the model parameters estimated and the execution time and error metrics compared. The data from the same GREPOW cells was used. The active set algorithm was employed, as it was shown to be the fastest. This resulted in the graphs shown in Figs. 4.19 through 4.21, where the execution time is shown in the top graph against the number of circuits and the mean estimation error in the bottom one.

The graphs show an increase in execution time as the number of parallel circuits increases, while the error metrics remain around the same value. These results show that the increase in the number of RC parallel circuits would add complexity with no clear gain to the resulting model.

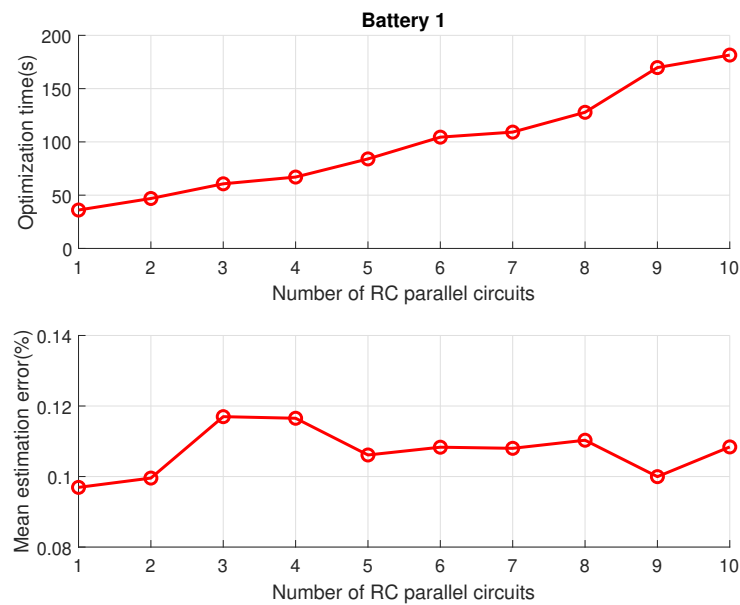


Figure 4.19: Comparison between optimization time and mean estimation error for battery 1 (GREPOW).

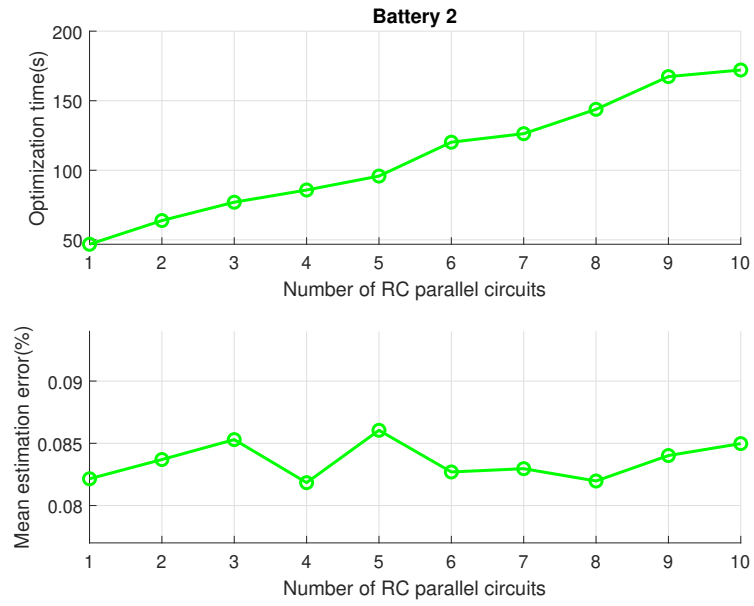


Figure 4.20: Comparison between optimization time and mean estimation error for battery 2 (GREPOW).

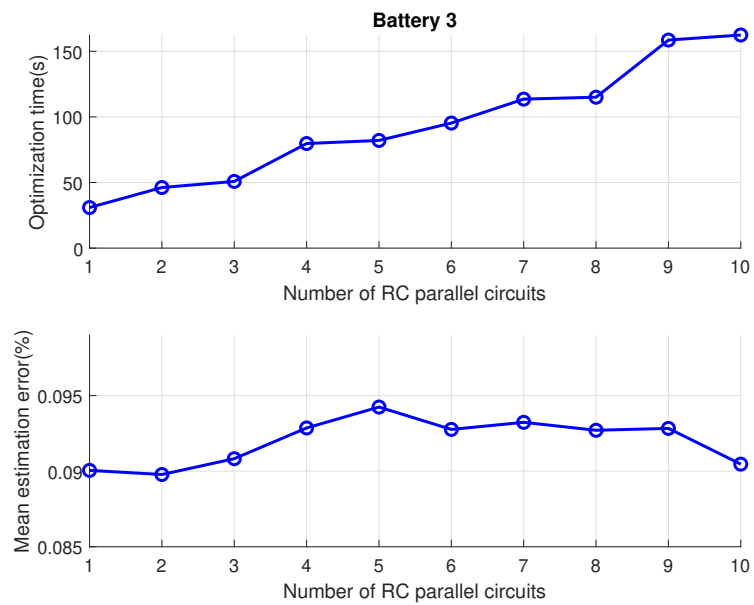


Figure 4.21: Comparison between optimization time and mean estimation error for battery 3 (GREPOW).

4.5.4 GiFi Power 600 mAh 3.7 V 15 C results

The results of the modeling of the GiFi Power 600 mAh, 3.7 V, 15 C batteries, used to power the Parrot Mambo, are presented in this section. Once again, three batteries were used to take into account variations from the manufacturing process. The modeling approach employed is the one described in Section 4.5.2, and summarized in Fig. 4.18.

Constant discharge tests

As established when the modeling process was analyzed, the first step is to employ the results of the constant current discharge experiments to find the battery capacity α . The experimental data and the resulting models are shown in Figs. 4.22 through 4.24. The presented graphs show that the diffusion model is able to accurately predict the discharge time for a given current, with the estimation error remaining close to or smaller than 1 %.

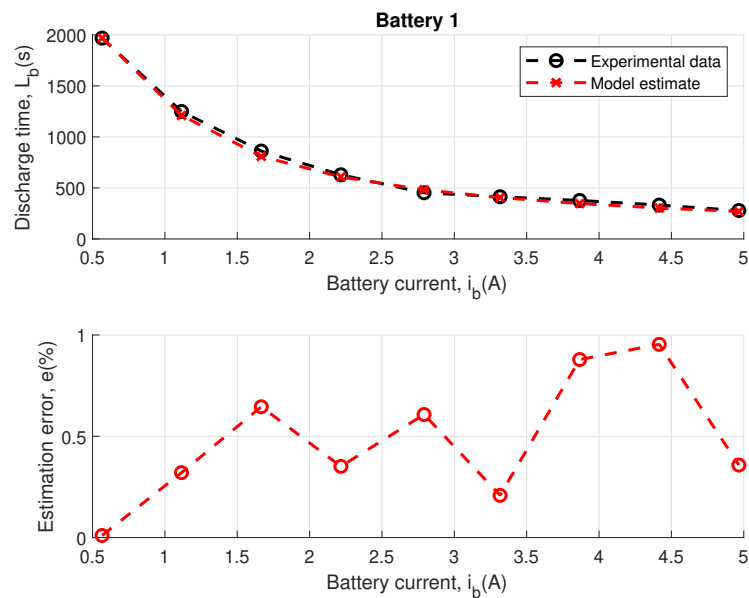


Figure 4.22: Estimation error for constant current discharges for battery 1 (GiFi Power).

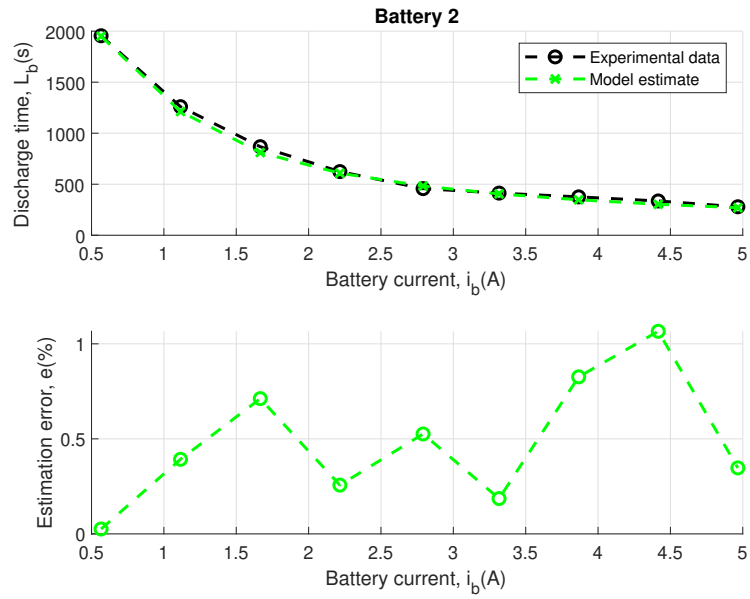


Figure 4.23: Estimation error for constant current discharges for battery 2 (GiFi Power).

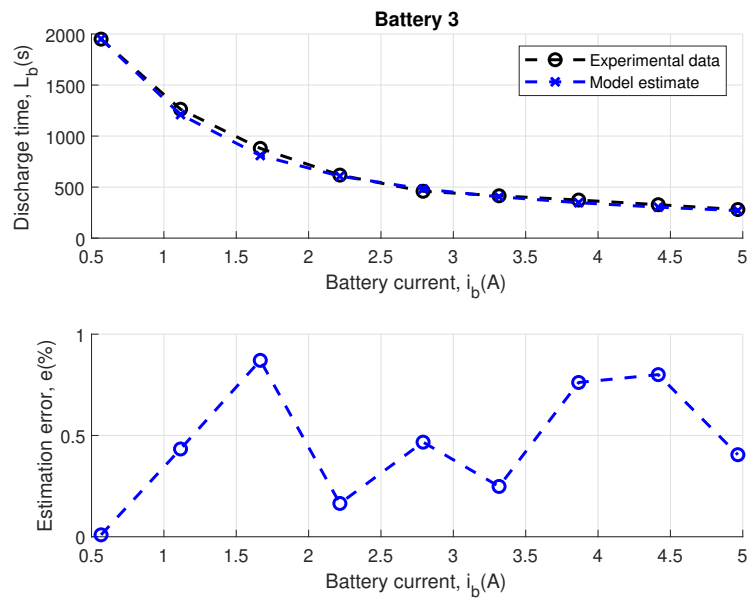


Figure 4.24: Estimation error for constant current discharges for battery 3 (GiFi Power).

Low discharge rate test

The next step is obtaining a relation between the open-circuit voltage and the state of charge $v_{oc} = f(A(t))$. This can be done by performing a low current discharge test. The experimental data and estimated open-circuit voltage are shown for the three cells in Figs. 4.25 through 4.27. The expression was obtained through linear interpolation, as it was previously shown that this option led to the lowest error amongst those explored. Although the error varies between the cells and depending on the region of the graph, it remains under 1 % at all times, attesting that the resulting expressions are able to accurately estimate the open-circuit voltage from the state of charge.

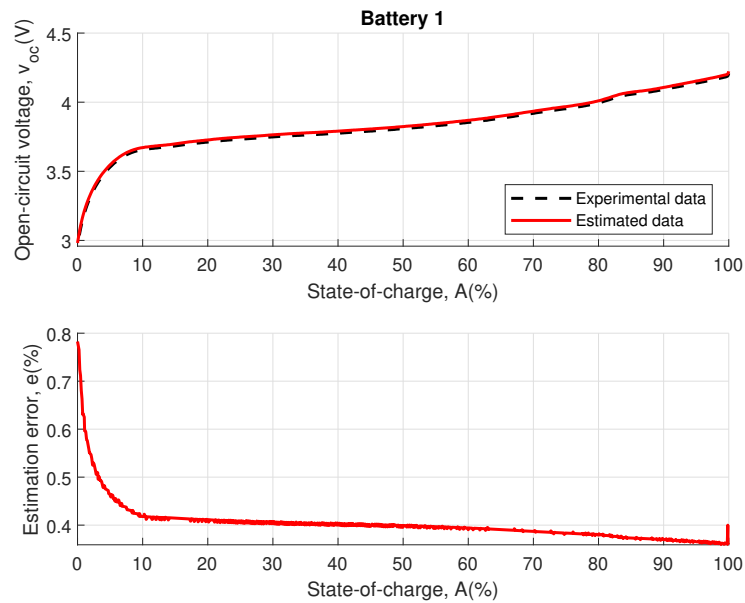


Figure 4.25: Open circuit voltage estimation results for battery 1 (GiFi Power).

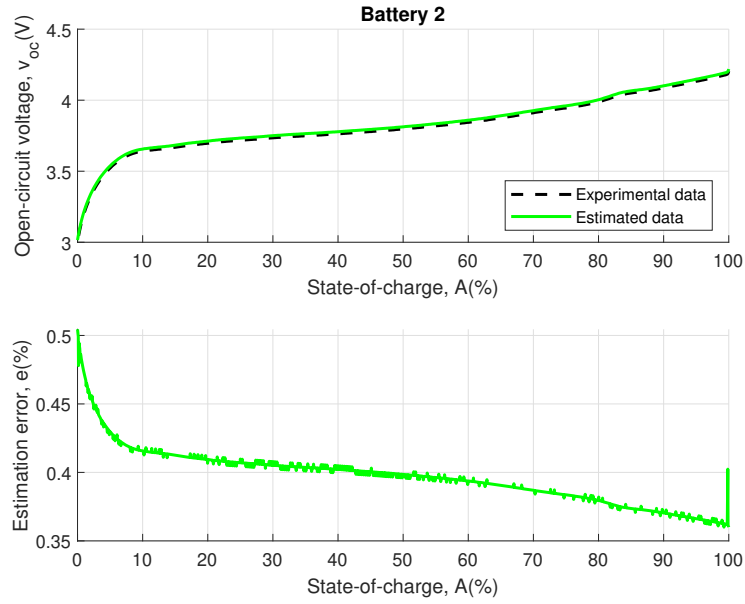


Figure 4.26: Open circuit voltage estimation results for battery 2 (GiFi Power).

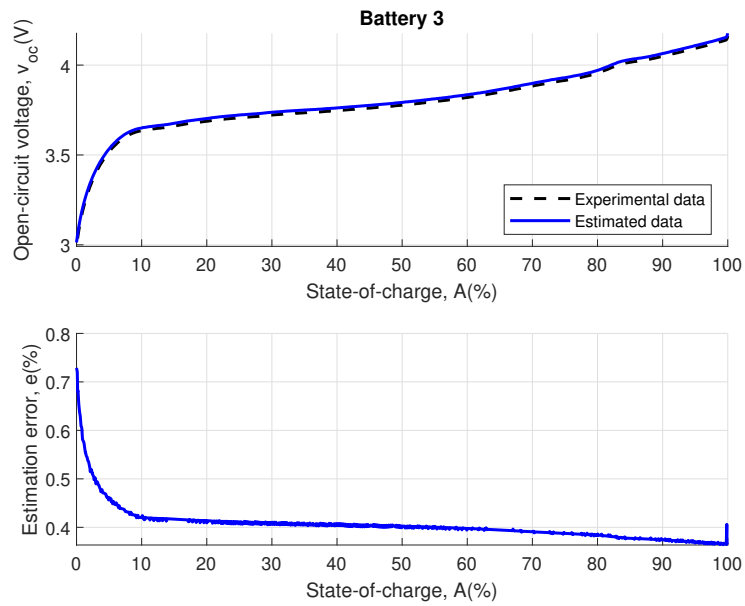


Figure 4.27: Open circuit voltage estimation results for battery 3 (GiFi Power).

Pulsed current test

The data from the pulsed current tests are used to obtain the parameters from the electrical model and to re-estimate the diffusion parameter β . The chosen modeling approach was the interior point algorithm. The experimental data from each battery and associated estimated response from the resulting models can be seen in Figs. 4.28 through 4.30. Once again,

the error remains under 1%, showing that the adopted modeling approach that combines the Rakhmatov-Vrudhula model with an electrical model can accurately represent the dynamic behavior of a LiPo battery.

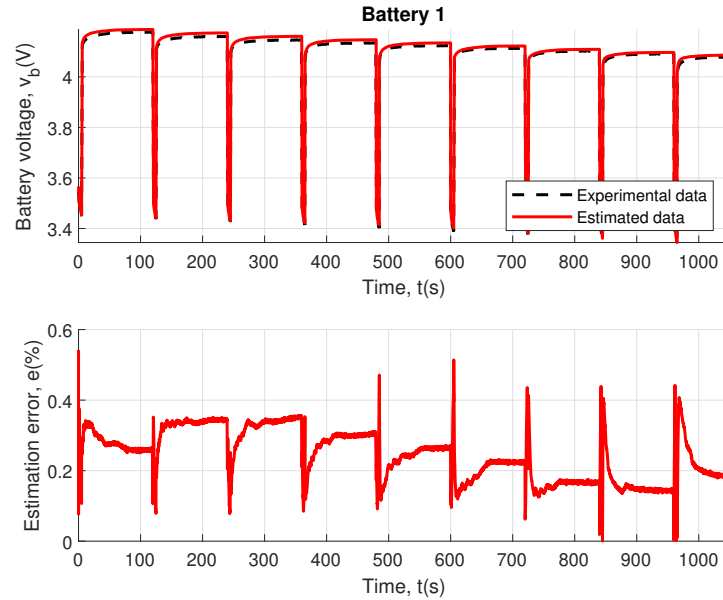


Figure 4.28: Model responses for battery 1 (GiFi Power).

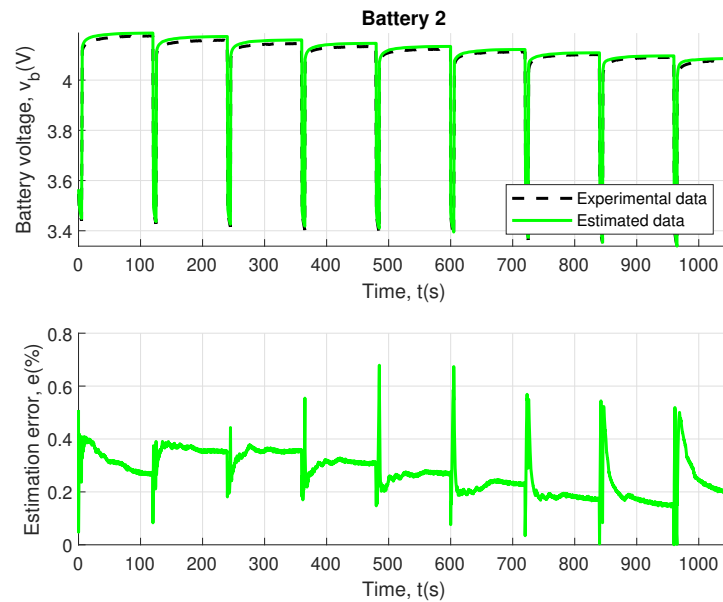


Figure 4.29: Model responses for battery 2 (GiFi Power).

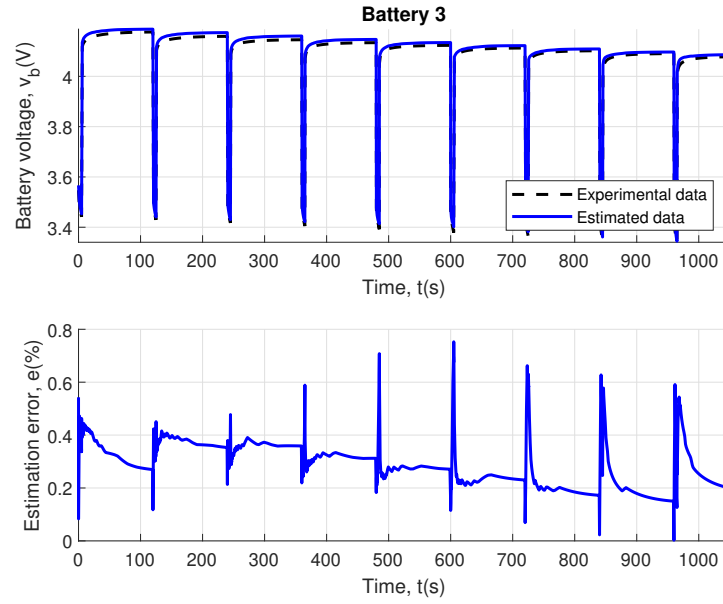


Figure 4.30: Model responses for battery 3 (GiFi Power).

Model parameters

The parameter models resulting from the modeling process described above are shown in Tables 4.11 through 4.13 for the interior point approach. All values are relatively close to each other, with the differences being between the margins expected due to variations in the manufacturing process and measurement noise in the experimental data.

Table 4.11: Model parameters for battery 1, interior point (GiFi Power).

$\hat{\alpha}$	$\hat{\beta}$	\hat{r}_s	\hat{r}_1	\hat{c}_1
$1.3536 \times 10^3 C$	$0.1924 s^{-1/2}$	0.1314Ω	$2.3643 \times 10^{-5} \Omega$	$10.1739 F$

Table 4.12: Model parameters for battery 2, interior point (GiFi Power).

$\hat{\alpha}$	$\hat{\beta}$	\hat{r}_s	\hat{r}_1	\hat{c}_1
$1.3555 \times 10^5 C$	$0.2038 s^{-1/2}$	0.1316Ω	$1.9728 \times 10^{-5} \Omega$	$10.1826 F$

Table 4.13: Model parameters for battery 3, interior point (GiFi Power).

$\hat{\alpha}$	$\hat{\beta}$	\hat{r}_s	\hat{r}_1	\hat{c}_1
$1.3533 \times 10^5 C$	$0.1966 s^{-1/2}$	0.1315Ω	$1.0077 \times 10^{-5} \Omega$	$10.1325 F$

4.6 Partial conclusions

In this chapter, the proposed battery model for LiPo batteries was presented, describing the combination of the Rakhmatov-Vrudhula diffusion model with an ECM model. This resulted in a model expressed through a set of discrete-time equations which is able to estimate the terminal voltage, open-circuit voltage, and SOC. The experimental procedure to estimate the model parameters was shown and the decisions taken in the modeling process were justified. The model was able to estimate the voltage for two sets of different batteries by employing the described experimental methodology.

With the battery model presented in this chapter and the other quadrotor mini drone system components described in Chapter 3, all of the components of the integrated model for the quadrotor mini drone used in this work have been properly modeled. The next step is to use this knowledge of the quadrotor mini drone model to analyze the impact of the varying battery voltage and the motor on the altitude and attitude dynamics, which is the subject of the following chapter.

Chapter 5

Analysis of the closed-loop altitude and attitude dynamics

In this chapter, a mathematical analysis of the effects of the electrical subsystem over the altitude and attitude dynamics of a quadrotor mini drone is performed. This study is made possible by the comprehension of the various system components, which were detailed in the previous chapters. The mathematical analysis performed in this chapter leads to a set of expressions that describe how the motor constant and the varying voltage from the battery affect the attitude and altitude dynamics. A small signal model is used to study how the closed-loop poles are affected. The conclusion is that the dynamics get slower as the battery discharges. Two approaches are proposed to remedy this effect over the closed-loop dynamics, one based on the controller design and another which uses the battery voltage to determine the motor commands. Additionally, a discussion on how the reference dynamics of the attitude control loop affect the energy consumption of the vehicle is performed.

5.1 Altitude loop analysis

This section shows the effects of the drop in battery voltage during the flight over the altitude error dynamics. An expression of the altitude dynamics taking into account the drop in battery voltage is derived. Further insights into the altitude loop dynamics can be obtained from a linear approximation around an operating point. The concepts employed here are reliant upon the models presented in Chapters 3 and 4, and, when necessary, equations from

those Chapters will be repeated for added clarity.

Equation (5.1) is the expression for the duty cycle and equation (5.2) is the mechanical equilibrium equation of the motor for the steady-state condition $\dot{\omega}_i = 0$, first presented in Chapter 3. It bears reminding that in the cases where the battery voltage is unknown, the nominal value $v_{b,0}$ is used to determine the duty cycle.

$$D_i = \frac{1}{k_e v_{b,0}} [(k_e^2 + r_a b) \omega_{i,C} + r_a k_N \omega_{i,C}^2] \quad (5.1)$$

$$0 = k_e D_i v_b - (k_e^2 + r_a b) \omega_i - r_a k_N \omega_i^2 \quad (5.2)$$

Applying (5.1) to (5.2) results in (5.4), where $\gamma = \frac{k_e^2 + r_a b}{r_a k_N} > 0$ and the ratio between the actual battery voltage and the nominal battery voltage is $\xi = \frac{v_b}{v_{b,0}} \in [0, 1]$. The square of the angular speed of the motors is then given by (5.5)

$$0 = \omega_i^2 + \frac{k_e^2 + r_a b}{r_a k_N} \omega_i - \frac{v_b}{v_{b,0}} \left(\omega_{i,C}^2 + \frac{k_e^2 + r_a b}{r_a k_N} \omega_{i,C} \right) \quad (5.3)$$

$$0 = \omega_i^2 + \gamma \omega_i - \xi (\omega_{i,C}^2 + \gamma \omega_{i,C}) \quad (5.4)$$

$$\omega_i^2 = \xi \omega_{i,C}^2 + \gamma (\xi \omega_{i,C} - \omega_i) \quad (5.5)$$

The expression (5.5) is then applied to the control allocation, which is shown in (5.6), resulting in (5.7).

$$\begin{bmatrix} L \\ M \\ N \\ T \end{bmatrix} = \mathbf{B} \begin{bmatrix} \omega_1^2 \\ \omega_2^2 \\ \omega_3^2 \\ \omega_4^2 \end{bmatrix} \quad (5.6)$$

$$\begin{bmatrix} L \\ M \\ N \\ T \end{bmatrix} = \xi \begin{bmatrix} L_C \\ M_C \\ N_C \\ T_C \end{bmatrix} + \mathbf{B} \begin{bmatrix} \gamma (\xi \omega_{1,C} - \omega_1) \\ \gamma (\xi \omega_{2,C} - \omega_2) \\ \gamma (\xi \omega_{3,C} - \omega_3) \\ \gamma (\xi \omega_{4,C} - \omega_4) \end{bmatrix} \quad (5.7)$$

The last line in (5.7), corresponding to the altitude dynamics, can be written as (5.8).

$$T = \xi T_C + k_T \gamma \sum_{i=1}^4 (\xi \omega_{i,C} - \omega_i) \quad (5.8)$$

Considering the cases in which $\omega_1 = \omega_2 = \omega_3 = \omega_4 = \omega$ and $\omega_{1,C} = \omega_{2,C} = \omega_{3,C} = \omega_{4,C} = \omega_C$, which corresponds to the cases where the quadrotor either maintains or changes altitude while keeping all of the attitude torques at zero, (5.9) is obtained, where it becomes explicit that the altitude dynamics are affected by ξ , which is directly related to the battery voltage.

$$T = \xi T_C + 4k_T \gamma (\xi \omega_C - \omega) \quad (5.9)$$

The expression (5.9) also shows that the resulting thrust is affected by the motor parameters, due to the presence of γ . If the commanded motor speed ω_C can be presumed to be close to the actual motor speed ω , then, in the ideal case where $\xi = 1$, which implies that $v_b = v_{b,0}$, the second term of (5.9) is negligible and $T = T_C$. However, as the battery voltage decreases during flight, then $\xi < 1$, which means that $T \neq T_C$. Since the desired dynamics are dependent upon the commanded thrust, this means that as the battery discharges, the system behavior will deteriorate.

It is possible to write ω as a function of ω_C by using (5.4), resulting in (5.10), which can be applied to (5.9) to obtain (5.11).

$$\omega = \frac{-\gamma + \sqrt{\gamma^2 + 4\xi(\omega_C^2 + \gamma\omega_C)}}{2} \quad (5.10)$$

$$T = \xi T_C + 4k_T \gamma \left(\xi \omega_C + \frac{\gamma - \sqrt{\gamma^2 + 4\xi(\omega_C^2 + \gamma\omega_C)}}{2} \right) \quad (5.11)$$

Further analysis of the closed-loop behavior is dependent upon the controller choice, which, for this work, is the NDI. The commanded thrust by the NDI is shown in (5.12), where the pseudo-control signal is of the form (5.13), and K_{e_z} , $K_{e_{Iz}}$ and $K_{\dot{e}_z}$ are the proportional, integral and derivative altitude error controller gains, respectively.

$$T_C = m \frac{g - \nu_Z}{\cos \Phi \cos \Theta} \quad (5.12)$$

$$\nu_Z = \ddot{Z}_R + K_{e_Z} e_Z + K_{e_{\dot{Z}}} \int_0^t e_Z d\tau_0 + K_{\dot{e}_Z} \dot{e}_Z \quad (5.13)$$

As the focus of the present analysis is on the altitude dynamics, the approximation $\cos \Phi \cos \Theta \approx 1$ can be considered for the cases where the vehicle maintains its position fixed on the horizontal plane, while changing its altitude. Therefore, (5.12) can be rewritten as (5.14).

$$T_C = m(g - \nu_Z) \quad (5.14)$$

The altitude dynamics are shown in (5.15). Considering that $\cos \Phi \cos \Theta \approx 1$, (5.16) can be written by applying (5.14) and (5.11) to (5.15).

$$\ddot{Z} = g - \frac{T}{m} \cos \Phi \cos \Theta \quad (5.15)$$

$$\begin{aligned} \ddot{Z} &= g - \frac{T}{m} \\ &= g - \xi(g - \nu_Z) - \frac{4k_T \gamma}{m} \left(\xi \omega_C + \frac{\gamma - \sqrt{\gamma^2 + 4\xi(\omega_C^2 + \gamma \omega_C)}}{2} \right) \\ &= f(\nu_Z, \omega_C, \xi) \end{aligned} \quad (5.16)$$

The error dynamics of the altitude closed-loop is given by (5.17), where Z_R is the altitude reference signal.

$$\ddot{e}_Z = \ddot{Z}_R - \ddot{Z} = \ddot{Z}_R - f(\nu_Z, \omega_C, \xi) \quad (5.17)$$

If the motors have the same speed, the allocation matrix gives $T_C = 4k_T \omega_C^2$, which leads to (5.18).

$$\omega_C = \sqrt{\frac{T_C}{4k_T}} = \sqrt{\frac{m(g - \nu_Z)}{4k_T}} = u(\nu_Z) \quad (5.18)$$

Therefore, applying (5.18) to (5.17) leads to (5.19).

$$\ddot{e}_Z = \ddot{Z}_R - f(\nu_Z, u(\nu_Z), \xi) \quad (5.19)$$

The expression for ν_Z can be seen in (5.13), which allows rewriting (5.19) as (5.20), where $e_{IZ} = \int_0^t e_Z(\tau_0) d\tau_0$.

$$\ddot{e}_Z = h(\ddot{Z}_R, e_Z, \dot{e}_Z, e_{IZ}, \xi) \quad (5.20)$$

To analyze (5.20) a small signals approximation can be obtained around an operating point $O = h(\ddot{Z}_0, e_{Z0}, \dot{e}_{Z0}, e_{IZ0}, \xi_0)$. This approximation is of the form (5.21), where the coefficients A_1, A_2, A_3 and B_1 are shown in (5.22), (5.23), (5.24) and (5.25).

$$\begin{bmatrix} \dot{e}_{iZ} \\ \dot{e}_Z \\ \ddot{e}_Z \end{bmatrix} = \begin{bmatrix} 0 & 1 & 0 \\ 0 & 0 & 1 \\ -A_1(\xi) & -A_2(\xi) & -A_3(\xi) \end{bmatrix} \begin{bmatrix} e_{IZ} \\ e_Z \\ \dot{e}_Z \end{bmatrix} + \begin{bmatrix} 0 \\ 0 \\ B_1(\xi) \end{bmatrix} \ddot{Z}_R \quad (5.21)$$

$$A_1(\xi) = \left. \frac{\partial h(\ddot{Z}_R, e_Z, \dot{e}_Z, e_{IZ}, \xi)}{\partial e_{IZ}} \right|_O \quad (5.22)$$

$$A_2(\xi) = \left. \frac{\partial h(\ddot{Z}_R, e_Z, \dot{e}_Z, e_{IZ}, \xi)}{\partial e_Z} \right|_O \quad (5.23)$$

$$A_3(\xi) = \left. \frac{\partial h(\ddot{Z}_R, e_Z, \dot{e}_Z, e_{IZ}, \xi)}{\partial \dot{e}_Z} \right|_O \quad (5.24)$$

$$B_1(\xi) = \left. \frac{\partial h(\ddot{Z}_R, e_Z, \dot{e}_Z, e_{IZ}, \xi)}{\partial \ddot{Z}_R} \right|_O \quad (5.25)$$

The operation point considered is a steady-state regime from a step command in altitude. As such, it is presumed that the error is constant and equal to zero. This translates into $\ddot{Z}_R = 0, e_Z = 0, \dot{e}_Z = 0$ e $e_{IZ} = 0$, with ξ considered constant. A transfer function (5.26) can be obtained from (5.21).

$$\frac{e_Z(s)}{Z_R(s)} = \frac{B_1(\xi)s^3}{s^3 + A_3(\xi)s^2 + A_2(\xi)s + A_1(\xi)} \quad (5.26)$$

The coefficients A_1, A_2, A_3 and B_1 are dependent on ξ , meaning that the poles of the transfer function (5.26) change when the battery voltage v_b gets smaller than the nominal voltage $v_{b,0}$ during the vehicle flight. The poles can be obtained by solving the characteristic polynomial of (5.26), allowing an analysis of the system response as ξ varies. The expanded expressions of $h(\ddot{Z}_R, e_Z, \dot{e}_Z, e_{IZ}, \xi)$ and the coefficients A_1, A_2, A_3 and B_1 can be seen in

equations (5.27) through (5.31). Note that the choice of the gains in the expression for ν_Z will also bear influence upon the placement of the poles.

$$\begin{aligned} \ddot{e}_Z &= h(\ddot{Z}_R, e_Z, \dot{e}_Z, e_{IZ}, \xi) \\ &= \ddot{Z}_R - g + \xi(g - \ddot{Z}_R - K_{\dot{e}_Z}\dot{e}_Z - K_{e_Z}e_Z - K_{e_{IZ}}e_{IZ}) + \frac{4k_T\gamma}{m} \left(\xi \sqrt{\frac{m(g - \ddot{Z}_R - K_{\dot{e}_Z}\dot{e}_Z - K_{e_Z}e_Z - K_{e_{IZ}}e_{IZ})}{4k_T}} \right) \\ &\quad - \frac{4k_T\gamma}{m} \left(\frac{-\gamma + \sqrt{\gamma^2 + 4\xi \left(\frac{m(g - \ddot{Z}_R - K_{\dot{e}_Z}\dot{e}_Z - K_{e_Z}e_Z - K_{e_{IZ}}e_{IZ})}{4k_T} \right) + \gamma \sqrt{\frac{m(g - \ddot{Z}_R - K_{\dot{e}_Z}\dot{e}_Z - K_{e_Z}e_Z - K_{e_{IZ}}e_{IZ})}{4k_T}}}}{2} \right) \end{aligned} \quad (5.27)$$

$$A_1 = \frac{4\gamma k_t \xi \left(\frac{K_{e_{IZ}}m}{4k_t} + \frac{\gamma K_{e_{IZ}}}{8k_t \sqrt{\frac{g - K_{e_{IZ}}\epsilon}{4k_t}}} \right)}{m \sqrt{4\xi \left(\gamma \sqrt{\frac{g - K_{e_{IZ}}\epsilon}{4k_t}} + \frac{m(g - K_{e_{IZ}}\epsilon)}{4k_t} \right) + \gamma^2}} - \frac{\gamma K_{e_{IZ}}\xi}{2\sqrt{\frac{m(g - K_{e_{IZ}}\epsilon)}{4k_t}}} - \xi K_{e_{IZ}} \quad (5.28)$$

$$A_2 = \frac{4\gamma k_t \xi \left(\frac{K_{e_Z}m}{4k_t} + \frac{\gamma K_{e_Z}}{8k_t \sqrt{\frac{g - K_{e_{IZ}}\epsilon}{4k_t}}} \right)}{m \sqrt{4\xi \left(\gamma \sqrt{\frac{g - K_{e_{IZ}}\epsilon}{4k_t}} + \frac{m(g - K_{e_{IZ}}\epsilon)}{4k_t} \right) + \gamma^2}} - \frac{\gamma K_{e_Z}\xi}{2\sqrt{\frac{m(g - K_{e_{IZ}}\epsilon)}{4k_t}}} - \xi K_{e_Z} \quad (5.29)$$

$$A_3 = \frac{4\gamma k_t \xi \left(\frac{K_{\dot{e}_Z}m}{4k_t} + \frac{\gamma K_{\dot{e}_Z}}{8k_t \sqrt{\frac{g - K_{e_{IZ}}\epsilon}{4k_t}}} \right)}{m \sqrt{4\xi \left(\gamma \sqrt{\frac{g - K_{e_{IZ}}\epsilon}{4k_t}} + \frac{m(g - K_{e_{IZ}}\epsilon)}{4k_t} \right) + \gamma^2}} - \frac{\gamma K_{\dot{e}_Z}\xi}{2\sqrt{\frac{m(g - K_{e_{IZ}}\epsilon)}{4k_t}}} - \xi K_{\dot{e}_Z} \quad (5.30)$$

$$B_1 = \frac{4\gamma k_t \xi \left(\frac{m}{4k_t} + \frac{\gamma}{8k_t \sqrt{\frac{g - K_{e_{IZ}}\epsilon}{4k_t}}} \right)}{m \sqrt{4\xi \left(\gamma \sqrt{\frac{g - K_{e_{IZ}}\epsilon}{4k_t}} + \frac{m(g - K_{e_{IZ}}\epsilon)}{4k_t} \right) + \gamma^2}} - \frac{\gamma \xi}{2\sqrt{\frac{m(g - K_{e_{IZ}}\epsilon)}{4k_t}}} - \xi + 1 \quad (5.31)$$

5.2 Attitude loop analysis

This section studies the closed-loop attitude dynamics taking into account the variations in the battery voltage. The starting point is the expressions for the duty cycle and steady-state of the motor, shown in the analysis of the altitude loop in (5.1) and (5.2). It was shown in the previous section that from these equations it is possible to arrive at (5.32), which, when applied to the allocation matrix, results in (5.33).

$$\omega_i^2 = \xi \omega_{i,C}^2 + \gamma (\xi \omega_{i,C} - \omega_i) \quad (5.32)$$

$$\begin{bmatrix} L \\ M \\ N \\ T \end{bmatrix} = \xi \begin{bmatrix} L_C \\ M_C \\ N_C \\ T_C \end{bmatrix} + \mathbf{B} \begin{bmatrix} \gamma (\xi \omega_{1,C} - \omega_1) \\ \gamma (\xi \omega_{2,C} - \omega_2) \\ \gamma (\xi \omega_{3,C} - \omega_3) \\ \gamma (\xi \omega_{4,C} - \omega_4) \end{bmatrix} \quad (5.33)$$

In Chapter 3 it was established that the torque vector is $\boldsymbol{\tau} = [L \ M \ N]^T$. Considering that the commanded torques are given by $\boldsymbol{\tau}_C = [L_C \ M_C \ N_C]^T$, then (5.33) can be rewritten as (5.34), where \mathbf{B}' is defined in (5.35)

$$\boldsymbol{\tau} = \xi \boldsymbol{\tau}_C + \mathbf{B}' \begin{bmatrix} \gamma (\xi \omega_{1,C} - \omega_1) \\ \gamma (\xi \omega_{2,C} - \omega_2) \\ \gamma (\xi \omega_{3,C} - \omega_3) \\ \gamma (\xi \omega_{4,C} - \omega_4) \end{bmatrix} = \xi \boldsymbol{\tau}_C + \boldsymbol{\tau}_\xi \quad (5.34)$$

$$\mathbf{B}' = \begin{bmatrix} -l_x k_T & -l_x k_T & l_x k_T & l_x k_T \\ l_x k_T & -l_x k_T & -l_x k_T & l_x k_T \\ -k_N & k_N & -k_N & k_N \end{bmatrix} \quad (5.35)$$

In the analysis for the altitude loop, the equation equivalent to (5.34) is (5.8). To proceed with the analysis in that case, it was considered that the speeds of all motors and their respective commands were equal to ω and ω_C , respectively. This included the cases where the quadrotor either increases, decreases, or maintains its altitude, which corresponds to common use cases. It also allowed a direct relation between the altitude reference signal Z_R and

the altitude error e_Z to be written in (5.20), which is what permits the study of the location of the poles of the linear approximation as the battery voltage changes.

However, the same approach cannot be applied to the attitude loop, since, by looking at the control allocation, it becomes clear that if the motor speeds are equal, all torques in the vector τ are equal to zero. The state equations for the attitude (3.6) and (3.7) show that there is a coupling between the ρ and Ω , which means that it becomes difficult to presume any operating condition that would lead to decoupling them while still allowing an expression similar to that of the altitude case to be written. Therefore, the present analysis will continue by isolating the nonlinear term at each stage, such as the τ_ξ in (5.34). When the simulated and experimental results are presented, a numerical approach will be employed to provide a linear approximation of the attitude dynamics.

The state equation for the vector of the angular accelerations from Chapter 3 is repeated here in (5.36), for added clarity. The expression for the torque vector (5.34) can then be applied to (5.36), resulting in (5.37).

$$\dot{\Omega} = \mathbf{J}^{-1}(-\Omega \times \mathbf{J}\Omega + \tau) \quad (5.36)$$

$$\dot{\Omega} = \xi \mathbf{J}^{-1} \tau_C + \mathbf{J}^{-1} \tau_\xi - \mathbf{J}^{-1}(\Omega \times \mathbf{J}\Omega) \quad (5.37)$$

The NDI control strategy presented in section 3.6 defines the vector of the commanded torques τ_C as (5.38).

$$\tau_C = \mathbf{J}[\mathbf{S}^{-1}(\rho)\nu_\rho - \mathbf{S}^{-1}(\rho)\dot{\mathbf{S}}(\rho, \dot{\rho})\Omega + \mathbf{J}^{-1}(-\Omega \times \mathbf{J}\Omega)] \quad (5.38)$$

Applying (5.38) to (5.37) results in (5.39).

$$\dot{\Omega} = \xi \mathbf{S}^{-1}(\rho)\nu_\rho - \xi \mathbf{S}^{-1}(\rho)\dot{\mathbf{S}}(\rho, \dot{\rho})\Omega + \mathbf{J}^{-1}\tau_\xi + (1 - \xi)\mathbf{J}^{-1}(-\Omega \times \mathbf{J}\Omega) \quad (5.39)$$

Considering that the attitude dynamics $\ddot{\rho}$ are given by (5.41), (5.39) can be applied to (5.41), resulting in (5.43), where $\ddot{\rho}_\xi = \mathbf{S}(\rho)\mathbf{J}^{-1}\tau_\xi + (1 - \xi)(\dot{\mathbf{S}}(\rho, \dot{\rho})\Omega + \mathbf{S}(\rho)\mathbf{J}^{-1}(\Omega \times \mathbf{J}\Omega))$

$$\dot{\rho} = \mathcal{S}(\rho)\Omega \quad (5.40)$$

$$\ddot{\rho} = \dot{\mathcal{S}}(\rho, \dot{\rho})\dot{\Omega} + \mathcal{S}(\rho)\dot{\Omega} \quad (5.41)$$

$$\ddot{\rho} = \xi\nu_\rho + \mathcal{S}(\rho)J^{-1}\tau_\xi + (1 - \xi)(\dot{\mathcal{S}}(\rho, \dot{\rho})\dot{\Omega} + \mathcal{S}(\rho)J^{-1}(\Omega \times J\Omega)) \quad (5.42)$$

$$\ddot{\rho} = \xi\nu_\rho + \ddot{\rho}_\xi \quad (5.43)$$

Applying (5.43) to the expression of the second derivative of the error between the attitude states ρ and the reference model output ρ_R , which is $\ddot{e} = \ddot{\rho}_R - \ddot{\rho}$, and employing the expression for the pseudo-control signal ν_ρ (5.44), the error dynamics can be written as shown in (5.47). The vectors of constants \mathbf{K}_{e_ρ} , $\mathbf{K}_{e_{I\rho}}$, $\mathbf{K}_{\dot{e}_\rho}$, correspond to the proportional, integral and derivative attitude error controller gains, respectively.

$$\nu_\rho = \ddot{\rho}_R + \mathbf{K}_{e_\rho}e_\rho + \mathbf{K}_{e_{I\rho}} \int_0^t e_\rho dt + \mathbf{K}_{\dot{e}_\rho}\dot{e}_\rho \quad (5.44)$$

$$\ddot{e}_\rho = \ddot{\rho}_R - (\xi\nu_\rho + \ddot{\rho}_\xi) \quad (5.45)$$

$$\ddot{e} = -\xi\mathbf{K}_{e_\rho}e_\rho - \xi\mathbf{K}_{e_{I\rho}}e_{I\rho} - \xi\mathbf{K}_{\dot{e}_\rho}\dot{e}_\rho + (1 - \xi)\ddot{\rho}_R - \ddot{\rho}_\xi \quad (5.46)$$

$$\begin{bmatrix} \dot{e}_{I\rho} \\ \dot{e}_\rho \\ \ddot{e}_\rho \end{bmatrix} = \begin{bmatrix} 0_{3 \times 3} & I_{3 \times 3} & 0_{3 \times 3} \\ 0_{3 \times 3} & 0_{3 \times 3} & I_{3 \times 3} \\ -\xi\mathbf{K}_{e_{I\rho}} & -\xi\mathbf{K}_{e_\rho} & -\xi\mathbf{K}_{\dot{e}_\rho} \end{bmatrix} \begin{bmatrix} e_{I\rho} \\ e_\rho \\ \dot{e}_\rho \end{bmatrix} + \begin{bmatrix} 0 \\ 0 \\ 1 - \xi \end{bmatrix} \ddot{\rho}_R + \begin{bmatrix} 0 \\ 0 \\ -1 \end{bmatrix} \ddot{\rho}_\xi \quad (5.47)$$

The characteristic equation associated with the error matrix in (5.47) is given by (5.48). Therefore, the eigenvalues of the system are given by the roots of (5.48). Since $0 < \xi \leq 1$, three distinct cases can be defined. If the battery is at full charge, that is, the voltage source provides a voltage $V_{b,0}$, $\xi = 1$, and the system poles are equal to the system poles specified for the error dynamics by the choice of the error controller gains. When $0 < \xi < 1$, which means that the battery voltage is smaller than the nominal value, the poles get closer to zero and the error dynamics get slower. In the hypothetical case where $\xi = 0$, the poles are 0,

however, this is a purely hypothetical case, as the cut-off voltage v_{cut} is greater than zero and the battery would get damaged and stop working properly before reaching this condition.

$$s^3 + \xi(\mathbf{K}_{\dot{e}_\rho} s^2 + \mathbf{K}_{e_\rho} s + \mathbf{K}_{eI_\rho}) = 0 \quad (5.48)$$

5.3 Compensation of the electrical subsystem effects

The mathematical demonstrations presented in sections 5.1 and 5.2 describe the effect of the electrical subsystem over the altitude and attitude dynamics. More specifically, it was shown that in both cases the dynamic behavior will be slowed down by the discharge of the battery. This fact poses the problem of whether the system designer can, with this knowledge, provide solutions that diminish the negative impact of lower battery voltages over the closed-loop dynamics. Two approaches are proposed to solve this problem: a battery-aware controller design and the adjustment of the generated PWM commands.

5.3.1 Battery-aware controller design

The analysis of the altitude and attitude control loop resulted in equations (5.26) and (5.48). Both expressions show that the system response depends on the battery voltage, but they are also dependent on the choice of the controller gains of the error controller. This fact leads to the following hypothesis: it should be possible to include the battery dynamics as a factor in the controller design such that the effect of the varying battery voltage over the closed-loop dynamics is diminished. The expectation is that this battery-aware controller design approach can make the system less sensitive to variations in the battery voltage.

The adopted control strategy in this work employs a reference model to determine the desired dynamics for a given control loop, either the altitude or attitude. This desired dynamics may be achieved by designing the controller by solving the optimization problem (5.49), which aims to minimize the error between the reference signal y_R and the system output y through the appropriate choice of the error controller gains $\left[K_e^u \quad K_{eI}^u \quad K_{\dot{e}}^u \right]^*$, where ν is the pseudo-control signal and the constants U_1 , U_2 and U_3 define the upper bounds for the

controller gains.

$$\begin{aligned}
\left[K_e^u \quad K_{e_I}^u \quad K_{\dot{e}}^u \right]^* &= \arg \min_{\left[K_e^u \quad K_{e_I}^u \quad K_{\dot{e}}^u \right]} \left(\int_{t_0}^{t_f} \left(e(t) \left[K_e^u \quad K_{e_I}^u \quad K_{\dot{e}}^u \right] \right)^2 dt \right) \\
\text{s.t. } \nu(t) &= \ddot{y}_R + K_e^u e(t) + K_{e_I}^u \int_0^t e(t) dt + K_{\dot{e}}^u \dot{e}(t) \\
e(t) \left[K_e^u \quad K_{e_I}^u \quad K_{\dot{e}}^u \right] &= y_R(t) - y(\nu(t)) \\
0 &\leq K_e^u \leq U_1 \\
0 &\leq K_{e_I}^u \leq U_2 \\
0 &\leq K_{\dot{e}}^u \leq U_3
\end{aligned} \tag{5.49}$$

If the model used to obtain the output signal y in (5.49) does not consider the variation of the battery voltage, either by not implementing a battery model or considering only the ideal case $\xi = 1$, then the design process is battery-unaware. Note that while the optimization problem presented in (5.49) presumes a linear error controller, the problem can easily be rewritten for any other control law that employs constant tuning parameters. Therefore, in this work, the resulting controller from this battery-unaware design process represents a previously adopted control strategy for altitude and attitude control in quadrotor mini drones. This controller will be the standard against which performance will be measured.

By contrast, (5.49) can be rewritten as (5.50), where ξ is considered an explicit factor, and the goal is to minimize a weighted sum of the error for different values of ξ , where w_i are the different weights. The goal, then, is to obtain consistent error dynamics for an interval of values of the battery voltage, resulting in a system that is less affected by these changes.

$$\begin{aligned}
\left[K_e^a \quad K_{e_I}^a \quad K_{\dot{e}}^a \right]^* &= \arg \min_{\left[K_e^a \quad K_{e_I}^a \quad K_{\dot{e}}^a \right]} \left(\sum_{i=1}^M \int_{t_0}^{t_f} w_i \left(e(t, \xi_i) \left[K_e^a \quad K_{e_I}^a \quad K_{\dot{e}}^a \right] \right)^2 dt \right) \\
\text{s.t. } \nu(t, \xi_i) &= \ddot{y}_R + K_e e(t, \xi_i) + K_{e_I} \int_0^t e(t, \xi_i) dt + K_{\dot{e}} \dot{e}(t, \xi_i) \\
e(t, \xi_i) \left[K_e^a \quad K_{e_I}^a \quad K_{\dot{e}}^a \right] &= y_R(t) - y(\nu(t, \xi_i)) \\
0 &\leq K_e^a \leq U_1 \\
0 &\leq K_{e_I}^a \leq U_2 \\
0 &\leq K_{\dot{e}}^a \leq U_3
\end{aligned} \tag{5.50}$$

It is important to note that the relation between the altitude dynamics and the current drained from the battery goes both ways. That is, by changing the control gains to obtain a consistent behavior as the battery discharges, the discharge regime will change accordingly. Therefore, in addition to observing the resulting error dynamics from the battery-aware controller design, it is also necessary to verify how the battery is behaving, as the improvement in performance might come at the cost of faster discharge times.

5.3.2 Compensation of the effect of the battery discharge by adjusting the PWM commands

In the previous sections, it was posed that the duty cycle D_i used to generate the PWM commands sent to the motors is given by (5.51), where the nominal voltage value $v_{b,0}$ is considered.

$$D_i = \frac{1}{k_e v_{b,0}} \left[(k_e^2 + r_a b) \omega_{i,C} + r_a k_N \omega_{i,C}^2 \right] \tag{5.51}$$

If it is assumed that the command generation algorithm has access to a sensor measurement of the battery voltage $v_{b,s}$ during flight, then (5.51) becomes (5.52), where D_i^* is the duty-cycle obtained as a function of $v_{b,s}$.

$$D_i^* = \frac{1}{k_e v_{b,s}} [(k_e^2 + r_a b) \omega_{i,C} + r_a k_N \omega_{i,C}^2] \quad (5.52)$$

Considering the steady-state equation for the motor shown in (5.53), (5.52) can be applied to write (5.54), which can be manipulated to result in (5.56), where $\Xi = v_b/v_{b,s}$, which as a coefficient which measures how close the value of the measured battery voltage $v_{b,s}$ is from the actual battery voltage v_b .

$$0 = k_e D_i^* v_b - (k_e^2 + r_a b) \omega_i - r_a k_N \omega_i^2 \quad (5.53)$$

$$0 = k_e v_b \frac{1}{k_e v_{b,s}} [(k_e^2 + r_a b) \omega_{i,C} + r_a k_N \omega_{i,C}^2] - (k_e^2 + r_a b) \omega_i - r_a k_N \omega_i^2 \quad (5.54)$$

$$\frac{v_b}{v_{b,s}} ((k_e^2 + r_a b) \omega_{i,C} + r_a k_N \omega_{i,C}^2) = (k_e^2 + r_a b) \omega_i + r_a k_N \omega_i^2 \quad (5.55)$$

$$\Xi \omega_{i,C} = \omega_i \quad (5.56)$$

If $v_{b,s}$ is close to v_b , then $\Xi \approx 1$ and (5.56) becomes (5.57).

$$\omega_{i,C} = \omega_i \quad (5.57)$$

Therefore, if the PWM commands sent to the motors are a function of the measured battery voltage as presented in (5.52), and the measured battery voltage $v_{b,s}$ is sufficiently precise, the angular speeds of the motors are expected to be equal to the commanded angular speeds in the steady state. This results in the system poles no longer being dependent upon the battery voltage variation.

This strategy also impacts the current i_b drained from the battery. Considering the expression for the steady-state response of the motor in (5.58), the expression (5.59) gives the

current of the motor i_i as a function of the commanded angular rate $\omega_{i,C}$, since in this case (5.56) is valid. Therefore, the motor current is not dependent on the battery voltage v_b .

$$0 = k_e i_i - b\omega_i - k_N \omega_i^2 \quad (5.58)$$

$$i_i = \frac{b\omega_{i,C} + k_N \omega_{i,C}^2}{k_e} \quad (5.59)$$

However, when considering the expression for the duty-cycle as a function of $v_{b,s}$ as in (5.52), it is clear that as $v_{b,s}$ decreases, the value of D_i^* increases. Then, if $v_{b,s} < v_{b,0}$, which will happen as soon as the vehicle is powered on, then the duty-cycle D_i^* will be greater than D_i , where only the nominal battery voltage $v_{b,0}$ is considered. The expression for the current drawn from the battery i_b as a function of i_i and the duty-cycle is (5.60), from which (5.61) is obtained. Thus, using this method to make the system less sensitive to variations in the battery voltage will present a trade-off in the form of a higher current being drawn from the battery, and consequently a faster discharge.

$$i_b \approx \sum_{i=1}^4 D_i^* i_i > \sum_{i=1}^4 D_i i_i \quad (5.60)$$

$$i_b \approx \sum_{i=1}^4 \frac{[(k_e^2 + r_a b) \omega_{i,C} + r_a k_N \omega_{i,C}^2] (b\omega_{i,C} + k_N \omega_{i,C}^2)}{k_e^2 v_b} > \sum_{i=1}^4 \frac{[(k_e^2 + r_a b) \omega_{i,C} + r_a k_N \omega_{i,C}^2] (b\omega_{i,C} + k_N \omega_{i,C}^2)}{k_e^2 v_{b,0}} \quad (5.61)$$

5.4 Impact of the controller choice over the battery discharge

The discussion up to this point analyzed the effect that the varying battery voltage has over the closed loop altitude and attitude responses of a quadrotor mini drone. However, as the system is in a closed loop, the specified dynamics, which are defined by the designer such that the vehicle can perform a given mission, will necessarily have an effect on the battery discharge.

This point can be demonstrated by analyzing the factors that impact energy consumption on a quadrotor. In [Gandolfo et al. 2017] the authors establish that the two most important components of the energy spent in this type of vehicle during normal operation come from two efforts: maintaining or increasing its altitude by generating lift and compensating against drag forces caused by the air when moving laterally. Of these two, the consumption from drag forces is only relevant for vehicles that are large in size, due to the high volume of air their propellers must displace to move, or when moving at very high speeds. As the focus of this study is not specific to either of these conditions, the effort to maintain or increase altitude will be considered the main contributor to energy consumption.

The defining characteristic of rotary wing flying vehicles such as quadrotors from a usability point of view is their ability to perform a hovering flight, that is, to remain at a constant altitude and in a fixed position on the horizontal plane. This condition is illustrated in Fig. 5.1 (a), where a quadrotor is shown with all of its axis aligned to the reference frame. Thus no moments are generated which would lead to angular movement, and if the thrust $T = mg$, the altitude will remain constant.

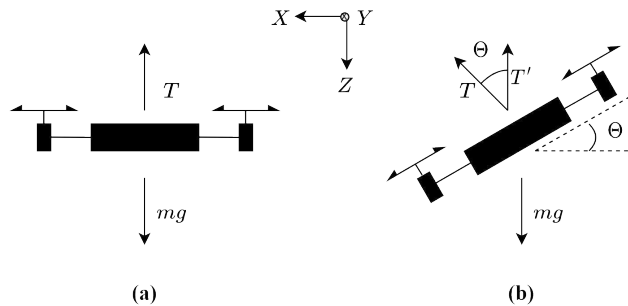


Figure 5.1: Illustration of a quadrotor during hover (a) and while tilting around the Y axis (b).

From an energy consumption standpoint, the current drawn from the battery remains constant in (a), such that the hover condition can be maintained. Consider, then, the cases where the quadrotor performs lateral movement by tilting around the Y axis, shown in Fig. 5.1 (b), where a pitch angle Θ is commanded such that the vehicle might move along the X axis. This leads to the thrust T being tilted by the same angle, resulting in only the component $T_Z = T \cos \Theta$ of the thrust opposing the action of gravity. The torque necessary to produce Θ is achieved by inducing a difference in the speed of the relevant motors. If the goal is for

the vehicle to not lose altitude at the same time it is moving in a given horizontal direction, meaning that $T_z = mg$, then T must increase, and so do the motor speeds. Therefore as long as the vehicle is performing lateral movement, the battery will discharge faster than while hovering.

It follows, then, that the battery will discharge slower the longer the vehicle spends hovering. This leads to the following hypothesis when designing the attitude controller: if multiple control solutions are capable of attending to the necessities of a given task, fast, or aggressive controllers, will lead to a slower discharge of the battery than comparatively slow controllers, as the required attitude maneuvers will be achieved faster and therefore the time spent hovering will be greater. This can be tested by implementing different attitude control strategies and evaluating the resulting energy consumption when performing the same flight mission.

Chapter 6

Compensation of the effects of the electrical subsystem

In this chapter, the results of the analysis and compensation techniques proposed in the previous chapter are verified through simulations and experiments. The employed methods and materials are described, including details about the experimental and simulation platform, the Parrot Mambo, how the altitude and attitude controllers were designed and what experiments and simulations were conducted. Then, results are presented that show the effect of the battery discharge over the poles and how effective the proposed compensation techniques are, along with the impact of the aggressiveness of the attitude controller over the energy consumption.

6.1 Methods and materials

The details about the simulation and experimental platforms employed to obtain the results are presented in this section. Additionally, the optimization problems employed to obtain the controller gains for the altitude and attitude loops are also defined and the test maneuvers employed are described.

6.1.1 Parrot Mambo

For the flight simulations and experiments presented in the next section, the platform used is the Parrot Mambo. This platform has seen previous use in research, in works such as [Madruga et al. 2022] and [Scola et al. 2021]. It is an "x" configuration quadrotor mini drone powered by a LiPo battery, capable of both autonomous and remotely controlled flight. The sensors available are an Inertial Measurement Unit (IMU), which contains an accelerometer and a gyroscope, a barometer, a downwards-facing ultrasound distance sensor, and a downwards-facing camera. This set of sensors is capable of tracking its global position through the use of an optical flow algorithm and subsequent fusion of sensor data.

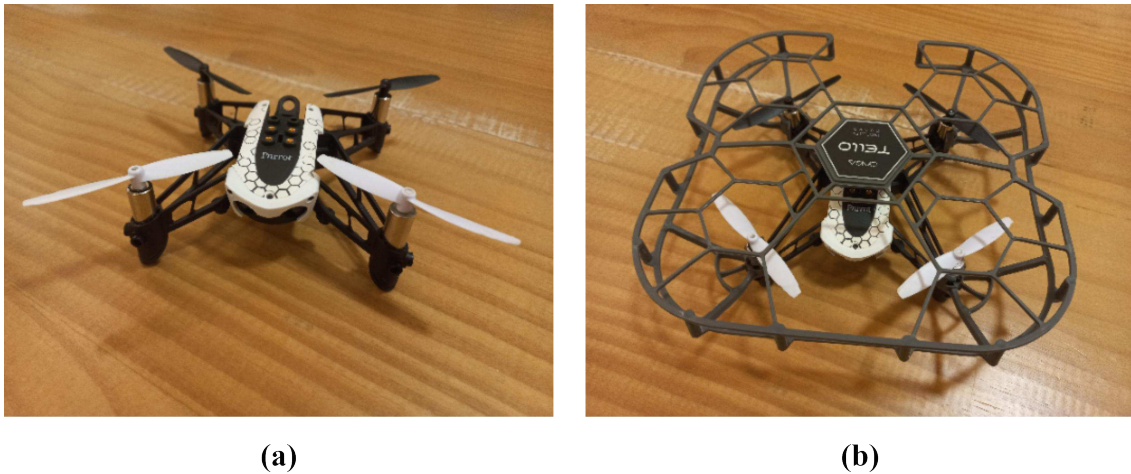


Figure 6.1: Photos of the Parrot Mambo without (a) and with (b) a flexible protection cage.

The Parrot Mambo has a supported simulation package for Simulink, which enable the use of model-in-the-loop and hardware-in-the-loop verification approaches. The block diagram of the simulation environment can be seen in Fig. 6.2. The model has a Flight Control System (FCS) block, which contains the command generation, the state estimator, and the state controllers, shown in Fig. 6.3. The electrical subsystem is shown in Fig. 6.4, containing models of the motors and battery. The simulator also includes aerodynamic and environmental effects and provides models for the embedded sensors. Flight controller code can be generated and deployed directly to the vehicle through a Bluetooth Low Energy (BLE) connection, from which flight data and logs can be collected. A 3D visualization of the vehicle is available during simulations and is presented in Fig. 6.5.

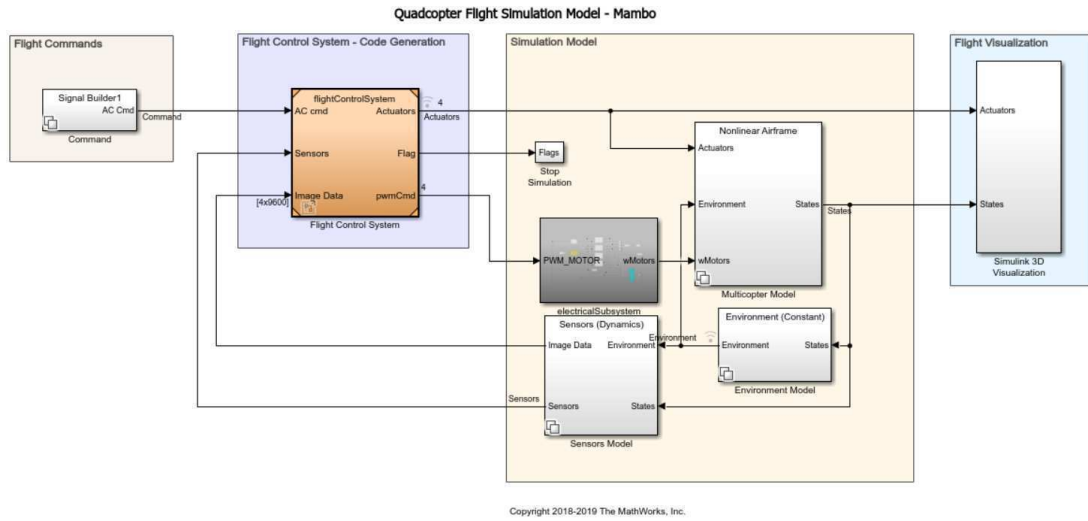


Figure 6.2: Simulink block diagram model of the Parrot Mambo.

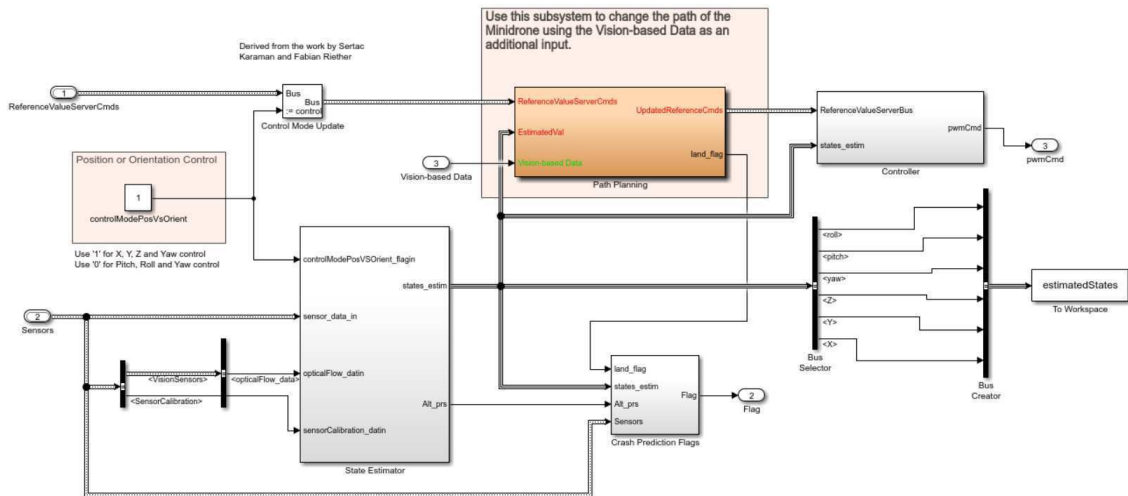


Figure 6.3: Simulink model of the Flight Control System of the Parrot Mambo.

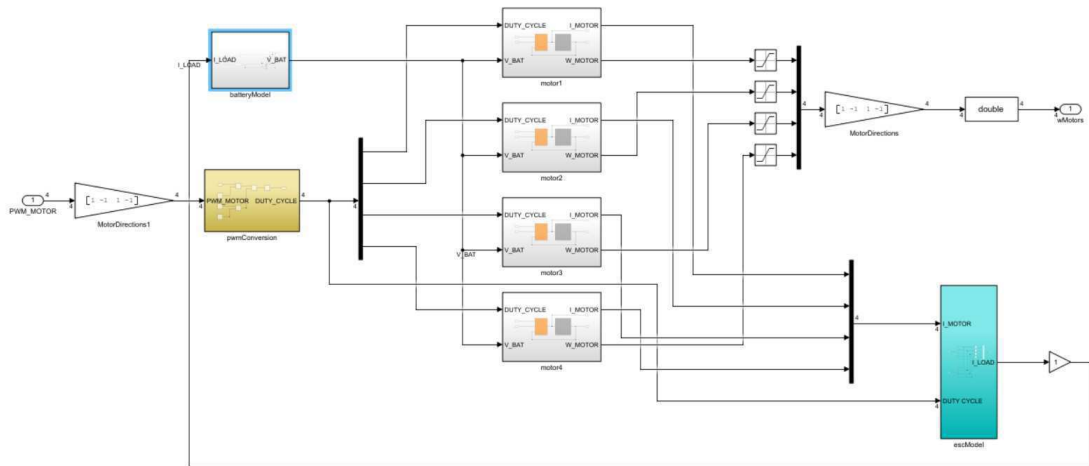


Figure 6.4: Simulink model of the electrical subsystem of the Parrot Mambo.

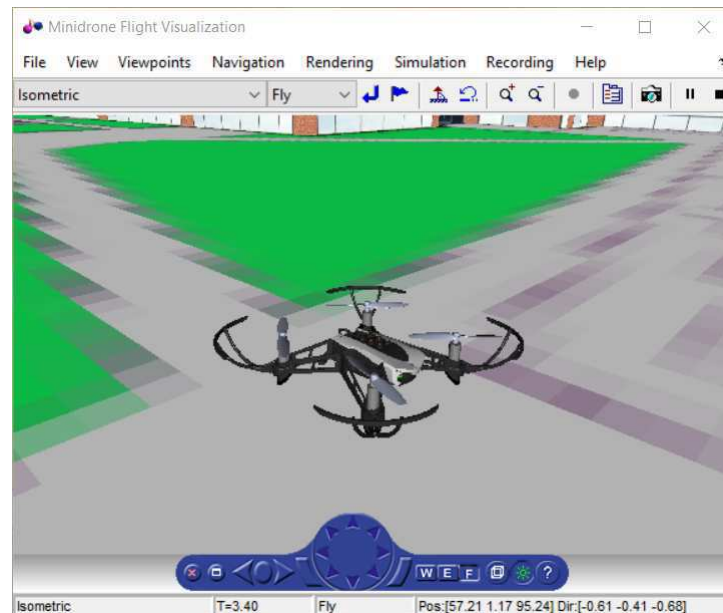


Figure 6.5: 3D visualization of the Parrot Mambo during flight in the simulated environment.

It is relevant to note that the simulator architecture shown in Fig. 6.2 can be directly translated to the block diagram of the integrated model for a quadrotor mini drone shown in Fig. 3.12, with the exception of the environmental model, which in this case was kept constant as all tests were performed indoors. Further details regarding the platform can be found in [Mathworks 2020].

The simulation environment employs the Parrot Mambo parameters listed in Table 6.1, using a sampling time of $t_s = 0.005$ s. The vehicle was powered by the GiFi Power battery whose model is presented in Section 4.5.4.

$\mathbf{J} = \text{diag}(0.0005 \text{ kg m}^2, 0.0007 \text{ kg m}^2, 0.0001 \text{ kg m}^2)$			
m	0.063 kg	r_a	0.49 Ω
k_e	7.4041×10^{-4} Nm/A	b	10^{-6} Nms/rad
k_N	9.6223×10^{-11} kgm ² /rad	J^P	4.5156×10^{-8} kgm ²
l	0.062 m	k_T	7.4041×10^{-4} kgm
r_S	0.13 Ω		

Table 6.1: Parrot Mambo parameters.

The duty cycle defined in (5.51) and (5.52) is converted to a signal within a range of values defined by the hardware, such that the digital-to-analog converters can provide the voltage level corresponding to the desired motor angular velocity. In the case of the Parrot Mambo, this signal for a motor i is $\omega_{i,PWM} \in [10, 500]$. The upper and lower bounds for the commanded PWM signal are imposed by the hardware, which in this case is the Parrot Mambo. The values smaller than 10 are reserved for special cases, such as flight crashes. The signal $\omega_{i,PWM}$ can be obtained from D_i using (6.1).

$$\omega_{i,PWM} = 490D_i + 10 \quad (6.1)$$

6.1.2 Numerical linearization of the attitude control loop

In the analysis of the attitude dynamics presented in Chapter 5 it was established that a numerical approach would be implemented in order to obtain a linear approximation of the system so that the behavior of the closed-loop poles as the battery discharges might be analyzed. This was done through the Model Linearizer feature available in Simulink. This feature allows defining inputs and outputs in a Simulink model and obtaining linear approximations between them. The model shown in Fig. 6.6 was used when linearizing the attitude dynamics. In this block diagram, the pink block is the reference dynamics model and the blue block is the closed-loop attitude dynamics. This is a version of the full model of the

Parrot Mambo, employing the same physical constants, but omitting blocks related to image processing and the 3D visualization which generate the need to calculate very large Jacobians, exceeding the available computer memory. The result of the linearization considering a varying power source is a set of state space models, from which a transfer function and closed loop poles can be obtained.

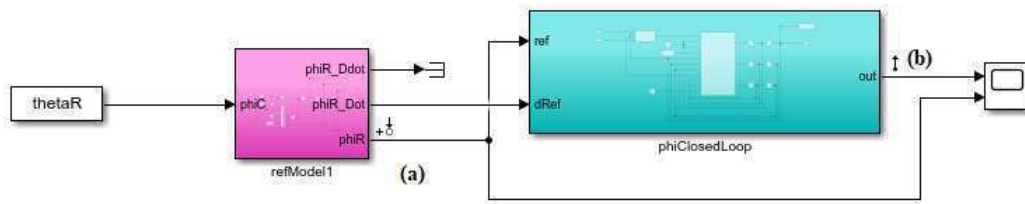


Figure 6.6: Model employed for the numerical linearization. The input is (a) and the output is (b).

6.1.3 Controller design for the altitude control loop

The gains of the battery-unaware altitude error controller $\begin{bmatrix} \hat{K}_{e_z}^u & \hat{K}_{e_{Iz}}^u & \hat{K}_{\dot{e}_z}^u \end{bmatrix}$ are obtained by solving the optimization problem (6.2), which aims to minimize the error over the time interval $[t_0, t_f]$, according to what was proposed in section 5.3. The nonlinear altitude dynamics can be obtained from the models described in Chapters 3 and 4, and from the analysis presented in section 5.1. The constant U_u^Z is the upper bound for the controller gains. Since this is the battery-unaware case, $\xi = 1$ was considered, that is, the design of the controller was unaware of the changes in the energy source during the flight.

$$\begin{aligned}
\left[\hat{K}_{eZ}^u \quad \hat{K}_{eIZ}^u \quad \hat{K}_{\dot{e}Z}^u \right]^* &= \arg \min_{\left[K_{eZ}^u \quad K_{eIZ}^u \quad K_{\dot{e}Z}^u \right]} \left(\int_{t_0}^{t_f} \left(e_Z(t) \left[K_{eZ}^u \quad K_{eIZ}^u \quad K_{\dot{e}Z}^u \right] \right)^2 dt \right) \\
\text{s.t. } \nu_Z(t) &= \ddot{Z}_R + K_{eZ} e_Z(t) + K_{eIZ} \int_0^t e_Z(t) dt + K_{\dot{e}Z} \dot{e}_Z(t) \\
e_Z(t) \left[K_{eZ}^u \quad K_{eIZ}^u \quad K_{\dot{e}Z}^u \right] &= Z_R(t) - Z(\nu_Z(t)) \\
0 &\leq K_{eZ}^u \leq U_u^Z \\
0 &\leq K_{eIZ}^u \leq U_u^Z \\
0 &\leq K_{\dot{e}Z}^u \leq U_u^Z
\end{aligned} \tag{6.2}$$

The gains of the battery-aware altitude error controller $\left[\hat{K}_{eZ}^a \quad \hat{K}_{eIZ}^a \quad \hat{K}_{\dot{e}Z}^a \right]$ are obtained by simulating the altitude response for the $\xi \in \{\xi_1, \dots, \xi_n\}$, for a total of M_ξ values of ξ . The weighted sum of the resulting errors over a time interval $[t_0, t_f]$ is then minimized. The corresponding optimization problem is shown in (6.3), where w_i is the weight for a given error $e_Z^{\xi_i}$ and U_a^Z is the upper bound for the controller gains.

$$\begin{aligned}
\left[\hat{K}_{eZ}^a \quad \hat{K}_{eIZ}^a \quad \hat{K}_{\dot{e}Z}^a \right] &= \arg \min_{\left[K_{eZ}^a \quad K_{eIZ}^a \quad K_{\dot{e}Z}^a \right]} \left(\sum_{i=0}^{M_\xi} \int_{t_0}^{t_f} w_i \left(e_Z(t, \xi_i) \left[K_{eZ}^a \quad K_{eIZ}^a \quad K_{\dot{e}Z}^a \right] \right)^2 dt \right) \\
\text{s.t. } \nu_Z(t, \xi_i) &= \ddot{Z}_R + K_{eZ} e_Z^{\xi_i}(t, \xi_i) + K_{eIZ} \int_0^t e_Z(t, \xi_i) dt + K_{\dot{e}Z} \dot{e}_Z(t, \xi_i) \\
e_Z(t, \xi_i) \left[K_{eZ}^a \quad K_{eIZ}^a \quad K_{\dot{e}Z}^a \right] &= Z_R(t) - Z(\nu_Z(t, \xi_i)) \\
0 &\leq K_{eZ}^a \leq U_a^Z \\
0 &\leq K_{eIZ}^a \leq U_a^Z \\
0 &\leq K_{\dot{e}Z}^a \leq U_a^Z
\end{aligned} \tag{6.3}$$

Since the problems defined in (6.2) and (6.3) are nonlinear constrained problems, a PSO optimization method was chosen to solve them, as this approach is able to avoid local minima. The Matlab Optimization toolbox implementation was used, which is based on [Kennedy & Eberhart 1995]. The initial swarm has 100 particles with a uniform distribution, and the stop tolerance was set to 10^{-6} . The maximum number of stall iterations is 20, the

adaptive inertia range is $[0.1, 1]$ and the maximum number of iterations is $200 n_{vars} = 600$.

In both (6.2) and (6.3) the objective functions to be minimized are based on the error between a provided reference signal and the system output. Therefore, providing the optimization is properly solved, it is expected that the resulting controller gains will lead to a dynamic behavior close to that of the reference signal. This means that the choice of the reference model parameters which generate Z_R , in the case of the altitude loop, will determine the expected system dynamics.

6.1.4 Controller design for the attitude control loop

The formulation of the optimization problems to design the controller for the attitude control loop is analogous to that of the altitude controller. The same optimization algorithm and optimization settings were employed, with the gains of the battery-unaware attitude error controller $\begin{bmatrix} \hat{K}_{e_\rho}^u & \hat{K}_{e_{I\rho}}^u & \hat{K}_{\dot{e}_\rho}^u \end{bmatrix}$ being obtained by solving (6.4), where the ideal case $\xi = 1$ is considered, and the gains of the battery-aware attitude error controller $\begin{bmatrix} \hat{K}_{e_\rho}^a & \hat{K}_{e_{I\rho}}^a & \hat{K}_{\dot{e}_\rho}^a \end{bmatrix}$ being obtained by solving (6.5), in which multiple values of ξ are considered. The nonlinear attitude dynamics are obtained from the models described in Chapters 3 and 4 and from the analysis shown in 5.2. The constants U_u^ρ and U_a^ρ are the upper bounds for the gains of the battery-unaware and the battery-aware attitude error controllers, respectively. Once again, due to the nature of the optimization, the system behavior will be defined by the choice of the reference model which provides the reference attitude signals ρ_R .

$$\begin{aligned}
\begin{bmatrix} \hat{K}_{e_\rho}^u & \hat{K}_{e_{I\rho}}^u & \hat{K}_{\dot{e}_\rho}^u \end{bmatrix} &= \arg \min_{\begin{bmatrix} K_{e_\rho}^u & K_{e_{I\rho}}^u & K_{\dot{e}_\rho}^u \end{bmatrix}} \left(\int_{t_0}^{t_f} \left(e_\rho(t) \begin{bmatrix} K_{e_\rho}^u & K_{e_{I\rho}}^u & K_{\dot{e}_\rho}^u \end{bmatrix} \right)^2 dt \right) \\
\text{s.t. } \nu_\rho(t) &= \ddot{\rho}_R + K_{e_\rho} e_\rho(t) + K_{e_{I\rho}} \int_0^t e_\rho(t) dt + K_{\dot{e}_\rho} \dot{e}_\rho(t) \\
e_\rho(t) \begin{bmatrix} K_{e_\rho}^u & K_{e_{I\rho}}^u & K_{\dot{e}_\rho}^u \end{bmatrix} &= \rho_R(t) - \rho(\nu_\rho(t)) \\
0 \leq K_{e_\rho}^u &\leq U_u^\rho \\
0 \leq K_{e_{I\rho}}^u &\leq U_u^\rho \\
0 \leq K_{\dot{e}_\rho}^u &\leq U_u^\rho
\end{aligned} \tag{6.4}$$

$$\begin{aligned}
\begin{bmatrix} \hat{K}_{e_\rho}^a & \hat{K}_{e_{I\rho}}^a & \hat{K}_{\dot{e}_\rho}^a \end{bmatrix} &= \arg \min_{\begin{bmatrix} K_{e_\rho}^a & K_{e_{I\rho}}^a & K_{\dot{e}_\rho}^a \end{bmatrix}} \left(\sum_{i=0}^{M_\xi} \int_{t_0}^{t_f} w_i \left(e_\rho(t, \xi_i) \begin{bmatrix} K_{e_\rho}^a & K_{e_{I\rho}}^a & K_{\dot{e}_\rho}^a \end{bmatrix} \right)^2 dt \right) \\
\text{s.t. } \nu_\rho(t, \xi_i) &= \ddot{\rho}_R + K_{e_\rho} e_\rho(t, \xi_i) + K_{e_{I\rho}} \int_0^t e_\rho(t, \xi_i) dt + K_{\dot{e}_\rho} \dot{e}_\rho(t, \xi_i) \\
e_\rho(t, \xi_i) \begin{bmatrix} K_{e_\rho}^a & K_{e_{I\rho}}^a & K_{\dot{e}_\rho}^a \end{bmatrix} &= \rho_R(t) - \rho(\nu_\rho(t, \xi_i)) \\
0 \leq K_{e_\rho}^a &\leq U_a^\rho \\
0 \leq K_{e_{I\rho}}^a &\leq U_a^\rho \\
0 \leq K_{\dot{e}_\rho}^a &\leq U_a^\rho
\end{aligned} \tag{6.5}$$

6.1.5 Description of the altitude control loop simulation and experiments

The altitude maneuver shown in Fig. (6.7) was used as the altitude reference. In the maneuver, the vehicle takes off and remains hovering, with no lateral movement, for 5 s and 1.1 m. Then, it performs three consecutive 0.4 m ascents, hovering at 1.5 m for 7.5 s, before descending to 1.1 m again. The first 5 s of the maneuver corresponds to the take-off regime, which has a mandatory firmware start-up sequence, which involves sending commands to the motors such that inertia is overcome. Therefore, the data in the time interval $t \in [0\text{s}, 5\text{s}]$ will not be considered. This altitude maneuver was designed to provide a significant effect on the battery voltage while remaining in an operation region where the Parrot Mambo altitude tracking is reliable. At very low altitude values, aerodynamic effects from the air displaced by the propellers might impact the system stability, while for much higher altitudes the optical flow based position tracking is unreliable.

In the simulated case, the maneuver was performed for different values of ξ . The simulated results were employed to solve the optimization problems shown in (6.2) and (6.3). In both the simulated and experimental environments, altitude reference model dynamics was determined by a fundamental frequency of $\omega_Z = 5$ and a damping coefficient of $\zeta_Z = 1$, unless otherwise specified. These values were empirically obtained by performing flight tests and observing the resulting vehicle behavior. Images of the vehicle during the flight are

shown in Fig. 6.8.

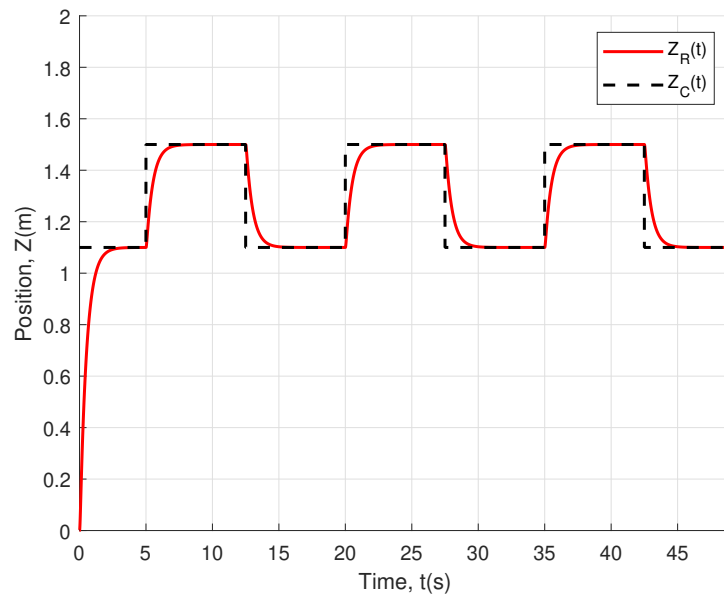


Figure 6.7: Reference altitude maneuver.



Figure 6.8: Photos of the Parrot Mambo performing the maneuver shown in Fig. 6.7, at 1.1 m (a) and 1.5 m (b).

6.1.6 Description of the attitude control loop simulation and experiments

When designing attitude test scenarios, real-world restrictions must be taken into account. So as to have a reasonable degree of control over environmental variables, the flight experiments must be performed indoors, otherwise, factors such as the wind could introduce a disturbance not predicted in the models. This would affect the analysis of the impact of the effect of the drop in the battery voltage over the altitude and attitude dynamics. One must consider, then, the fact that small variations in the quadrotor attitude will quickly translate into a considerable distance traveled in the horizontal plane, which is a relevant restriction for indoor environments.

The signal used as the attitude reference is shown in Fig. 6.9, which equates to the vehicle moving forward 1.5m and then returning to the original point. This corresponds to sharp variations in the pitch angle of 4° , with the initial variation being smaller due to the absence of a backward momentum that must be compensated. The altitude is kept constant at 1.1 m. This maneuver avoids physical shocks against walls and other obstacles in the indoor test environment while sufficiently exciting the attitude dynamics. As in the altitude maneuver, the first 5 s are considered to be part of the take-off. This maneuver was used both in simulated and experimental scenarios, and the results from the simulated case were used to obtain the controller gains from (6.4) and (6.5). Images of the vehicle during flight are shown in Fig. 6.10.

The attitude dynamics reference model has a fundamental frequency of $\omega_\rho = 100$ and a damping coefficient of $\zeta_\rho = 1$ unless otherwise specified. These values were defined empirically through the observation of flight test results. Fast reference dynamics need to be imposed in this case, as generally, the attitude loop is the inner loop of the position control loop, and therefore the use of slower reference dynamics would lead to a degradation of the system performance.

In the case of the attitude loop, the relevant state variables are the angles Φ , Θ , and Ψ . The yaw angle Ψ tracking is treated separately from the other two, as it pertains to the rotational position of the vehicle and does not have influence in either the lateral or the vertical movements. As such, the relevant states are the roll and pitch angles, which are

symmetrical to one another along their respective axis. Therefore, to avoid the repetitive presentation of results which would lead to the same conclusions, a preference will be given to presenting results for the pitch angle Θ .

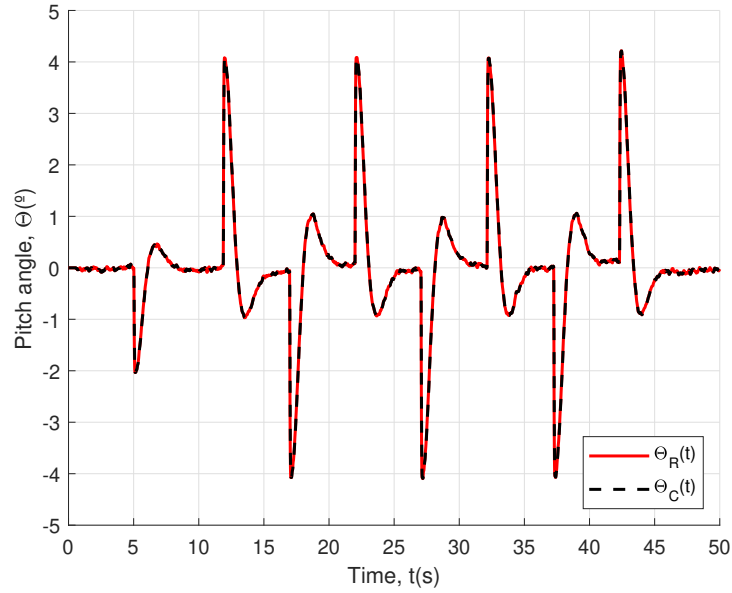


Figure 6.9: Reference attitude maneuver.



Figure 6.10: Photos of the Parrot Mambo performing the maneuver shown in Fig. 6.9, at the initial position (a) and 1.5 m forward (b).

6.1.7 Description of the trajectory simulation and experiments

To evaluate the impact of the choice of aggressiveness of the attitude controller over the energy consumption, an experiment in which the quadrotor mini drone performs a square trajectory was devised, reflecting a common-use scenario. The aforementioned trajectory can be seen in Fig. 6.11, made of a square with 1.5 m in the side. The vehicle must take off from the ground, remain at a stable altitude of 1 m, and then move sequentially to the square vertices in a counter-clockwise order, until the specified flight time of 50 s is achieved. As with the altitude and attitude experiments, the data corresponding to the take-off will not be considered when evaluating the results.

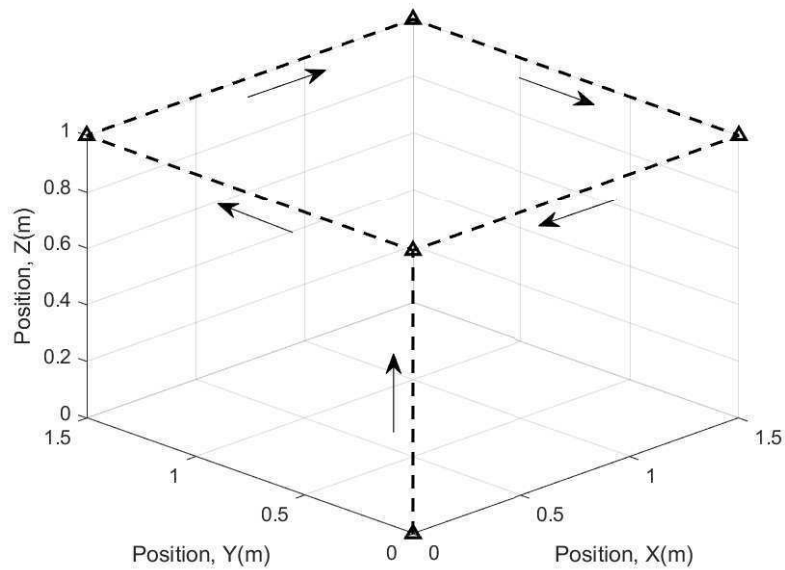


Figure 6.11: Reference trajectory used in the experiments.

6.2 Simulated location of the closed-loop poles and system response as the battery voltage drops

6.2.1 Altitude control loop

The gains of the battery-unaware altitude controller were obtained by solving (6.2) for $U_u^Z = 10$, $t_0 = 0s$ and $t_f = 5s$, resulting in $\left[\hat{K}_{eZ}^u \quad \hat{K}_{eIZ}^u \quad \hat{K}_{\dot{e}Z}^u \right] = \left[0.95 \quad 0.25 \quad 0.54 \right]$. The value of the upper bound was chosen to avoid saturation in the vehicle actuators and the time interval corresponds to the duration of the transient response of the employed command step signal. A simulation of the pole placement of the linearized system when employing the battery-unaware controller was conducted while varying the value of ξ from 0.8 to 1, in increments of 0.01, resulting in Fig. 6.12, where it can be seen that the dominant real pole remains at approximately the same position as ξ varies from 1 to 0.8, but the pair of complex poles gets closer to the origin. That is, the system response gets slower. A color bar is included in this figure, with red corresponding to the lower ξ values and blue to the higher ones.

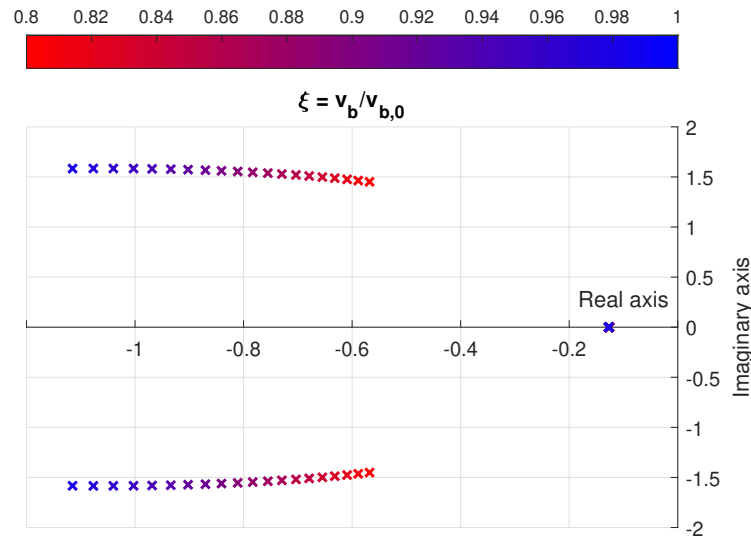


Figure 6.12: Altitude system poles for the linear approximation of the altitude control loop, designed with a battery-unaware controller.

Fig. 6.13 shows the error transient response of the altitude closed-loop poles for the linear approximation as ξ varies, using the battery-unaware controller parameters. There are three undesired phenomena that must be addressed. First, system response gets slower as ξ

decreases, corroborating the analysis of the closed-loop poles of the linear approximation. Secondly, the response dynamics change, with the appearance of oscillations and a longer settling time when comparing the lower ξ values to the higher ones. Finally, the peak error value suffers a significant increase. Not considering the ideal case $\xi = 1$, in which the NDI leads to a perfect tracking of the reference signal, the peak error goes from around 0.02 m in the higher ξ values to 0.14 m in the lower ξ values. Furthermore, the integral action from the nonlinear dynamic inversion is dependent on model parameter knowledge, which means that even the steady-state behavior can be affected in an experimental scenario, a fact that will be shown in the experimental results.

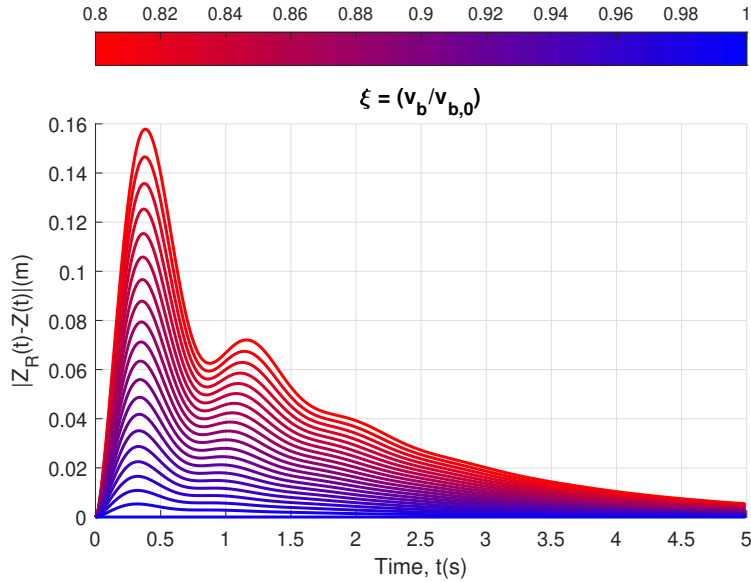


Figure 6.13: Simulated altitude error transient response using battery-unaware controller design.

6.2.2 Attitude control loop

The battery-unaware attitude controller gains were obtained by solving (6.4) for $U_u^p = 1$, $t_0 = 0s$ and $t_f = 50s$, resulting in $\begin{bmatrix} \hat{K}_{e_p}^u & \hat{K}_{e_{I_p}}^u & \hat{K}_{\dot{e}_p}^u \end{bmatrix} = \begin{bmatrix} 0.95 & 0.07 & 0.12 \end{bmatrix}$. The value of the upper bound was chosen to avoid saturation in the vehicle actuators and the time interval corresponds to the duration of the employed reference signal. The poles of the numerically linearized system were then obtained by varying the value of ξ between 0.8 and 1, resulting

in Fig. 6.14, where it can be seen that the dominant real pole remains at approximately at the same position, while the leftmost real pole gets closer to the origin as ξ goes from 1 to 0.8. This corroborates the findings from the mathematical analysis, as the drop in battery voltage leads to a slower system response.

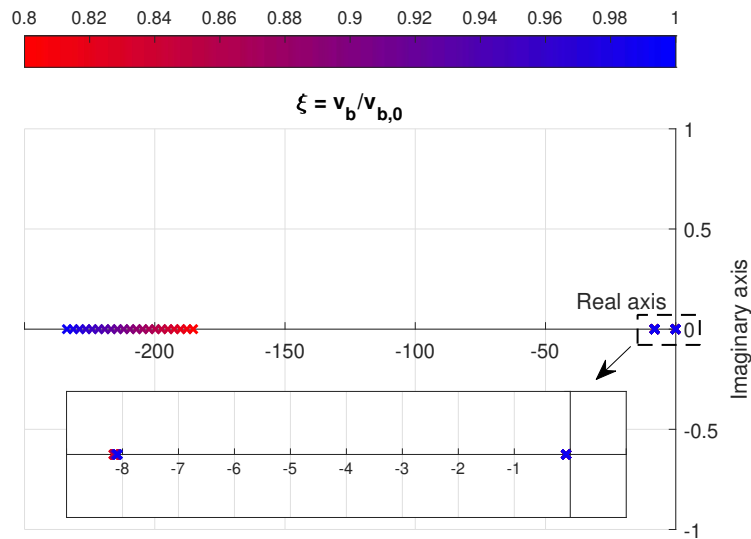


Figure 6.14: Attitude system poles for the linear approximation of the attitude control loop, designed with a battery-unaware controller.

However, when looking at the resulting error dynamics, shown in Fig. 6.15, the resulting variation, although present, is relatively small. Remembering that, for this case, the altitude dynamics correspond to the most energetically costly component of the vehicle operation, it follows that the effect of the battery discharge over the attitude dynamics would be significantly smaller than the one observed for the altitude.

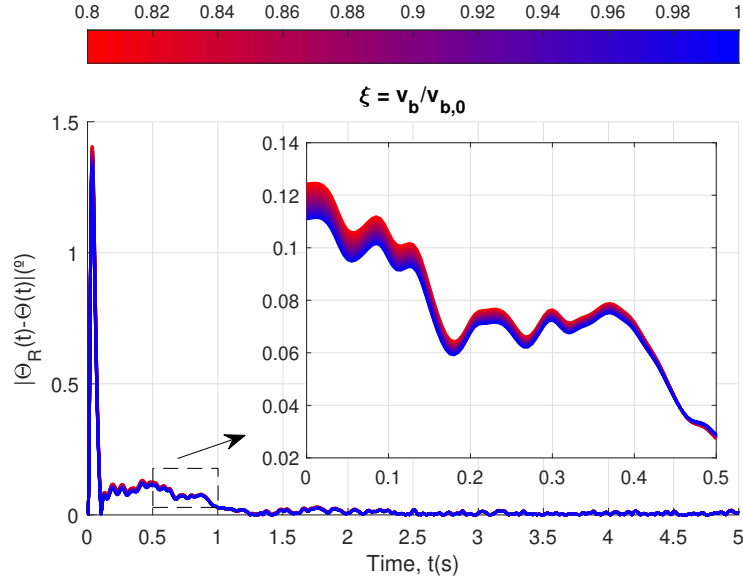


Figure 6.15: Simulated attitude error transient response using battery-unaware controller design.

6.3 Battery-aware controller design simulated results

6.3.1 Altitude control loop

The gains of the battery-aware altitude controller were obtained by solving (6.3) for $U_a^Z = 10$, $t_0 = 0$ s, $t_f = 5$ s and values of ξ_i going from 0.8 to 1 in increments of 0.01, for $M = 21$ with all weights $w_1 = \dots = w_M = 1$, as the objective is for the performance to be consistent across all considered values of ξ , resulting in $\begin{bmatrix} \hat{K}_{e_Z}^a & \hat{K}_{e_{TZ}}^a & \hat{K}_{e_Z}^a \end{bmatrix} = \begin{bmatrix} 5.03 & 7.87 & 1.36 \end{bmatrix}$. The results for the battery-aware altitude controller in the simulated case can be seen in Figs. 6.16 and 6.17, where it is shown that by designing the controller taking the battery voltage as a factor, the difference in behavior for the $\xi \approx 1$ scenarios against the $\xi \approx 0.8$ ones is greatly reduced, along with an overall improvement in the peak value of the error dynamics. The peak error for the battery-unaware design varies between 0 and 0.16 for the different values of ξ , while it stays between 0 and 0.04 for the battery-aware case. The dominant pole is allocated further to the left, so that as the battery discharges and the dynamics get slower, the closed-loop behavior is still acceptable, especially when considering the steady-state response.

Furthermore, the imposition of different closed-loop dynamics will necessarily impact the discharge rate of the battery. In the experimental section, a comparison of the battery voltage between the battery-unaware and battery-aware cases will be performed to determine if there is a trade-off between the two controller design approaches.

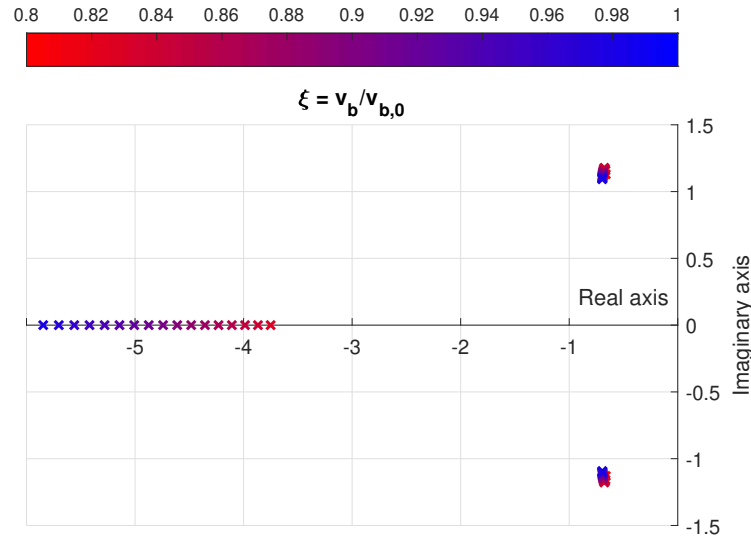


Figure 6.16: Altitude system poles for the linear approximation of the altitude control loop, designed with a battery-aware controller.

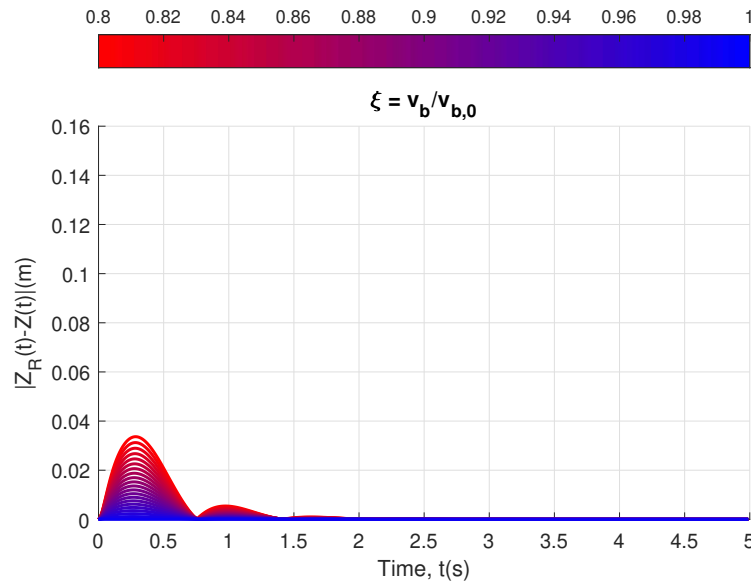


Figure 6.17: Simulated altitude error transient response using battery-aware controller design.

6.3.2 Attitude control loop

The gains of the battery-aware attitude controller were obtained by solving (6.5) for $U_a^p = 0.1$, $t_0 = 0$ s, $t_f = 50$ s and values of ξ_i going from 0.8 to 1 in increments of 0.01, for $M = 21$ with all weights $w_1 = \dots = w_M = 1$, as the objective is for the performance to be consistent across all considered values of ξ , resulting in $[\hat{K}_{e_p}^a \quad \hat{K}_{e_{I\rho}}^a \quad \hat{K}_{\dot{e}_p}^a] = [0.99 \quad 0.07 \quad 0.25]$. The resulting error dynamics for the battery-aware attitude controller can be seen in Fig. 6.18. There is not a significant improvement over the behavior observed in Fig. 6.15, which is coherent since as the battery-unaware case established that this loop is not severely impacted by the battery discharged, the gains from the battery-aware design are only marginal. The corresponding poles from the linear approximation are shown in Fig. 6.19.

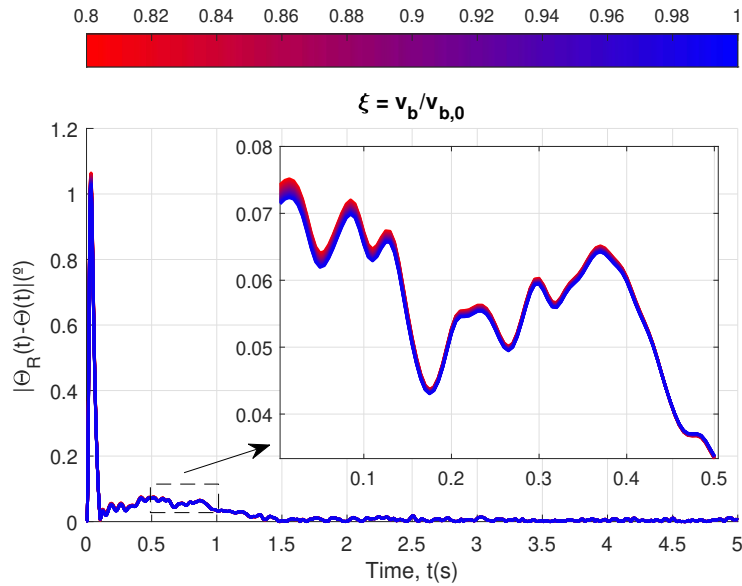


Figure 6.18: Simulated attitude error transient response using battery-aware controller design.

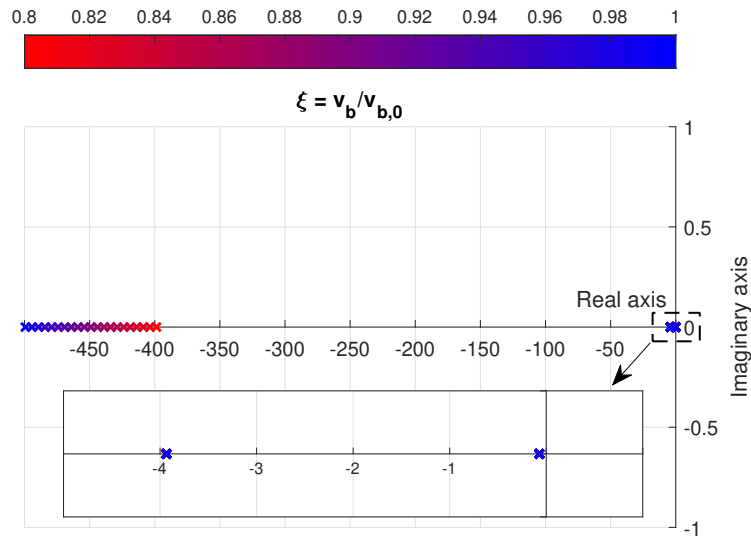


Figure 6.19: Attitude system poles for the linear approximation of the altitude control loop, designed with a battery-aware controller.

6.4 Adjusted command compensation simulated results

This section presents the simulated results comparing the altitude response of the quadrotor mini drone when performing the maneuver shown in Fig. 6.7 between the cases where the motor commands are obtained through the nominal battery voltage or normal commands, using (5.51), and when the measured battery voltage is fed into the command generation process or compensated commands, using (5.52). The battery-aware controller is being used, as it presented a better error transient response in both the altitude and attitude control loops when compared to the battery-unaware alternative. The absolute error for each case is shown in Fig. 6.20, with the signals from 27.5 until 32.5 s being highlighted in Fig. 6.21, and the corresponding battery voltages are shown in Fig. 6.22.

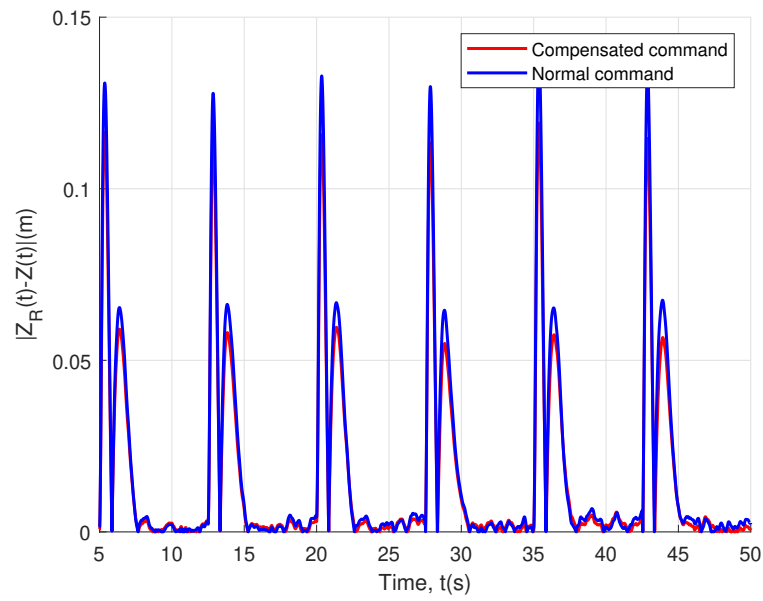


Figure 6.20: Simulated altitude error transient response for the non-compensated and compensated command generation.

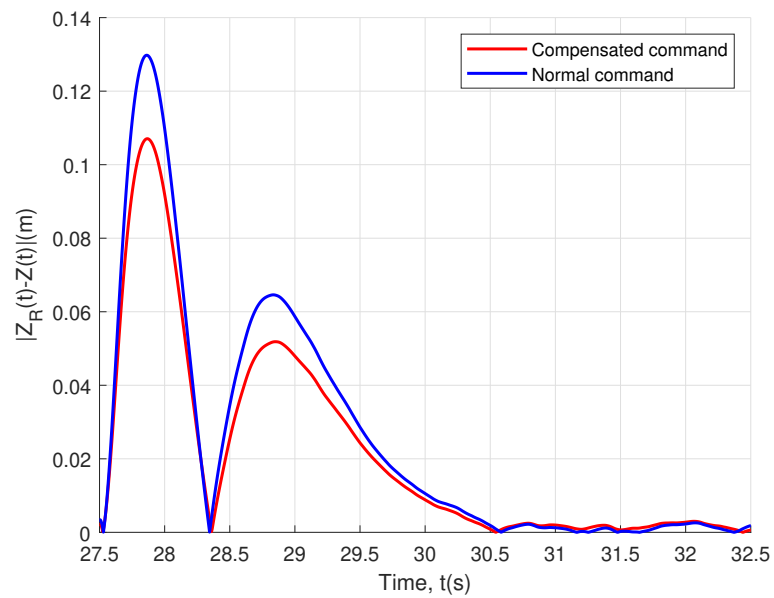


Figure 6.21: Simulated altitude error transient response for the non-compensated and compensated command generation, from 27.5 until 32.5 s.

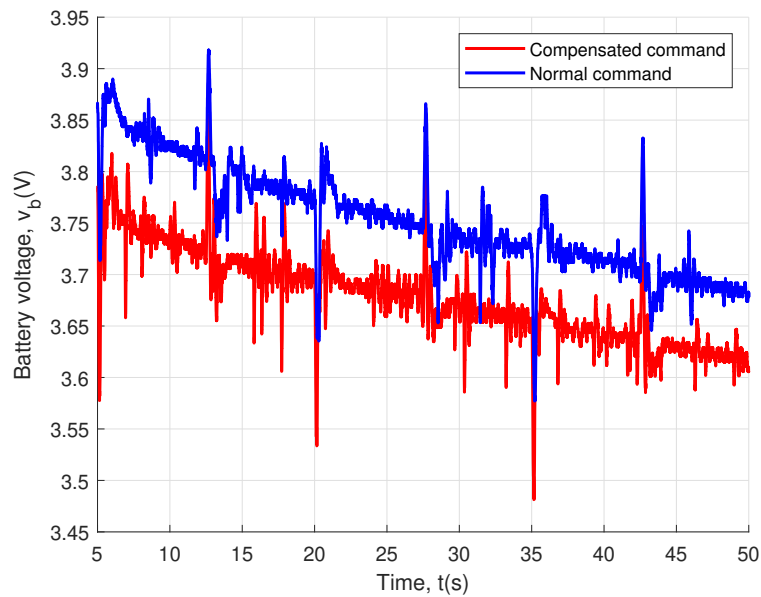


Figure 6.22: Simulation result for the battery voltage for the non-compensated and compensated command generation.

The analysis shown in section 5.3 predicted that the error dynamics would benefit from the feedback of the battery voltage v_b , as the actual motor speeds would correspond to the commanded motor speeds, at the cost of a faster discharge rate. Figs. 6.20 and 6.21 show that this improvement is verified in the simulated setting, with the absolute error for the compensated case being closer to the reference signal than the normal command case. The trade-off is also verified by the data shown in Fig. 6.22, where it can be seen that the battery discharges faster in the compensated case when compared to the case where the motor commands are generated by employing the nominal battery voltage. In the next section, the experimental results will be presented.

6.5 Experimental results for the battery-unaware and battery-aware controllers

6.5.1 Altitude control loop

The experimental results relating to the application of the battery-unaware and battery-aware controller to solve the altitude control loop problem are presented in this section. The flight maneuver shown in Fig. 6.7 was repeated two times for each experiment, one immediately after the other, with no recharge of the battery in between, using both battery-unaware and battery-aware designed controllers. This allowed the collection of data sets containing six step responses during flight at different intervals of battery voltage. The necessity of two flights is due to memory restrictions for data logging imposed by the vehicle. The battery is recharged between each experiment. The altitude responses for the first and second flights are presented in Figs. 6.23 and 6.24 for the battery-unaware and battery-aware controllers, respectively.

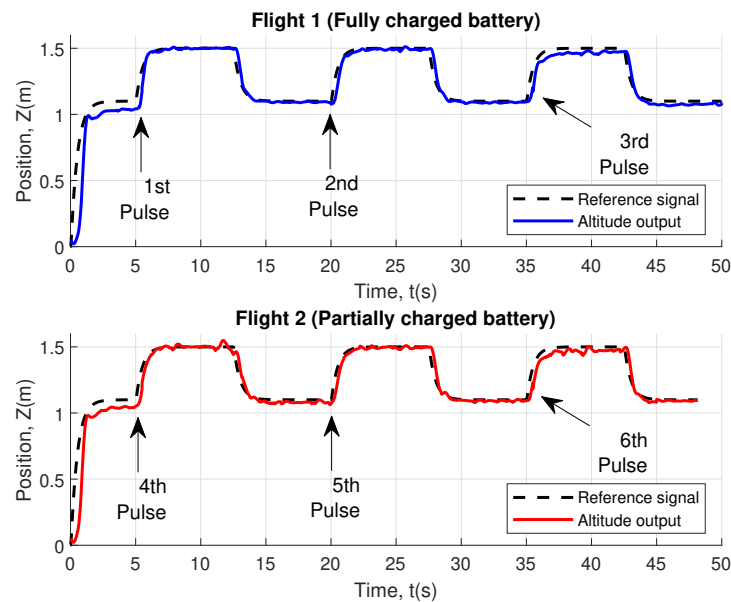


Figure 6.23: Altitude response of the battery-unaware controller.

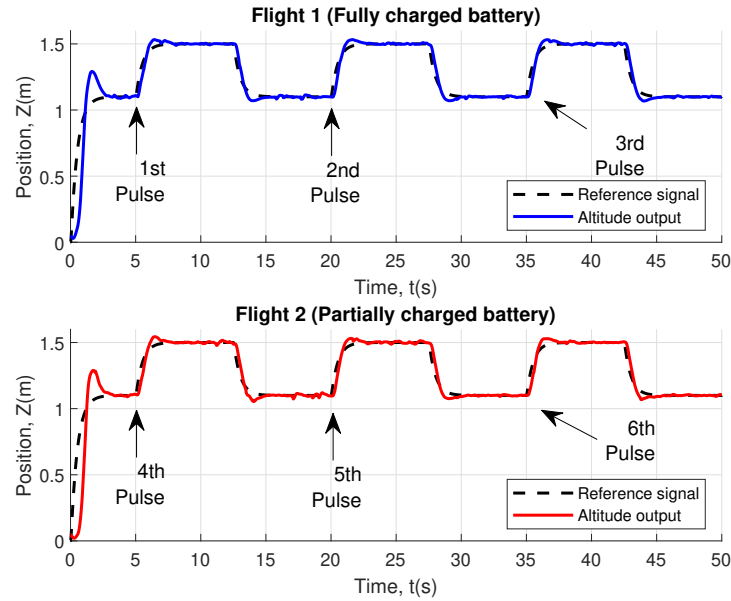


Figure 6.24: Altitude response of the battery-aware controller.

The altitude response was analyzed as follows: the periodic sections of the altitude signal corresponding to the pulses after the take-off were isolated, the absolute error between the vehicle altitude and the reference signal was calculated and the resulting error signals were superposed. The initial time t_0 was considered to be the starting time of each altitude pulse and the final time t_f is 5 s after t_0 . Additionally, the corresponding values of ξ were included in each figure as a second plot, to better demonstrate the relation between the decrease in battery voltage and the system dynamics.

The flight error transient responses and the corresponding intervals of ξ for the battery-unaware case can be seen in Fig. 6.25. It is clear that as the value of ξ decreases, deterioration can be observed in the error dynamics. When compared to the simulated results in Fig. 6.13, it is of note that the oscillating behavior was less pronounced, but the steady-state error in the lower ξ intervals still appears. These results show that the analytical demonstration in Section 5.1 and subsequent simulated results were correct to confirm a deterioration in the closed-loop dynamics. The differences observed between simulated and experimental results are to be expected, as no model can be expected to fully capture the dynamics of a system, and factors such as mechanical wear and tear, variable connection speeds between the quadrotor and the base station and variation in environmental conditions can lead to such variance.

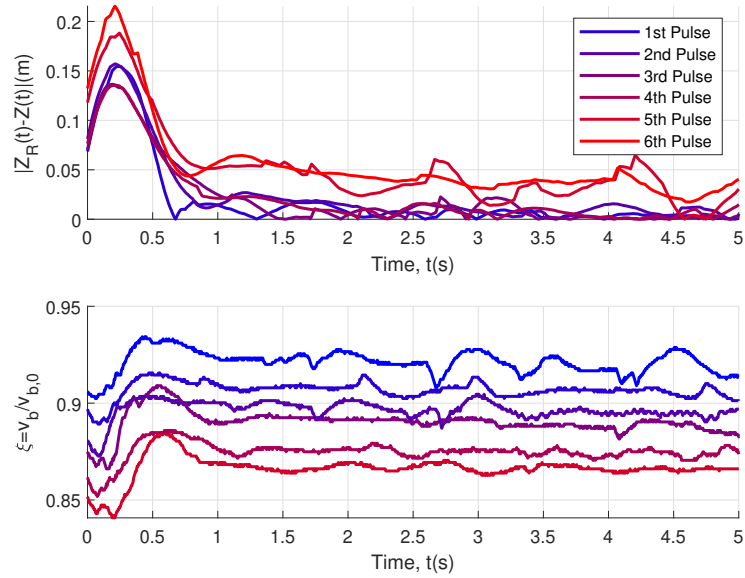


Figure 6.25: Experimental altitude error transient responses for different intervals of ξ using the battery-unaware controller design.

The behavior for the battery-aware case is shown in Fig. 6.26. The experimental results show that by taking into account the existence of the propulsion system and, critically, the battery as a variable power source, the system behavior has an overall improvement, as the behavior is consistent between all intervals of battery voltage values, in contrast with the battery-unaware case, where a significant deterioration of the closed-loop behavior was observed for the lower intervals of ξ . The behavior was particularly better in the steady-state regime. This attests that the battery-aware controller design approach resulted in a closed-loop altitude response less sensitive to variations in the battery voltage than its battery-unaware counterpart.

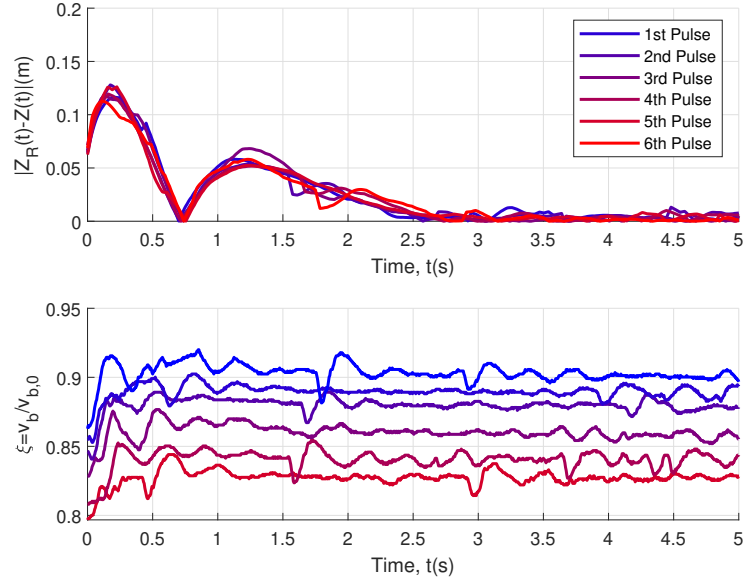


Figure 6.26: Experimental altitude error dynamics for different bands of ξ using the battery-aware controller design.

Regarding the discharge rate in both scenarios, the comparison of the battery voltage v_b can be seen in Fig. 6.27. The curves show that the battery-aware altitude controller design has a trade-off, presenting a higher discharge rate over its unaware counterpart. Thus, the system designer must balance the need for reliable closed-loop dynamics for a given band of states-of-charge against the flight autonomy desired for a given application.

6.5.2 Attitude control loop

The experimental results regarding the application of the battery-unaware and battery-aware attitude controllers are presented in this section. The maneuver specified in Fig. 6.9 was performed employing these controllers, and the resulting signals can be seen in Fig. 6.28, where the first five cycles where an attitude maneuver is performed are highlighted.

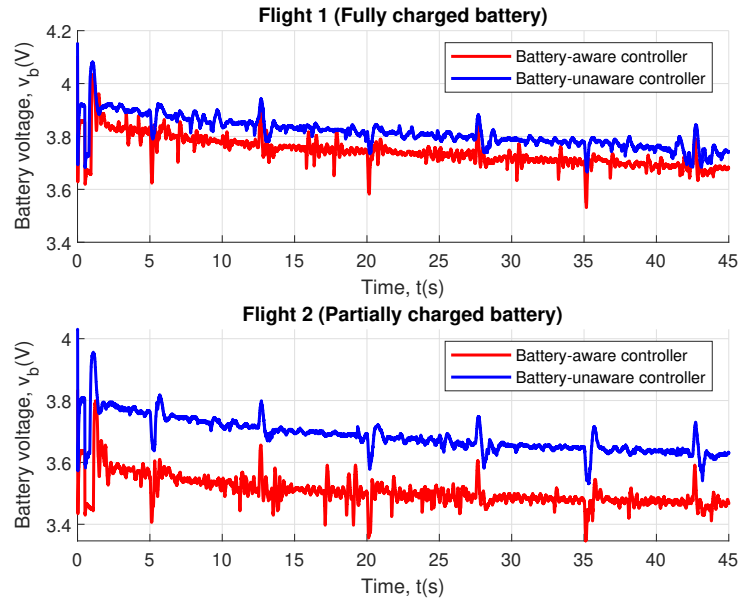


Figure 6.27: Comparison of the battery voltage v_b observed in both the battery-unaware and battery-aware cases for the altitude.

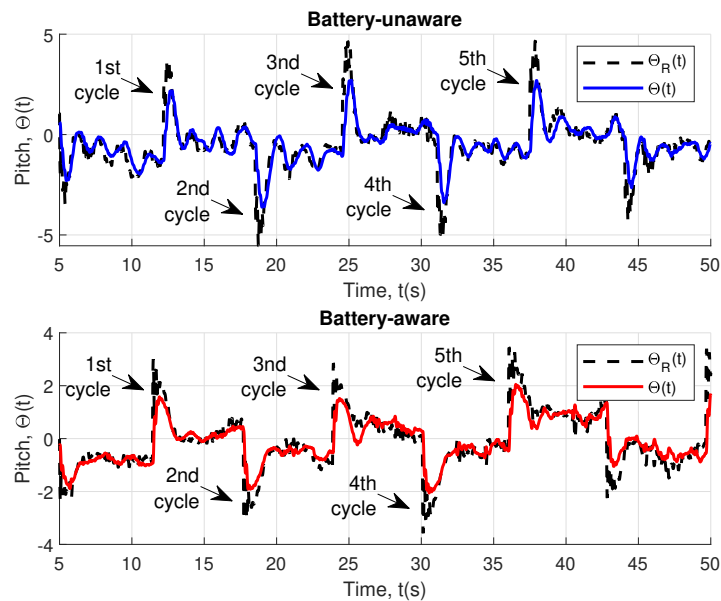


Figure 6.28: Attitude response of the battery-unaware and battery-aware controllers.

In order to compare the attitude response at different points, the sections of the maneuver corresponding to the forward movement of the aircraft were isolated, and the error signals were superposed, as was done for the altitude. The values of ξ are also included in each plot. This led to Figs. 6.29 and 6.30, for the battery-unaware and battery-aware controller,

respectively. Once again, differences between the behavior in the two scenarios are to be expected, due to mechanical wear and tear in the vehicle parts and variable connection speed between the vehicle and the base station, among others. That said, the conclusions drawn from the simulated case hold true here: the system behavior remains unaffected by the drop in battery voltage, and the use of the battery-aware controller leads only to marginal gains in performance. All error transients have a peak of approximately 4° and achieve a steady-state value under 1° in the same amount of time. This is also reflected when comparing the battery voltage in both cases in Fig. 6.31, which shows that the discharge rate was very close between the two cases. This means that although there are small gains from adopting the battery-aware approach in the attitude loop, they are not nearly as significant as those seen for the altitude.

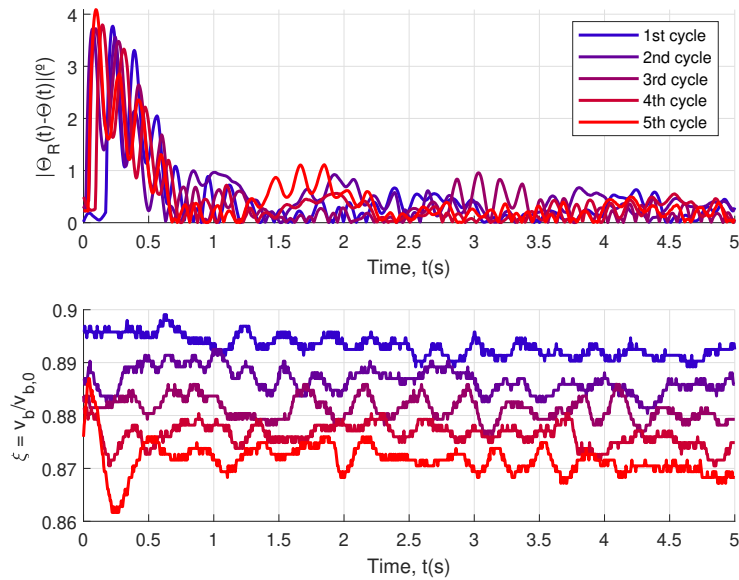


Figure 6.29: Experimental attitude error transient responses for different intervals of ξ using the battery-unaware controller design.

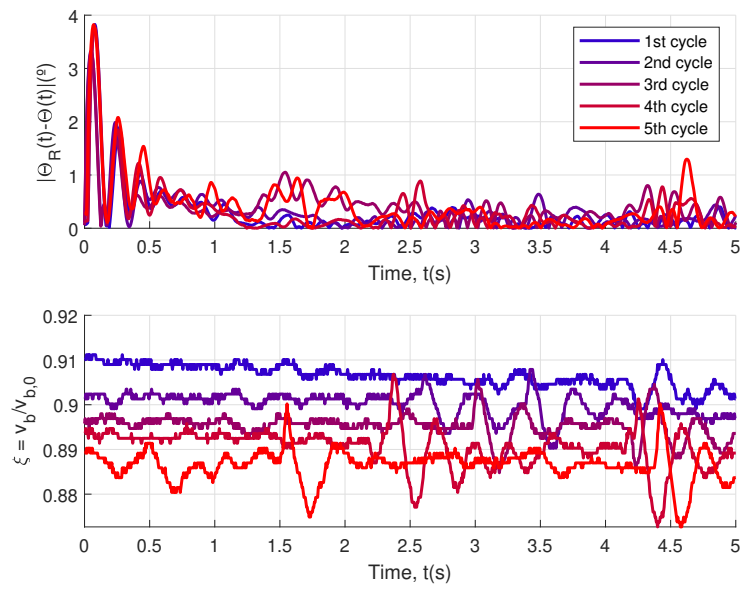


Figure 6.30: Experimental altitude error transient responses for different intervals of ξ using the battery-aware controller design.

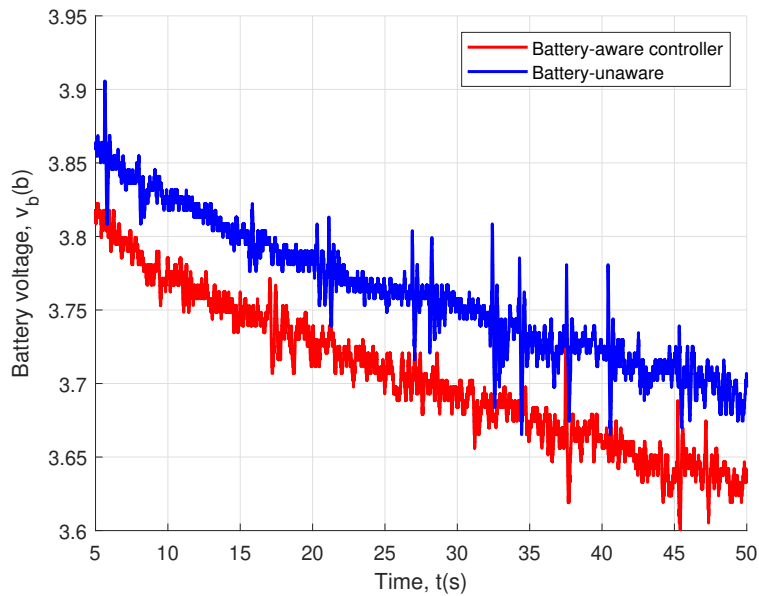


Figure 6.31: Comparison of the battery voltage v_b observed in both the battery-unaware and battery-aware cases for the attitude.

6.6 Experimental results for the adjusted command compensation

This section presents the experimental results which compare the altitude response of the quadrotor mini drone when performing the maneuver shown in Fig. 6.7 between the cases where the motor commands are obtained through the nominal battery voltage or normal commands, using (5.51), and when the measured battery voltage is fed into the command generation process or compensated commands, using (5.52). The absolute error for each case is shown in Fig. 6.32, with the signals between 27.5 to 32.5 s being highlighted in Fig. 6.33, and the corresponding battery voltages are shown in Fig. 6.34.

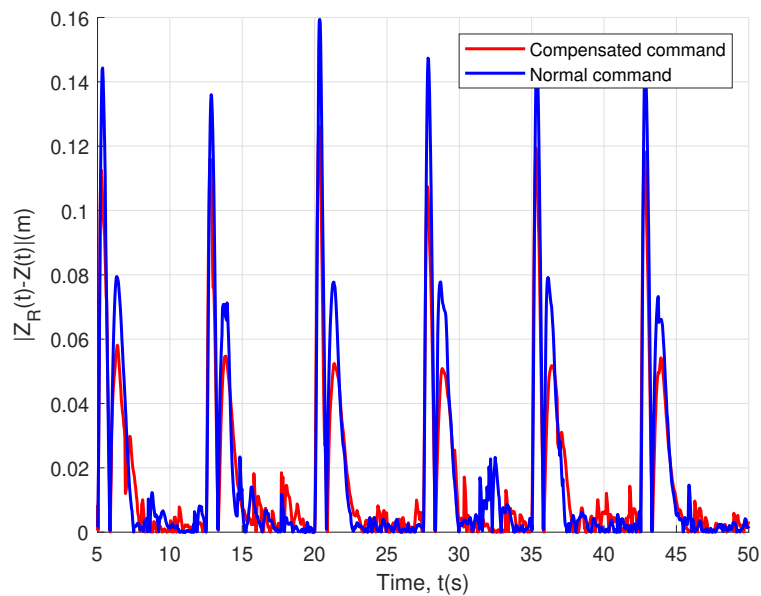


Figure 6.32: Experimental altitude error transient response for the normal and compensated command generation.

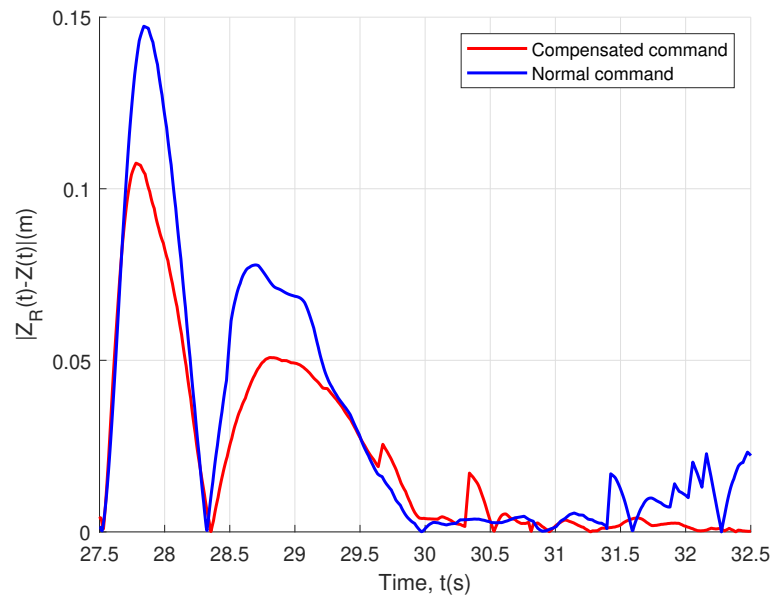


Figure 6.33: Experimental altitude error transient response for the normal and compensated command generation, 27.5 to 32.5 s.

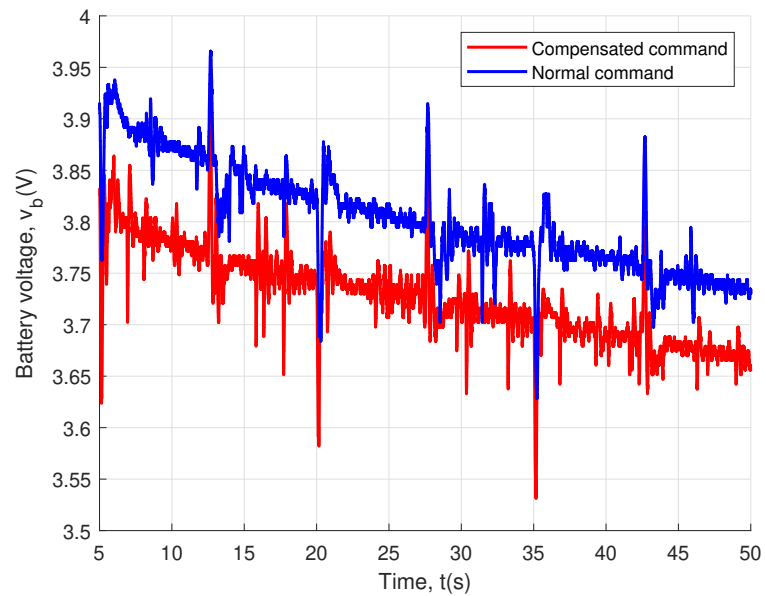


Figure 6.34: Battery voltage during flight for the non-compensated and compensated command generation.

The simulated results shown in Section 6.4 corroborated the analysis presented in Chapter 5.3, which predicted that the error dynamics would benefit from the feedback of the battery voltage v_b , as the actual motor speeds would correspond to the commanded motor speeds, at the cost of a faster discharge rate. Figs. 6.32 and 6.33 show that this improvement is also verified in the experimental setting, as the compensated case is better at tracking the reference signal. The trade-off is also verified by the battery voltage data shown in Fig. 6.34, where it can be seen that the battery discharges faster in the compensated case than in the case where the motor commands are generated by employing the nominal battery voltage.

6.7 Experimental results for the impact of the controller choice over the energy consumption

The experimental results of the trajectory test are presented in this section. Two cases were tested, one with a reference model with $\omega_\rho = 100$ and another with $\omega_\rho = 200$, that is, a less aggressive and more aggressive control approach. The battery-aware gains were employed in both cases, and both flights were conducted using the same battery, fully charged in both cases. The resulting trajectories can be seen in Fig. 6.35.

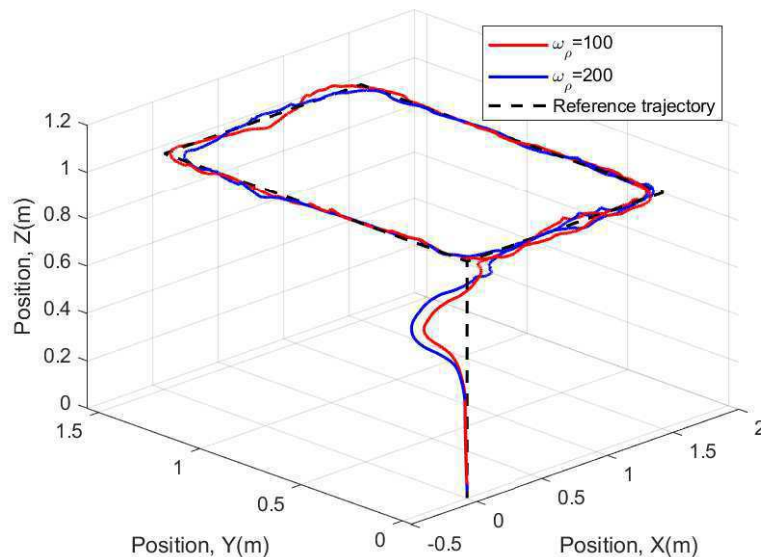


Figure 6.35: Square trajectory performed by the quadrotor mini drone with different reference models.

The altitude and pitch responses for both cases are presented in Figs. 6.36 and 6.37. Although differences in the system response can be observed between both cases, both were able to satisfactorily track the square trajectory. This is a requirement to compare the energy consumption between the two cases since if one or both of them were unable to perform the required maneuvers, from a mission design standpoint the proposed flight controller would be inadequate. Considering that the behavior was adequate in both cases, then a comparison can be made to see if any of the two approaches present an advantage either in the error transient response or in the battery discharge rate during flight.

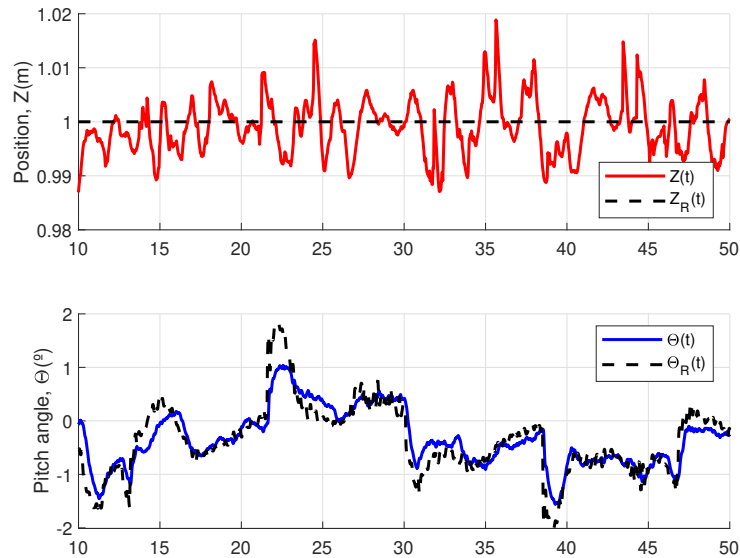


Figure 6.36: Altitude and attitude responses for the square trajectory, $\omega_\rho = 100$.

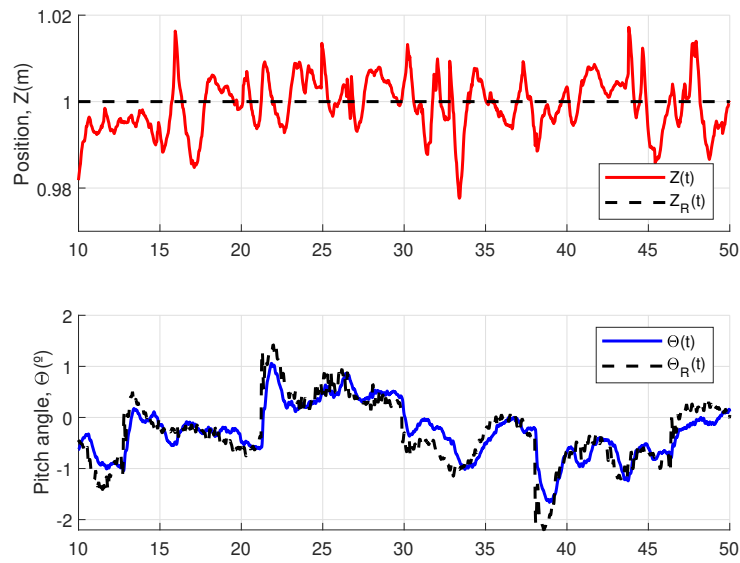


Figure 6.37: Altitude and attitude responses for the square trajectory, $\omega_\rho = 200$.

The similarity between the obtained responses can be further demonstrated by plotting the respective absolute errors for each case in the same graph, as shown in Fig. 6.38. The resulting error signals are very similar between both cases, which is also reflected when comparing the Mean Square Error (MSE) metric for each case, resulting in $0.0185 m^2$ and $0.5336 (^\circ)^2$ when $\omega_\rho = 100$ and $0.0181 m^2$ and $0.4542 (^\circ)^2$ when $\omega_\rho = 200$. These metrics show that the behavior in both cases is similar, although the faster reference model has a slight edge in performance.

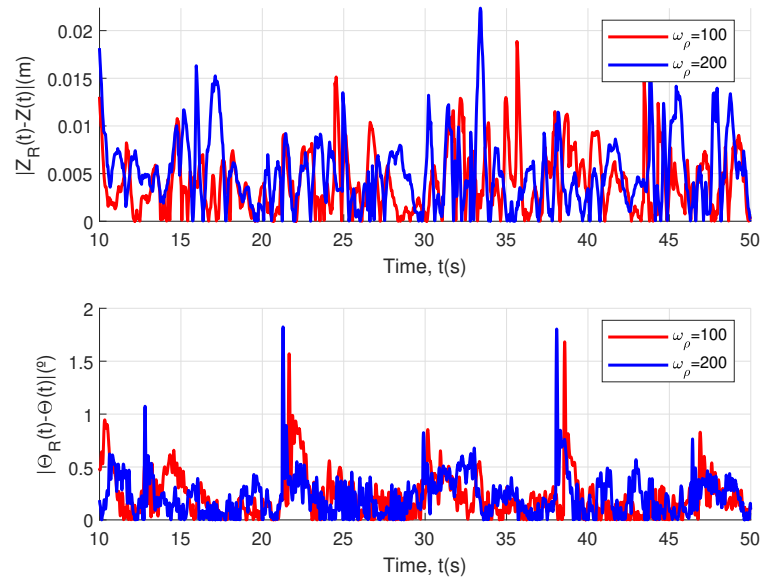


Figure 6.38: Comparison of the altitude and attitude absolute errors for the square trajectory.

Finally, the battery voltage for both cases can be seen in Fig. 6.39. The hypothesis formulated in Chapter 5 was that the shorter transient regimes from the more aggressive control strategy would lead to less tilting of the total thrust axis, resulting in less energy consumed during the flight. The results shown in Fig. 6.39 agree with this hypothesis, showing that the battery does indeed discharge slower in the case where $\omega_\rho = 200$ than the case where $\omega_\rho = 100$. The resulting gains, however, are small. This is to be expected, as attitude maneuvers for a vehicle such as the Parrot Mambo demand significantly less energy than altitude maneuvers, and since the behavior of both cases was close in regards to tracking error, it is to be expected that the resulting difference is negligible.

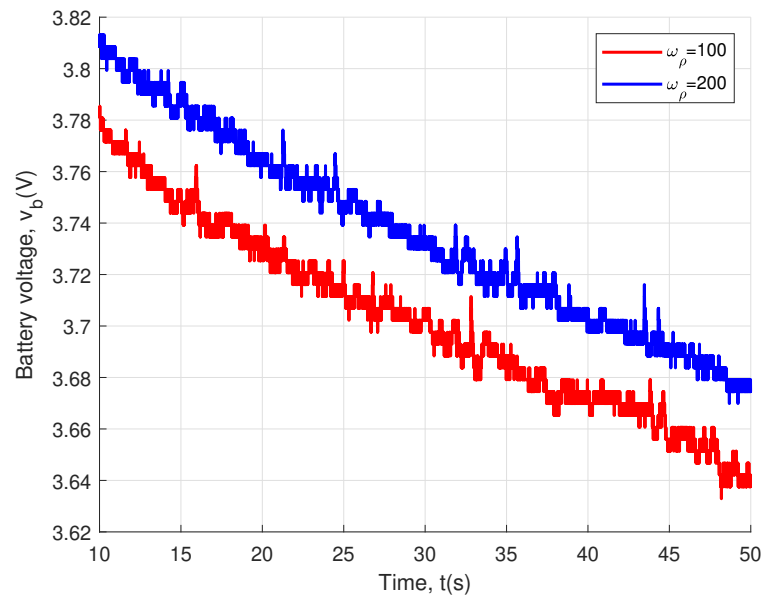


Figure 6.39: Comparison of the battery voltages for the square trajectory.

Chapter 7

Conclusion

In this chapter a description of the research results is given, describing how the research question posed in the motivation was answered, and future lines of work derived from the conducted studies are presented.

7.1 Research results

The motivation stated for this research was the following: to determine whether improvements can be made to the current design process of flight controllers for quadrotor mini drones, where the behavior of the electrical subsystem in these vehicles is ignored.

This was shown to be a relevant question through the exploration of the related works, where it was verified that the majority of works regarding the electrical energy consumption in these vehicles consider, for a previously designed system, topics such as energy-efficient path planning and battery replacement techniques. Of those few works that actually considered how the presence of a varying power source feeding the system actuators would affect the system behavior, none had provided a rigorous mathematical analysis that would lead to a model which represented these factors.

In this work, a complete model of a quadrotor mini drone vehicle and its subsystems was studied, including the components of the electrical subsystem and a nonlinear battery model. This study showed that the relevant system variables are strongly coupled and mostly nonlinear. This culminated in the analysis of how the quadrotor mini drone altitude and attitude dynamics are affected by the motor model and, more critically, by the drop in battery voltage

as it discharges during flight. Intuitively, such an effect would be present, but the analysis presented here described its nature and quantified it through the location of the poles of linearized system approximations, showing how the expected response deteriorates over time. This implies that if these effects are not considered during the design process, the resulting vehicle performance may be outside the design specifications. This was demonstrated through simulated and experimental results, where the observed response of the altitude and attitude control loops of a quadrotor mini drone presented an increased difficulty in tracking the reference signals as the battery voltage decreased.

Changes in the design process of the vehicle flight controller were proposed to mitigate these effects, one by the adaptation of an optimization-based approach to design the altitude and attitude controllers, so-called battery-aware controller design, and another by changing how the motor commands are generated. These were shown to be effective for improving the performance of the altitude loop, resulting in a consistent system response during battery discharge, and an overall improvement over the alternatives where the battery voltage was not considered a factor in the system design. However, when it comes to the adjustment of the motor commands by employing the battery voltage, the theoretical analysis predicted the elimination of the effects associated with the battery discharge, which were not verified by the experimental results. This is likely because the ESCs were considered energy conserving, as data that would enable their modeling was not available. Nevertheless, this solution still resulted in an improvement in the system's performance.

The results for the attitude control loop showed a less pronounced improvement when compared to the altitude. This is consistent with the analysis of the physics related to the movement of quadrotor mini drones. This analysis established that for the case studied in this work, the effort to maintain or increase the vehicle height is the most significant component in vehicle energy consumption. This agrees with the attitude dynamics, which are related to lateral movement, being less affected by the battery discharge.

However, this same analysis showed that the attitude response of the system will have an impact on the energy consumption, due to the tilting of the thrust axis caused by lateral movement, because of the coupling between the vertical lift necessary to maintain altitude and any movement along the horizontal plane. It was explained that this tilting of the thrust axis increases energy consumption by demanding an increase in motor speed so that the vehicle

does not lose altitude, which leads to the hypothesis that establishing more aggressive reference model dynamics for the attitude, minimizing the time in which the thrust axis is tilted, the battery would discharge slower when compared to the cases in which less aggressive reference model dynamics are employed. This hypothesis was tested through experiments and proved valid for the studied case. This conclusion might change for larger vehicles, or at higher movement speeds, where the air volume displaced due to the flight envelope is more relevant.

Thus, the answer to the original research question is that the electrical subsystem is relevant to the proper design of quadrotor mini drone systems and that the design process itself can result in better performance if the electrical subsystem is taken into account. This implies that the associated effort to correctly model the system components must be conducted when providing solutions for applications that require the use of these vehicles.

7.2 Future works

The proposed battery-aware controller design approach was implemented for a linear control strategy. While the optimization problem formulated is fairly agnostic regarding controller choice, as long as the associated parameters are constant values, there are possible interesting results to be derived by implementing and applying this methodology to other control strategies.

Due to the experimental platform restrictions regarding the nature of the DC-DC converters, these components were considered to be energy-conserving during the modeling phase of the study. A detailed model of the DC-DC converters would lead to a deeper understanding of the problem and would help explain why the proposed compensation through the generated commands for the motors, although effective, did not correspond precisely to what was predicted in the theoretical analysis.

Due to the coupling of the system variables, the analytical solution for obtaining a linear approximation of the attitude dynamics presented difficulties, which for this study were overcome through the use of a numerical tool to linearize the system. Therefore, obtaining an expression that allows the linearization of the attitude dynamics within the context of the quadrotor mini drone model proposed in this work is still an open problem.

All of the experiments were performed indoors, given that the employed experimental platform was made for this type of scenario. Environmental effects present in outdoor environments, such as wind, might present interesting challenges for energy consumption analysis. Furthermore, while this work aimed to propose general experiments which could demonstrate the overall effectiveness of the proposed compensation techniques and corroborate the results of the presented mathematical analyses, some works have demonstrated that by focusing on specific applications, such as photogrammetry, new research challenges might arise from specific needs regarding the vehicle construction and design.

Bibliography

[Abdilla, Richards & Burrow 2015]ABDILLA, A.; RICHARDS, A.; BURROW, S. Power and endurance modelling of battery-powered rotorcraft. In: . [S.l.]: Institute of Electrical and Electronics Engineers Inc., 2015. v. 2015-December, p. 675–680. ISBN 9781479999941. ISSN 21530866.

[Anggraeni et al. 2022]ANGGRAENI, D. et al. Soc estimation lithium polymer battery based on equivalent circuit model and extended kalman filter. In: . [S.l.]: Institute of Electrical and Electronics Engineers Inc., 2022. p. 118–122. ISBN 9781665499330.

[Azevedo et al. 2018]AZEVEDO, G. T. D. et al. *Pseudospectral Optimisation of UAV Trajectories for Minimal Battery Consumption in the Presence of a Wind Field*. [S.l.: s.n.], 2018. Energy efficiency with path planning under wind. ISBN 9781538628645.

[Bard & Faulkner 2001]BARD, A.; FAULKNER, L. R. *Eletrochemical methods: fundamentals and applications*. New York: J. Wiley & Sons, 2001. ISBN 9780071548564.

[Bard & Faulkner 1980]BARD, A. J.; FAULKNER, L. R. *Electrochemical Methods: Fundamentals and Applications*. [S.l.]: Wiley, 1980.

[Belmonte et al. 2018]BELMONTE, N. et al. Fuel cell powered octocopter for inspection of mobile cranes: Design, cost analysis and environmental impacts. *Applied Energy*, v. 215, p. 556–565, 2018. ISSN 0306-2619. Disponível em: <<https://www.sciencedirect.com/science/article/pii/S0306261918301788>>.

[Benito et al. 2014]BENITO, J. A. et al. Design considerations of a small uav platform carrying medium payloads. In: *Design of Circuits and Integrated Systems*. [S.l.: s.n.], 2014. p. 1–6.

- [Bolton & Pearson 2018]BOLTON, W.; PEARSON. *Mechatronics*. Pearson Education Limited, 2018. ISBN 9781292250991. Disponível em: <<https://books.google.com.br/books?id=BIV1DwAAQBAJ>>.
- [Boukoberine, Zhou & Benbouzid 2019]BOUKOBERINE, M. N.; ZHOU, Z.; BENBOUZID, M. A critical review on unmanned aerial vehicles power supply and energy management: Solutions, strategies, and prospects. *Applied Energy*, v. 255, p. 113823, 2019. ISSN 0306-2619. Disponível em: <<https://www.sciencedirect.com/science/article/pii/S0306261919315107>>.
- [Cabreira et al. 2018]CABREIRA, T. M. et al. Energy-aware spiral coverage path planning for uav photogrammetric applications. *IEEE Robotics and Automation Letters*, v. 3, n. 4, p. 3662–3668, 2018.
- [Chen et al. 2016]CHEN, X. et al. Robust adaptive sliding-mode observer using rbf neural network for lithium-ion battery state of charge estimation in electric vehicles. *IEEE Transactions on Vehicular Technology*, Institute of Electrical and Electronics Engineers Inc., v. 65, p. 1936–1947, 4 2016. ISSN 00189545.
- [Chipperfield & Fleming 1996]CHIPPERFIELD, A.; FLEMING, P. Evolutionary algorithms for control engineering. *IFAC Proceedings Volumes*, v. 29, n. 1, p. 1163–1168, 1996. ISSN 1474-6670. 13th World Congress of IFAC, 1996, San Francisco USA, 30 June - 5 July. Disponível em: <<https://www.sciencedirect.com/science/article/pii/S1474667017578222>>.
- [Chou, Pang & Yu 2020]CHOU, S. F.; PANG, A. C.; YU, Y. J. Energy-aware 3d unmanned aerial vehicle deployment for network throughput optimization. *IEEE Transactions on Wireless Communications*, Institute of Electrical and Electronics Engineers Inc., v. 19, p. 563–578, 1 2020. ISSN 15582248. Energy efficiency on mission for network.
- [Dai et al. 2019]DAI, X. et al. An analytical design-optimization method for electric propulsion systems of multicopter uavs with desired hovering endurance. *IEEE/ASME Transactions on Mechatronics*, v. 24, n. 1, p. 228–239, 2019.

- [Daigle & Kulkarni 2013]DAIGLE, M.; KULKARNI, C. S. Electrochemistry-based battery modeling for prognostics. In: *Conf. Rec. PHM*. [S.l.: s.n.], 2013.
- [Doyle, Fuller & Newman 1993]DOYLE, M.; FULLER, T. F.; NEWMAN, J. Modeling of galvanostatic charge and discharge of the lithium/polymer/insertion cell. *Journal of The Electrochemical Society*, The Electrochemical Society, v. 140, n. 6, p. 1526–1533, jun 1993.
- [Ducard & Geering 2008]DUCARD, G.; GEERING, H. P. Stability analysis of a dynamic inversion based pitch rate controller for an unmanned aircraft. In: *2008 IEEE/RSJ International Conference on Intelligent Robots and Systems*. [S.l.: s.n.], 2008. p. 360–366.
- [Falconí et al. 2013]FALCONÍ, G. P. et al. Admissible thrust control laws for quadrotor position tracking. In: *2013 American Control Conference*. [S.l.: s.n.], 2013. p. 4844–4849.
- [Falconí & Holzapfel 2014]FALCONÍ, G. P.; HOLZAPFEL, F. Position tracking of a hexacopter using a geometric backstepping control law - experimental results. In: *2014 IEEE International Conference on Aerospace Electronics and Remote Sensing Technology*. [S.l.: s.n.], 2014. p. 20–25.
- [Fletcher 2000]FLETCHER, R. Front matter. In: _____. *Practical Methods of Optimization*. [S.l.]: John Wiley & Sons, Ltd, 2000. p. i–xvii. ISBN 9781118723203.
- [Franco & Butazzo 2016]FRANCO, C. D.; BUTAZZO, G. Coverage path planning for uavs photogrammetry with energy and resolution constraints. *Journal of Intelligent Robots & Systems*, v. 83, 2016.
- [Fransozi 2015]Fransozi, L. *Modelagem Matemática do Tempo de Vida de Baterias de Lítio Íon Polímero através de Modelos Híbridos*. Tese (Doutorado) — Universidade Regional do Noroeste do Estado do Rio Grande do Sul - UNIJUÍ, 2015.
- [Galán-Jiménez et al. 2021]GALÁN-JIMÉNEZ, J. et al. Energy-efficient and solar powered mission planning of uav swarms to reduce the coverage gap in rural areas: The 3d case. *Ad Hoc Networks*, Elsevier B.V., v. 118, 7 2021. ISSN 15708705. Energy efficiency on mission for network.

- [Gandolfo et al. 2017]GANDOLFO, D. C. et al. Stable path-following control for a quadrotor helicopter considering energy consumption. *IEEE Transactions on Control Systems Technology*, Institute of Electrical and Electronics Engineers Inc., v. 25, p. 1423–1430, 7 2017. ISSN 10636536. Energy efficiency through path planning.
- [Gandolfo et al. 2017]GANDOLFO, D. C. et al. Stable path-following control for a quadrotor helicopter considering energy consumption. *IEEE Transactions on Control Systems Technology*, v. 25, p. 1423–1430, 2017.
- [Gandolfo et al. 2017]GANDOLFO, D. C. et al. Energy evaluation of low-level control in uavs powered by lithium polymer battery. *ISA Transactions*, ISA - Instrumentation, Systems, and Automation Society, v. 71, p. 563–572, 11 2017. ISSN 00190578. Energetic performance of different controllers, complex results.
- [Gjengedal, Vie & Molinas 2017]GJENGEDAL, O.; VIE, P. J. S.; MOLINAS, M. Battery modeling and kalman filter-based state-of-charge estimation for a race car application. In: . [S.l.]: Institute of Electrical and Electronics Engineers Inc., 2017. p. 561–567. ISBN 9781509044283.
- [Hassanalian & Abdelkefi 2017]HASSANALIAN, M.; ABDELKEFI, A. Classifications, applications, and design challenges of drones: A review. *Progress in Aerospace Sciences*, v. 91, p. 99–131, 2017. ISSN 0376-0421. Disponível em: <<https://www.sciencedirect.com/science/article/pii/S0376042116301348>>.
- [Horn et al. 2019]HORN, A. C. et al. A study on configuration of propellers for multirotor-like hybrid aerial-aquatic vehicles. In: *2019 19th International Conference on Advanced Robotics (ICAR)*. [S.l.: s.n.], 2019. p. 173–178.
- [Ingber 1995]INGBER, L. Adaptive simulated annealing (asa): Lessons learned. *Polish Journal Control and Cybernetics*, 1995.
- [Jee, Cho & Kim 2020]JEE, S. H.; CHO, H. C.; KIM, J. The experimental modeling of quadrotor actuators with undefined hardware errors for safety-flight. *Electronics*, v. 9, n. 4, 2020. ISSN 2079-9292. Disponível em: <<https://www.mdpi.com/2079-9292/9/4/579>>.

- [Jongerden & Haverkort 2010]JONGERDEN, M.; HAVERKORT, B. Which battery model to use? *Software, IET*, v. 3, p. 445 – 457, 01 2010.
- [Karlsson 2002]KARLSSON, M. *Control of Unmanned Aerial Vehicles using Non-linear Dynamic Inversion*. Tese (Doutorado) — Institutionen för systemteknik, 12 2002.
- [Kelley 1999]KELLEY, C. T. *Iterative Methods for Optimization*. Society for Industrial and Applied Mathematics, 1999. Disponível em: <<https://epubs.siam.org/doi/abs/10.1137/1.9781611970920>>.
- [Kennedy & Eberhart 1995]KENNEDY, J.; EBERHART, R. Particle swarm optimization. In: *Proceedings of ICNN'95 - International Conference on Neural Networks*. [S.l.: s.n.], 1995. v. 4, p. 1942–1948 vol.4.
- [Kim, Gadsden & Wilkerson 2020]KIM, J.; GADSDEN, S. A.; WILKERSON, S. A. A comprehensive survey of control strategies for autonomous quadrotors. *Canadian Journal of Electrical and Computer Engineering*, v. 43, n. 1, p. 3–16, 2020.
- [Kim, Qiao & Qu 2013]KIM, T.; QIAO, W.; QU, L. Online state of charge and electrical impedance estimation for multicell lithium-ion batteries. In: . [S.l.: s.n.], 2013. ISBN 9781479901463.
- [Kuchly et al. 2021]KUCHLY, J. et al. Li-ion battery soc estimation method using a neural network trained with data generated by a p2d model. *IFAC-PapersOnLine*, v. 54, n. 10, p. 336–343, 2021. ISSN 2405-8963. 6th IFAC Conference on Engine Powertrain Control, Simulation and Modeling E-COSM 2021. Disponível em: <<https://www.sciencedirect.com/science/article/pii/S2405896321015871>>.
- [Lee, Dai & Chuang 2018]LEE, K.-T.; DAI, M.-J.; CHUANG, C.-C. Temperature-compensated model for lithium-ion polymer batteries with extended kalman filter state-of-charge estimation for an implantable charger. *IEEE Trans. Ind. Electron.*, v. 65, n. 1, p. 589–596, 2018.
- [Li et al. 2021]LI, F. et al. Dynamic modeling, simulation, and parameter study of electric quadrotor system of quad-plane uav in wind disturbance environment. *International*

- Journal of Micro Air Vehicles*, v. 13, p. 17568293211022211, 2021. Disponível em: <<https://doi.org/10.1177/17568293211022211>>.
- [Li & Choe 2013]LI, X.; CHOE, S. Y. State-of-charge (soc) estimation based on a reduced order electrochemical thermal model and extended kalman filter. In: . [S.l.: s.n.], 2013. p. 1100–1105. ISBN 9781479901777. ISSN 07431619.
- [Li, Xiao & Choe 2011]LI, X.; XIAO, M.; CHOE, S. Y. Reduced order of electrochemical model for a pouch type high power li-polymer battery. In: . [S.l.: s.n.], 2011. p. 593–599. ISBN 9781424489282.
- [Li et al. 2011]LI, X. et al. State-of-charge (soc) estimation based on reduced order of electrochemical model for a pouch type high power li-polymer battery. In: . [S.l.: s.n.], 2011. ISBN 9781612842486.
- [Lim, Kim & Yee 2021]LIM, D.; KIM, H.; YEE, K. Mission-oriented performance assessment and optimization of electric multirotors. *Aerospace Science and Technology*, Elsevier Masson s.r.l., v. 115, 8 2021. ISSN 12709638.
- [Luiz, Lima & Lima 2022]LUIZ, S. O. D.; LIMA, E. G.; LIMA, A. M. N. Representing the accumulator ageing in an automotive lead-acid battery model. *J Control Autom Electr Syst*, v. 33, p. 204–218, 2022.
- [Maddikunta et al. 2021]MADDIKUNTA, P. K. R. et al. Unmanned aerial vehicles in smart agriculture: Applications, requirements, and challenges. *IEEE Sensors Journal*, v. 21, n. 16, p. 17608–17619, 2021.
- [Madruga et al. 2022]MADRUGA, S. P. et al. Aerodynamic effects compensation on multirotor uavs based on a neural network control allocation approach. *IEEE/CAA Journal of Automatica Sinica*, v. 9, n. 2, p. 295–312, 2022.
- [Mao, Zhao & Lin 2014]MAO, J.; ZHAO, L.; LIN, Y. State-of-charge estimation of lithium-ion polymer battery based on sliding mode observer. In: . [S.l.]: IEEE Computer Society, 2014. p. 269–273. ISBN 9789881563842. ISSN 21612927.
- [Mathworks 2020]MATHWORKS. *Parrot Drone Support from MATLAB*. 2020. Disponível em: <<https://tinyurl.com/parrotIoUg>>.

- [Mazumder & Zhang 2013]MAZUMDER, S.; ZHANG, S. S. Faster-than-real-time simulation of lithium ion batteries with full spatial and temporal resolution. *International Journal of Electrochemistry*, v. 2013, 2013. ISSN 2090-3529.
- [Mc Carthy et al. 2022]Mc Carthy, K. et al. Electrochemical impedance correlation analysis for the estimation of li-ion battery state of charge, state of health and internal temperature. *Journal of Energy Storage*, v. 50, p. 104608, 2022. ISSN 2352-152X. Disponível em: <<https://www.sciencedirect.com/science/article/pii/S2352152X22006247>>.
- [Miniguano et al. 2020]MINIGUANO, H. et al. General parameter identification procedure and comparative study of li-ion battery models. *IEEE Transactions on Vehicular Technology*, Institute of Electrical and Electronics Engineers Inc., v. 69, p. 235–245, 1 2020. ISSN 19399359.
- [Morbidi, Cano & Lara 2016]Morbidi, F.; Cano, R.; Lara, D. Minimum-energy path generation for a quadrotor uav. In: *2016 IEEE International Conference on Robotics and Automation (ICRA)*. [S.l.: s.n.], 2016. p. 1492–1498.
- [Neves et al. 2016]NEVES, B. H. et al. Battery lifetime estimation by means of an analytical continuous-time model. In: *Conf. Rec. IEEE/INDUSCON*. [S.l.: s.n.], 2016. p. 1–5.
- [Neves et al. 2016]Neves, B. H. M. et al. Battery lifetime estimation by means of an analytical continuous-time model. In: *Conf. Rec. of INDUSCON'2016*. [S.l.: s.n.], 2016.
- [Nocedal, Öztoprak & Waltz 2014]NOCEDAL, J.; ÖZTOPRAK, F.; WALTZ, R. An interior point method for nonlinear programming with infeasibility detection capabilities. *Optimization Methods & Software*, v. 29, p. 837–854, 07 2014.
- [Paschero et al. 2010]PASCHERO, M. et al. Estimation of lithium polymer cell characteristic parameters through genetic algorithms. In: . [S.l.: s.n.], 2010. ISBN 9781424441754.
- [Podhradský et al. 2013]PODHRADSKÝ, M. et al. Battery model-based thrust controller for a small, low cost multirotor unmanned aerial vehicles. In: *2013 International Conference on Unmanned Aircraft Systems (ICUAS)*. [S.l.: s.n.], 2013. p. 105–113.

- [Podhradský, Coopmans & Jensen 2014]PODHRADSKÝ, M.; COOPMANS, C.; JENSEN, A. Battery state-of-charge based altitude controller for small, low cost multicopter unmanned aerial vehicles. *Journal of Intelligent & Robotic Systems volume*, v. 74, p. 193–207, 2014.
- [Rahimi-Eichi, Baronti & Chow 2014]RAHIMI-EICHI, H.; BARONTI, F.; CHOW, M. Y. Online adaptive parameter identification and state-of-charge coestimation for lithium-polymer battery cells. *IEEE Transactions on Industrial Electronics*, Institute of Electrical and Electronics Engineers Inc., v. 61, p. 2053–2061, 2014. ISSN 02780046.
- [Rakhmatov & Vrudhula 2001]RAKHMATOV, D.; VRUDHULA, S. An analytical high-level battery model for use in energy management of portable electronic systems. In: *Conf. Rec. IEEE/ACM/ICCAD*. [S.l.: s.n.], 2001. p. 488–493.
- [Rakhmatov & Vrudhula 2003]RAKHMATOV, D.; VRUDHULA, S. Energy management for battery-powered embedded systems. *ACM Trans. Embedded Comput. Syst.*, v. 2, p. 277–324, 08 2003.
- [Sarikurt, Ceylan & Balikci 2014]SARIKURT, T.; CEYLAN, M.; BALIKCI, A. A hybrid battery model and state of health estimation method for lithium-ion batteries. In: . [S.l.]: IEEE Computer Society, 2014. p. 1349–1356. ISBN 9781479924493.
- [Sarsembayev et al. 2022]SARSEMBAYEV, B. et al. Lipo battery modeling for dynamic wireless power transfer in uav application. In: . [S.l.]: Institute of Electrical and Electronics Engineers (IEEE), 2022. p. 346–351. ISBN 9781665471404.
- [Schacht-Rodríguez et al. 2018]SCHACHT-RODRÍGUEZ, R. et al. Prognosis & health management for the prediction of uav flight endurance. In: . [S.l.]: Elsevier B.V., 2018. v. 51, p. 983–990. ISSN 24058963. Model based flight time prediction w/ linear SOC.
- [Schmidt et al. 2010]SCHMIDT, A. P. et al. Lumped parameter modeling of electrochemical and thermal dynamics in lithium-ion batteries. *IFAC Proceedings Volumes*, v. 43, n. 7, p. 198–203, 2010. ISSN 1474-6670. 6th IFAC Symposium on Advances in Automotive Control.

- [Schneideri 2011]SCHNEIDERI, K. K. *Modelos Analíticos na Predição de Tempo de Vida de Baterias Utilizadas em Dispositivos Móveis*. Tese (Doutorado) — Universidade Regional do Noroeste do Estado do Rio Grande do Sul - UNIJUÍ, 2011.
- [Scola et al. 2021]SCOLA, I. R. et al. A robust control strategy with perturbation estimation for the parrot mambo platform. *IEEE Transactions on Control Systems Technology*, v. 29, n. 4, p. 1389–1404, 2021.
- [Shi et al. 2017]SHI, D. et al. A practical performance evaluation method for electric multi-copters. *IEEE/ASME Transactions on Mechatronics*, v. 22, n. 3, p. 1337–1348, 2017.
- [Shraim, Awada & Youness 2018]SHRAIM, H.; AWADA, A.; YOUNESS, R. A survey on quadrotors: Configurations, modeling and identification, control, collision avoidance, fault diagnosis and tolerant control. *IEEE Aerospace and Electronic Systems Magazine*, v. 33, n. 7, p. 14–33, 2018.
- [Sierra et al. 2019]SIERRA, G. et al. Battery health management for small-size rotary-wing electric unmanned aerial vehicles: An efficient approach for constrained computing platforms. *Reliability Engineering and System Safety*, Elsevier Ltd, v. 182, p. 166–178, 2 2019. ISSN 09518320. Predicting flight time from SOC model.
- [Silva 2016]Silva, F. A. Lithium-ion batteries: Fundamentals and applications. *IEEE Industrial Electronics Magazine*, v. 10, n. 1, p. 58–59, 2016.
- [Spohn et al. 2008]SPOHN, M. A. et al. Simulation of blind flooding over wireless sensor networks based on a realistic battery model. In: *Conf. Rec. IARIA/ICN*. [S.l.: s.n.], 2008. p. 545–550.
- [Stanciu et al. 2015]STANCIU, T. et al. Extensive eis characterization of commercially available lithium polymer battery cell for performance modelling. In: *2015 17th European Conference on Power Electronics and Applications (EPE'15 ECCE-Europe)*. [S.l.: s.n.], 2015. p. 1–10.
- [Szafranski, Czyba & Błachuta 2014]SZAFRANSKI, G.; CZYBA, R.; BŁACHUTA, M. Modeling and identification of electric propulsion system for multirotor unmanned aerial

- vehicle design. In: *2014 International Conference on Unmanned Aircraft Systems (ICUAS)*. [S.l.: s.n.], 2014. p. 470–476.
- [Tal & Karaman 2021]TAL, E.; KARAMAN, S. Accurate tracking of aggressive quadrotor trajectories using incremental nonlinear dynamic inversion and differential flatness. *IEEE Transactions on Control Systems Technology*, v. 29, n. 3, p. 1203–1218, 2021.
- [Topan et al. 2017]TOPAN, P. A. et al. State of charge (soc) and state of health (soh) estimation on lithium polymer battery via kalman filter. In: . [S.l.]: Institute of Electrical and Electronics Engineers Inc., 2017. p. 93–96. ISBN 9781509043576.
- [Tran et al. 2021]TRAN, M.-K. et al. A comprehensive equivalent circuit model for lithium-ion batteries, incorporating the effects of state of health, state of charge, and temperature on model parameters. *Journal of Energy Storage*, v. 43, p. 103252, 2021. ISSN 2352-152X. Disponível em: <<https://www.sciencedirect.com/science/article/pii/S2352152X2100949X>>.
- [Tran et al. 2020]TRAN, M.-K. et al. Effect of integrating the hysteresis component to the equivalent circuit model of lithium-ion battery for dynamic and non-dynamic applications. *Journal of Energy Storage*, v. 32, p. 101785, 2020. ISSN 2352-152X. Disponível em: <<https://www.sciencedirect.com/science/article/pii/S2352152X20316224>>.
- [Valladolid et al. 2019]VALLADOLID, J. D. et al. Proposal for modeling electric vehicle battery using experimental data and considering temperature effects. In: *Conf. Rec. IEEE/PowerTech*. [S.l.: s.n.], 2019. p. 1–6.
- [Voznesenskii 2021]VOZNESENSKII, E. A. Automated battery charging system for multi-rotor aerial vehicles. In: . [S.l.]: Institute of Electrical and Electronics Engineers Inc., 2021. ISBN 9781728177304. Automatic charging of battery.
- [Vu, Dang & Dinh 2019]VU, N. A.; DANG, D. K.; DINH, T. L. Electric propulsion system sizing methodology for an agriculture multicopter. *Aerospace Science and Technology*, Elsevier Masson SAS, v. 90, p. 314–326, 7 2019. ISSN 12709638.

- [Wang et al. 2022]WANG, C. et al. Cooperative co-evolutionary differential evolution algorithm applied for parameters identification of lithium-ion batteries. *Expert Systems with Applications*, v. 200, p. 117192, 2022. ISSN 0957-4174.
- [Wang, Wang & Ren 2022]WANG, Y.; WANG, Y.; REN, B. Energy saving quadrotor control for field inspections. *IEEE Transactions on Systems, Man, and Cybernetics: Systems*, v. 52, n. 3, p. 1768–1777, 2022.
- [Wu, Li & Du 2018]WU, X.; LI, X.; DU, J. State of charge estimation of lithium-ion batteries over wide temperature range using unscented kalman filter. *IEEE Access*, Institute of Electrical and Electronics Engineers Inc., v. 6, p. 41993–42003, 7 2018. ISSN 21693536.
- [Yacef et al. 2017]YACEF, F. et al. Optimization of energy consumption for quadrotor uav. In: . [S.l.: s.n.], 2017.
- [Yahui, Shaolei & Cong 2014]YAHUI, Q.; SHAOLEI, Z.; CONG, S. Height control of a quadrotor when voltage of battery falls. In: *Proceedings of 2014 IEEE Chinese Guidance, Navigation and Control Conference*. [S.l.: s.n.], 2014. p. 1427–1430.
- [Yuan et al. 2013]YUAN, R. et al. Stability robustness of nonlinear dynamic inversion based controller. In: *2013 IEEE International Conference on Robotics and Biomimetics (ROBIO)*. [S.l.: s.n.], 2013. p. 328–333.
- [Zhang et al. 2021]ZHANG, H. et al. Multidisciplinary design optimization of an electric propulsion system of a hybrid uav considering wind disturbance rejection capability in the quadrotor mode. *Aerospace Science and Technology*, Elsevier Masson s.r.l., v. 110, 3 2021. ISSN 12709638.
- [Zhanqi & Xi'an 2012]ZHANQI, F.; XI'AN, L. L. The high angle of attack aerodynamic modeling and nonlinear dynamic inversion flight control law design. In: *IEEE 10th International Conference on Industrial Informatics*. [S.l.: s.n.], 2012. p. 901–905.
- [Zhao, Wenzl & Bohn 2012]ZHAO, Q.; WENZL, H.; BOHN, C. Li-ion polymer battery soc estimation using bayesian filtering. *Proceedings of the 31st Chinese Control Conference*, 2012.

[Zhao et al. 2018]ZHAO, T. et al. Low cost autonomous battery replacement system for quadrotor small unmanned aerial systems (suas) using 3d printing components. In: *2018 International Conference on Unmanned Aircraft Systems (ICUAS)*. [S.l.: s.n.], 2018. p. 103–107.